Medipix3RX characterisation in MARS

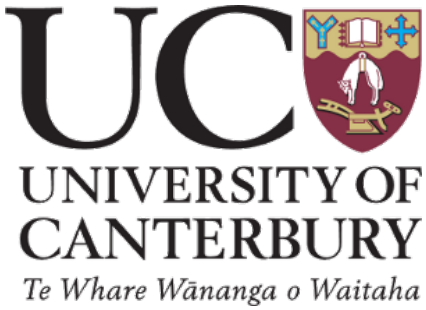

Lieza Vanden Broeke

School of Physical and Chemical Sciences

University of Canterbury

A thesis submitted for the degree of

Doctor of Philosophy in Medical Physics

February 7, 2019

Acknowledgements

It is a dream of many to be able to bring an idea to life. To turn that idea into a successful business is something even more unimaginable. Two of my supervisors, and the founders of MARS Bioimaging, Phil and Anthony Butler taught me to build my dreams, no matter how big or small they may be. I would like to thank them for giving me the opportunity to do a PhD with the MARS group. It is an honour and immense privilege to work alongside them. I am also thankful to Callaghan Innovation for supporting my studies. Without the financial support I received from them I would probably not have attempted the ginormous mountain that is a PhD.

I would like to thank Dr Ali Atharifard for the many hours of discussion and his support and patience when explaining things to me. Our minds appear to work together in a very favourable way and I feel very fortunate to have him as one of my supervisors. I thank Dr Christopher Bateman as one of my early supervisors. The skills he taught me have helped me immensely on my PhD journey. I would also like to thank Prof Hermann Kolanoski who gave me the push that I needed to start my experimental journey. I am hugely grateful to everyone in the MARS group for always encouraging my curiosity. You all endeavoured to answer my many questions. Thanks to you I will never stop questioning how and why things work they way they do.

I am beyond grateful for the support of my friends and family. They always kept me positive and believed in me, despite some significant set-backs. My parents always encouraged me to do what makes me happy, and what I love. Because of them, I had the courage to attempt a PhD.

Abstract

The goal of this thesis is to characterise the energy response of a multi-element camera in a MARS spectral scanner using x-ray fluorescence (XRF). The latest version of the MARS small bore scanner makes use of the Medipix3RX ASIC, bonded to a CZT semi-conductor layer, to count x-ray photons and create spectroscopic CT data. The MARS imaging chain uses the energy-resolved 2D transmission images to construct quantitative 3D spectral images. MARS imaging research can be broadly categorised into three streams: (1) detector technology, (2) image processing, reconstruction and visualisation, and (3) preclinical studies. The novel work presented in this thesis falls into the first two categories, but has direct consequences on the third category.

A novel XRF model is developed to represent the XRF distribution in the detector plane. The model offers a user-friendly Matlab function where scanner parameters are easily changed, preventing the need for time-consuming experiments. The model confirms that the distance between the metallic foil and the Medipix3RX has a large effect on the strength of the XRF signal. Experimental XRF from metallic foils are presented from an optimised geometrical setup (based on the model). The results show that the molybdenum, tantalum and lead foils have an experimental XRF peak that is close to the theoretical XRF peak. The final part of this thesis demonstrates that the energy response of the Medipix3RX can be characterised using XRF, in a form that is useful to the image reconstruction team.

The work in this thesis improves the quality of the spectroscopic data obtained with the MARS small-bore scanners, and in turn makes MARS images more medically useful. The long term motivation for this goal is to provide economic and health benefits to New Zealand.

Scientific contributions

The research presented in this thesis investigates and develops techniques for improving the spectral performance of the MARS spectral imaging system. During the course of this thesis, I have contributed to the MARS project through numerous peer-reviewed publications, conference proceedings, poster presentations, oral presentations, student supervisions, and demonstrations and presentations about the MARS project to the community and to future students. These have helped secure the continuance of the MARS project. My contributions are listed in this section.

Prior to staring my PhD with the MARS group in 2015, I was co-author on one MARS publication and one conference proceeding (MSc).

1. R. Aamir, A. Chernoglazov, C. J. Bateman, A. P. H. Butler, P. H. Butler, N. G. Anderson, S. T. Bell, R. K. Panta, J. L. Healy, J. L. Mohr, K. Rajendran, M. F. Walsh, N. de Ruiter, S. P. Gieseg, T. Woodfield, P. F. Renaud, **L. Vanden Broeke** and others, MARS spectral molecular imaging of lamb tissue: data collection and image analysis, *Journal of Instrumentation*, 2014, Volume 9, Issue 2.
   This paper demonstrates that lipid, water and bone can be discriminated in data collected by the Medipix3RX photon counting detector. The data used for this publication has been made available to enable other researchers to test their image reconstruction and material analysis techniques. My contribution to this publication includes preparing the MARS scanner for the lamb tissue scan.

2. A. Atharifard, S. T. Bell, M. Ramyar, B. Goulter, M. F. Walsh, **L. Vanden Broeke**, A. P. H. Butler, Pixel by pixel energy calibration of MARS camera, Proceedings of NZPEM 2014 Nov 20-21st, Christchurch, New Zealand.
This research demonstrates that variations in energy responses of pixels of the MARS camera is a limiting factor for global energy resolution and the image quality. Up to 5 keV dispersion of threshold energy across the detector array has been observed. A method that quantifies the error in energy responses of individual pixels across the spectra and corrects for it is introduced. The results are validated through x-ray fluorescence measurements. My contribution to this research includes developing methods for the per-pixel energy calibration of the MARS scanner by working as a part of the "foil group".

Peer-reviewed Journal Articles

Since starting my PhD with the MARS group in September 2015, I have published one paper as primary author and I am a co-author on four other papers. Additionally, one paper is being prepared for publication where I am the primary author. For the publications and conference proceedings where I am listed as a co-author under **The MARS team** my research has directly or indirectly contributed. A complete list of MARS team publications and proceedings can be found on the MARS Bioimaging website.

1. **L. Vanden Broeke**, A. Atharifard, B.P. Goulter, J.L. Healy,M. Ramyar, R.K. Panta, M. Anjomrouz, M. Shamshad, A. Largeau, K. Mueller and others. Oblique fluorescence in a MARS scanner with a CdTe-Medipix3RX, *Journal of Instrumentation*, 2016, Volume 11, Issue 12.
This paper develops a model that identifies near optimal positions inside a MARS scanner that maximises the x-ray fluorescence (XRF) signal while minimising transmitted and scattered x-rays from the primary beam. Preliminary experimental measurements of the XRF distribution outside of the main beam, taken with a CdTe-Medipix3RX, are presented and a comparison between the model and experiment is made. I was involved in the develop-

ment of the model, the experimental tests, and the writing and revising of the paper.

2. A. Atharifard, J.L. Healy, B.P. Goulter, M. Ramyar, **L. Vanden Broeke**, M.F. Walsh, C.C. Onyema, R.K. Panta and others. Per-pixel energy calibration of photon counting detectors. *Journal of Instrumentation*, 2017, Volume 12, Issue 3.
   This paper presents a methodology for quantifying the spectral response of individual pixels in an energy resolving photon counting detector. I contributed to developing the methodology, and the data acquisition.

3. M. Anjomrouz, M. Shamshad, R. K. Panta, **L. Vanden Broeke**, N. Schleich, A. Atharifard, and others. Beam Profile Assessment In Spectral CT Scanners. *Journal of Applied Clinical Medical Physics*. 2017
   This paper presents a method that uses a combination of experimental and modelled data to assess properties of x-ray beam measurements obtained from a MARS small animal scanner. Characterisation of the beam profile is useful in improving the accuracy of spectral reconstruction models. My contribution is in acquiring a series of measurements using a MARS small-bore scanner. These measurements were then used for the validation of the beam profile.

4. M. Shamshad, M. Anjomrouz, D. J. Smithies, A. Largeau, G. Lu, A. Atharifard, **L. Vanden Broeke**, R. Aamir and others. Semi-analytic off-axis X-ray source model. *Journal of Instrumentation*, Volume 12, October 2017
   This paper develops a parameterised semi-analytical x-ray source model in the diagnostic imaging range (30-120kVp) by applying regression techniques to data obtained from custom Monte Carlo simulations of the x-ray tube used in numerous MARS scanners. It provides qualitative and quantitative information about the energy distribution. My contribution is in acquiring a series of measurements using a MARS small-bore scanner. These measurements were then used for the validation of the semi-analytic source model.

5. C. Bateman, D. Knight, B. Brandwacht, J. Mc Mahon, J. Healy, R. Panta, R. Aamir, **L. Vanden Broeke**, and others. MARS-MD: rejection based

image domain material decomposition. *Journal of Instrumentation*, Volume 13, May 2018

This paper outlines image domain material decomposition algorithms that have been routinely used in MARS spectral CT systems. These algorithms (known collectively as MARS-MD) are based on methods for solving the under-determined problem where there are more materials than energy bins. I contributed to the testing of the new MARS-MD algorithm.

Under preparation

6. **L. Vanden Broeke**, A. Atharifard, C. J. Bateman, Hermann Kolanoski, and the MARS team. Calibrating MARS Cameras using X-ray Fluorescence. To be submitted to the Journal of Instrumentation 2018.

   This paper develops a x-ray fluorescence method to characterise the energy response of a multi-element camera in a MARS spectral scanner. This method makes the material analysis more accurate, and in turn makes MARS images more medically useful. I am involved in the development of the x-ray fluorescence method, collecting and analysing the experimental data, and the writing of the paper.

Conference Abstracts

1. **L. Vanden Broeke**, A. Atharifard, B. P. Goulter, J. L. Healy, R. K. Panta, and others. *Oblique fluorescence in a MARS scanner with a CdTe-Medipix3RX*. Proceedings of 18^{th} International Workshop on Radiation Imaging Detectors (iWoRiD), Barcelona, July 2016.
2. A. Atharifard, S. T. Bell, M. Ramyar, B. P. Goulter, M. F. Walsh, **L. Vanden Broeke**, A. P. H. Butler, P. H. Butler. *Pixel by pixel energy calibration of MARS camera.* Proceedings of New Zealand Physics and Engineering in Medicine (NZPEM), University of Otago, Christchurch School of Medicine, Nov 2014.
3. A. Atharifard, J. L. Healy, B. P. Goulter, M. Ramyar, **L. Vanden Broeke**,

and others *Per-pixel Energy Calibration of Photon-counting Detectors*. Proceedings of 18^{th} International Workshop on Radiation Imaging Detectors (iWoRiD), Barcelona, July 2016.

4. M. Anjomrouz, M. Shamshad, D. J. Smithies, A. Largeau, **L. Vanden Broeke**, and others .*Beam Profile Assessment in MARS Spectral Imaging Systems*. Proceedings of IEEE Nuclear Science Symposium and Medical Imaging Conference (NSS/MIC), Strasbourg, Sep 2016.
5. M. Shamshad, M. Anjomrouz, D. J. Smithies, A. Largeau, G. Lu, **L. Vanden Broeke**, and others, *Semi-Analytic X-ray Source Model for MARS Spectral CT*. Proceedings of IEEE Nuclear Science Symposium and Medical Imaging Conference (NSS/MIC), Strasbourg, Sep 2016.
6. **L. Vanden Broeke**, C. J. Bateman, Hermann Kolanoski, and the MARS team. *Calibrating MARS Cameras using X-ray Fluorescence*. Proceedings of 20^{th} International Workshop on Radiation Imaging Detectors (iWoRiD), Sundsvall, June 2018.
7. A. Atharifard and **the MARS team**. *Pulse Pileup Models for Spectral X-ray Imaging*. Proceedings of 20^{th} International Workshop on Radiation Imaging Detectors (iWoRiD), Sundavall, June 2018.
8. A. Raja and **the MARS team**. *MARS spectral CT imaging using CZT Medipix3RX*. Proceedings of 20^{th} International Workshop on Radiation Imaging Detectors (iWoRiD), Sundsvall, June 2018.
9. C. Lowe, A. Ortega and **the MARS team**, *MARS pulmonary spectral molecular imaging: potential for locating Tuberculosis involvement*. Proceedings of IEEE Nuclear Science Symposium and Medical Imaging Conference, Sydney, Australia, November 2018.
10. F. Aghariomabad, A. Ortega and **the MARS team**, *Intrinsic Respiratory Gating for MARS imaging*. Proceedings of IEEE Nuclear Science Symposium and Medical Imaging Conference, Sydney, Australia, November 2018.
11. E. Searle and **the MARS team**. *Distinguishing iron and calcium using MARS spectral CT*. Proceedings of IEEE Nuclear Science Symposium and

Medical Imaging Conference, Sydney, Australia, November 2018.

12. M. Moghiseh and **the MARS team**. *Cancer imaging with nanoparticles using MARS spectral scanner.* Proceedings of IEEE Nuclear Science Symposium and Medical Imaging Conference, Sydney, Australia, November 2018.

13. A. Butler and **the MARS team**. *First living human images from a MARS photon-counting 8-energy CT.* Proceedings of IEEE Nuclear Science Symposium and Medical Imaging Conference, Sydney, Australia, November 2018.

14. M. Moghiseh and **the MARS team**. *Spectral CT of Cancer Cells with Nano-Particles: In-Vitro and In In-Vivo Results.* Proceedings of the Radiological Society of North America (RSNA), Chicago, America, November 2018

Oral presentations

Below is a list of the oral presentations that I have given about my research. Additionally, I have helped with numerous MARS demonstrations to high school students, I have presented talks on behalf of the MARS team to the general public, and I have helped at many University open days.

1. "Foil fluorescence in MARS spectral imaging" (MSc thesis). Nikhef Conference, Amsterdam, Netherlands, June 2015.
2. "Oblique fluorescence in a MARS scanner with a CZT Medipix3RX". MedTech in Christchurch, Christchurch Hospital, New Zealand, May 2016.
3. "Oblique fluorescence in a MARS scanner with a CZT Medipix3RX". Physics and Astronomy Departmental Conference, University of Canterbury, New Zealand, September 2016.
4. "Determination of optimal foil Thickness". MARS research group seminar, University of Canterbury, Christchurch, New Zealand, November 2016.

5. "The effect of foil position on foil fluorescence in MARS-CT4". MARS research group seminar, University of Canterbury, Christchurch, New Zealand, February 2017.
6. "MARS and I". Physics and Astronomy departmental Seminar, University of Canterbury, Christchurch, New Zealand, May 2017
7. Thesis in 3. Department of Physics and Astronomy, University of Canterbury, New Zealand, July 2017.
8. Thesis in 3. College of Science, University of Canterbury, New Zealand, August 2017.
9. "Energy calibration of MARS", Physics and Astronomy Departmental Conference, University of Canterbury, New Zealand, September 2017.
10. "Detector response". MARS research group seminar, University of Canterbury, Christchurch, New Zealand, April 2018.
11. "MARS spectral CT imaging using CZT Medipix3RX". International Worksop on Radiation Imaging Detectors (iWoRiD) Conference, Sundsvall, Sweden, June 2018.
12. Thesis in 3. School of Physical and Chemical Sciences, University of Canterbury, New Zealand, July 2018.
13. Thesis in 3. College of Science, University of Canterbury, New Zealand, August 2018.

Poster presentations

1. **L. Vanden Broeke**, A. Atharifard, C. J. Bateman, and the MARS team,, "Oblique fluorescence in a MARS scanner with a CdTe-Medipix3RX". International Workshop on Radiation Imaging Detectors (iWoRiD), Barcelona, Spain, July 2016.
2. **L. Vanden Broeke**, A. Atharifard, C. J. Bateman, and the MARS team,"Oblique fluorescence in a MARS scanner with a CdTe-Medipix3RX". International Workshop on Semiconductor Detectors, First Barcelona Techno Week, Barcelona, Spain, July 2016.

3. **L. Vanden Broeke**, A. Atharifard, C. J. Bateman, and the MARS team, "Calibrating MARS Cameras Using X-ray Fluorescence". International Workshop on Radiation Imaging Detectors (iWoRiD), Sundsvall, Sweden, June 2018.

Awards and grants

1. **Callaghan Innovation R&D scholarship** - This scholarship was awarded to fully support my PhD research for three years.
2. **School of Physical and Chemical Sciences (SPCS) Travel Fund** - This fund is available for travel for which there is no other source of funding readily available, and which are of significant tangible benefit to the applicant and the school. I was awarded this grant to attend the 20^{th} International Workshop on Radiation Imaging Detectors (iWoRiD) held in Sundsvall, and also to attend the Medipix meeting in Sundsvall after the conference in June 2018
3. **Thesis in 3 Physics and Astronomy Representative** - I was selected to represent the Physics and Astronomy department at the College of Science Thesis in 3 competition in July 2017.
4. **2017 Physics and Astronomy 33^{rd}Department Conference Postgraduate Research Presentation Award** - I was awarded the prize for the best presentation at the Physics and Astronomy Departmental Conference in September 2017.
5. **Thesis in 3 School of Physical and Chemical Science Representative** - I was selected to represent the School of Physical and Chemical Science at at the College of Science Thesis in 3 competition in August 2018.

Textbook chapter

1. Phil Butler, Ali Atharifard, **Lieza Vanden Broeke**, Rayhan Uddin, Raj Panta, Jereena Sreedharan Sheeja, Brian Goulter, Marzi Anjomrouz, with contributions from the rest of the MARS team. Physics Volume of the

MARS textbook.
The Physics volume of the MARS textbook is an unpublished and internal document that describes the physics behind the MARS spectral imaging system.

Student supervision

Jie Kuang and Paul Estacio, both 300-level BSc students at the University of Canterbury. Jie and Paul had to undertake a 150 hour, 300-level research project in the second Semester of 2016. They worked on detecting x-ray fluorescence in a MARS CT scanner. I was involved with their day-to-day supervision, basic familiarity with the MARS group and their project, offering advice and helping with their presentations and final reports.

Translational outcomes

In July 2018 the first diagnostic quality images from the MARS human system (large bore scanner) were published. The breathtaking images stunned the entire world. This demonstrates that the MARS small bore technology can be translated to living humans. This is an incredible step forward and our work is having an enormous impact on the world. The research presented in this thesis has direct consequences on the company's successes. A list of the 42 recent media publications are shown below.

1. Scientists develop 3D, full-color x-rays. 2018, Engadget.
2. Ankle Slicethrough Using MARS Spectral X-ray Scanner 2018, Medgadget.
3. World's First Ever Colour X-Ray Performed On a Human. Lifestyle: Health & Fitness [Web article] 2018 July 13 1].
4. Father and son develop world-first scanner using CERN tech. Medical & healthcare [Web article] 2018 July 11.
5. First-ever colour X-ray on a human. [Web article] 2018 July 12..
6. First human scanned with next-generation 3-D colour medical scanner. [Web article] 2018 July 10.

7. NZ scientists produce first 3D color X-ray on a human. Scitech [Web article] 2018 July 12.
8. New Zealand scientists performs first 3D, colour X-ray on a human. [Web article] 2018 July 12.
9. First 3D Color Xray Of Human Body. [Web article] 2018 July 12.
10. Agnew, M. First human scanned with next-generation scanner invented by UC scientists. News [Web article] 2018 July 10.
11. Austin-Morgan, T. First 3D colour X-ray of a human using CERN technology. [Web article] 2018 July 11.
12. Baumgaertner, E. 3-D Color X-Rays Could Help Spot Deadly Disease Without Surgery. Health [Web article] 2018 July 17.
13. Burns, C. Behold, 3D color X-rays: MARS scanner, made with CERN tech. [Web article; videorecording] 2018 July 12.
14. Daley, J. Check Out These Awesome New 3D, Full-Color X-Rays. [Web article] 2018 July 13.
15. Davies, L. Christchurch father and son developing 3D scanner that could save millions. One NewsNow [Web article] 2018 9 July.
16. D'Estries, M. Your next X-ray could be in full color and 3D. Research & Innovations [Web article] 2018 July 14.
17. Dormehl, L. Thanks to CERN, your next X-ray scan could be in full color Emerging Tech [Web article] 2018 July 13.
18. Dorn, L. The World's First Human Body Scanner That Can Produce Highly Detailed Full Color 3D X-Ray Images. [Web article] 2018 July 16.
19. Filippidis, K. Scientists develop the world's first 3D color X-rays. Medicine [Web article] 2018 July 16.
20. Freeman, T. First human scanned with spectral X-ray scanner. Diagnostic Imaging: Research Update [Web article] 2018 July 11.
21. Houser, K. These Mind-Blowing Images of The Human Body Were Made By A New Kind of Scanner. The Digest [Web article] 2018 July 12.
22. Houser, K. Whoa, We Now Have X-Rays That Take Colour Images of The Human Body. [Web article] 2018 July 13.
23. Irving, M. CERN chip enables first 3D color X-ray images of the human body. Medical [Web article] 2018 July 11.

24. Johnson, S. New X-ray technology produces striking 3D images in full color. [Web article] 2018 July 13.
25. Joita, B. 3D Color X-Rays Now Possible Thanks to CERN-Made Chip. Science [Web article] 2018 July 13.
26. Kim, A. New Zealand start-up scans 1st humans with spectral CT. [Web article] 2018 July 18.
27. Kooser, A. Color X-ray scanner uses CERN tech to see all your innards: Fat, bone, metal. It's all there in 3D. News [Sci-Tech] 2018 July 12.
28. Kovner, A. New Full-Color, 3D X-Ray Platform Set To Revolutionize Medicine - And They Look Really Cool. Physics [Web article] 2018 July 13.
29. Liszewski, A. The World's First Full-Colour, 3D X-rays Are Freaking Me Out. Medical Devices [Web article] 2018 July 13.
30. Mehar, P. First human scanned with next-generation 3D color medical scanner. Invention [Web article] 2018 July 10.
31. Muller, R. First 3D colour X-ray of a human using CERN technology. Knowledge Transfer [Web article] 2018 July 10 July 10.
32. O'Donnell, D. New Type Of "Color" X-Ray Can Take Over the Clinical World. Health [Web article] 2018 July 17.
33. Papadopoulos, L. World's First 3D Color X-Rays of Human Body Produced Using CERN Technology. Innovation: 3D Technologies [Web article] 2018 July 13.
34. Rohman, M. First human scanned with novel 3D color x-ray scanner in New Zealand. Advanced Visualisation [Web article] 2018 July 10.
35. Schembri, F. X-rays get upgrade to 3D, full color. [Web article] 2018 July 18.
36. Scott, E. You Need To See The World's First 3D Colour X-Rays Of Human Bodies. [Web article] 2018 July 16.
37. Sturman, C. New Zealand scientists undertake the first 3D colour x-ray. [Web article] 2018 July 15.
38. Thompson, A. The first 3D colour X-ray: Scientists create a scan that takes the clearest pictures yet of the human body to help boost accuracy of diagnosing diseases. [Web article] 2018 July 11.
39. Wehner, M. Full-color 3D X-rays are the future, and here's what they look

like. Science [Web article] 2018 July 13.
40. Yan, L. See Bones, Blood and Tissue in World's First 3D Colored X-Ray. [Web article] 2018 July 15.
41. Nature. The month's sharpest science shots - selected by Nature's photo team. [Web article] 2018 August 7.
42. The verge. These 3D X-rays are spectacular and really gross. [Web article] 2018 August 14

Contents

Chapter 1

Introduction

This chapter presents my research goals and outlines my personal motivation for this research. The significance of my work is visualised through some remarkable images that demonstrate the applications of the MARS small bore scanner. I also present the first human images from the MARS large-bore scanner. This is followed by a brief introduction to diagnostic x-ray imaging, which leads to an introduction to the MARS spectral imaging technology and the MARS technology relevant to this thesis. The chapter concludes with a description of the thesis outline.

1.1 Thesis goals and significance

The energy response of the MARS system is governed by the Medipix3RX detector, and characterising it plays a critical role in the MARS imaging chain. The novel work presented in this thesis develops a model and methods to characterise the Medipix3RX detector to produce more clinically useful MARS images. The long term motivation for this thesis goal is to provide economic and health benefits to New Zealand.

My personal motivation for this research stems from my curiosity about fundamental physics principles. I love investigating how and why things happen the way they do. Being able to apply my curiosity to something as ground breaking

as the MARS technology makes me very excited, and the possibility that I can help people using my curiosity is astounding.

The significance of the work presented in this thesis is visualised through the potential applications of the MARS imaging system. Characterising the energy response of the Medipix3RX detector has a direct effect on the quality of the images obtained. An improved understanding of the energy response offers more applications of MARS. This lifts the profile and competitiveness of New Zealand's technology manufacturing sector in the area of medical imaging. Before introducing the MARS team and technology, I present some applications of the MARS spectral imaging system. The images I present below have been used with permission and are owned by MARS Bioimaging Ltd. (MBI), unless stated otherwise.

Contrast imaging

The MARS spectral imaging system has the potential to offer personalised medical care by monitoring disease progression and drug delivery [Anderson et al., 2010]. MARS scanners enable simultaneous identification and quantification of multiple contrast agents, in a single scan [Anderson and Butler, 2014]. Figures 1.1a and 1.1b show the differentiation and quantification of materials with different concentrations in a multi-contrast phantom and in a mouse, respectively.

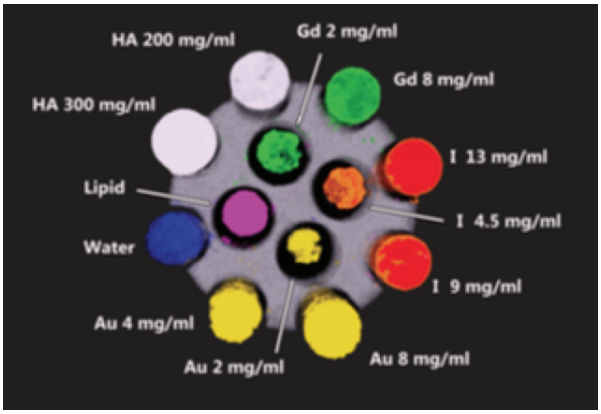

(a)

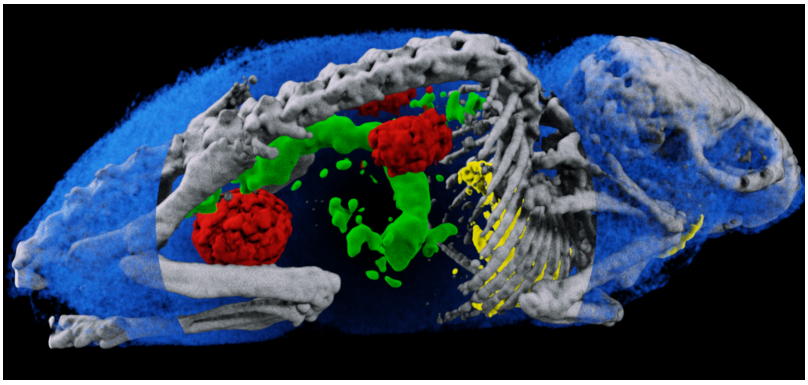

(b)

Figure 1.1: Simultaneous differentiation and quantification of four high-Z materials in (a) a multi-contrast phantom, and (b) a mouse. For easy visualisation, a separate colour is assigned to each material. For the mouse image the water has been partly removed to indicate four contrast materials: calcium (bone), gold (in the heart and blood vessels), gadolinium (in stomach), and iodine (in pelvis and bladder). Images retrieved from [Moghiseh et al., 2016].

Soft tissue imaging

MARS spectral imaging provides better soft tissue contrast than is available with traditional x-ray systems. This enables imaging of pathological features, such as cardiovascular disease, at high spatial resolution. Figure 1.2 shows a MARS image showing different components of an excised human carotid plaque. Another application of soft tissue differentiation in MARS is shown in figure 1.3 where fat, meat and bone are separated in a lamb chop. As a part of a 400-level research

project I was a part of this research and am a co-author on the published paper [Aamir et al., 2014].

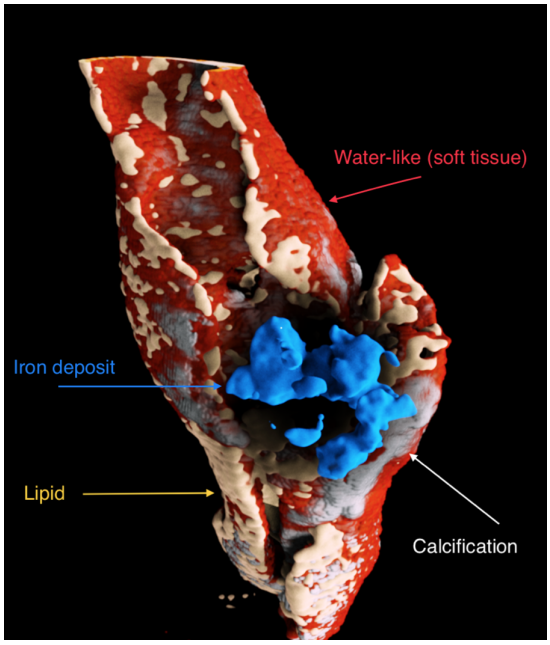

Figure 1.2: Atherosclerosis is the hardening and narrowing of the arteries. The MARS image of the atherosclerotic plaque shows the soft tissue in red, the lipid in beige, the calcifications in white, and the presence of a blood clot in blue. Image retrieved from Prebble [2018].

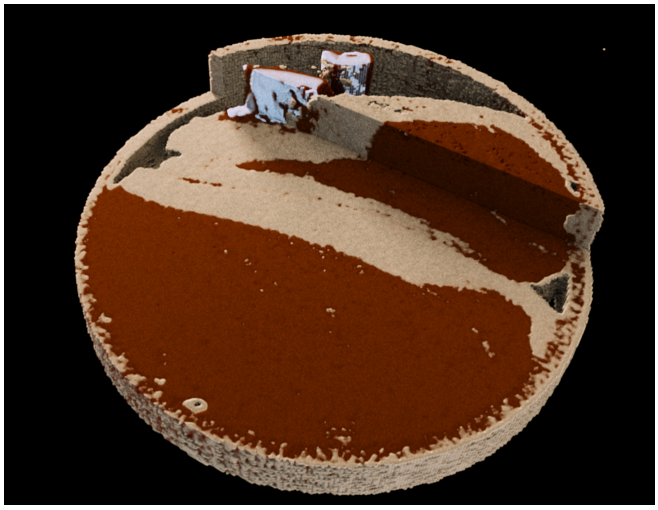

Figure 1.3: A slice through of a MARS image of a lamb meat sample. Clear separation of fat (beige), meat, and bone (white) can be seen in the meat structure. This is advantageous to the meat industry. Image retrieved from [Aamir et al., 2014].

Bone and joint imaging

MARS enables structural and material information to be measured simultaneously. This means that bone density can be measured, in addition to architectural features such as cortical thickness, trabecular thickness, and trabecular spacing. Furthermore, biomarkers of cartilage health can be measured (including early measures of osteoarthritis). Figure 1.4 demonstrates quantitative cartilage imaging using the MARS scanner.

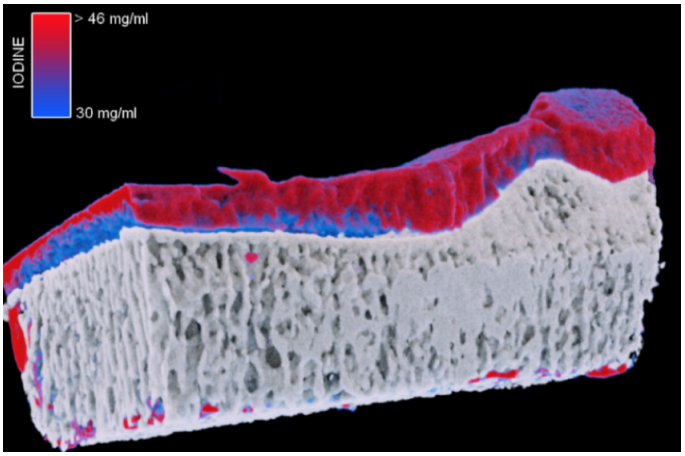

Figure 1.4: 3D rendered volume of an excised human lateral tibial plateau sample. Calcium and iodine are quantified simultaneously. A gradient of colours (from red to blue) indicates concentration of iodine as a reverse marker of cartilage health. This is useful in assessing the deterioration of cartilage in osteoarthritis. Image retrieved from [Rajendran et al., 2017].

Human imaging

In May 2018 the first diagnostic quality images of a living human were obtained using the MARS imaging chain. MARS-14, which is the human/large-bore system, was used to obtain the images. In July 2018 the images were published for the rest of the world to see. Figures 1.5 and 1.6 show images of a person's ankle/foot and wrist, respectively. These images prove that the MARS small bore scanner can be upscaled to image live humans and produce clinically relevant images. Existing research with small bore MARS scanners indicates that there is a benefit to the diagnosis and treatment around cancer, bone health, vascular disease and pharmacology. Development of the large bore MARS scanner enables a pathway from pre-clinical small bore research to clinical trials in humans.

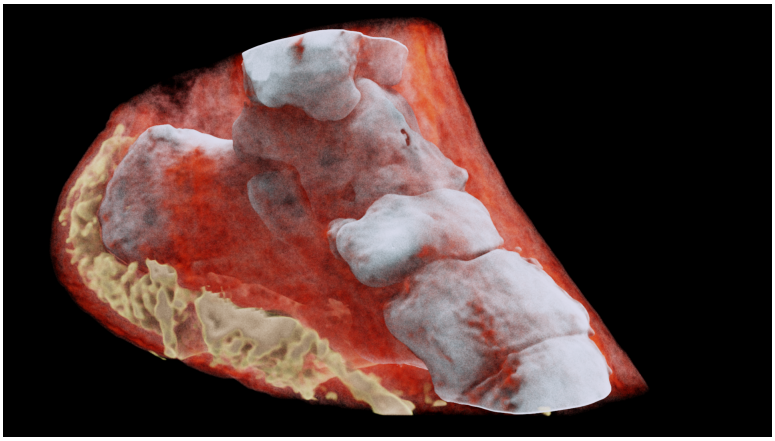

Figure 1.5: A 3D MARS image of an ankle viewed from the side where the soft tissue (coloured in red) has been made translucent to show the bones (white) and lipid-like material (yellow) inside the ankle. Image retrieved from [MARS, 2018].

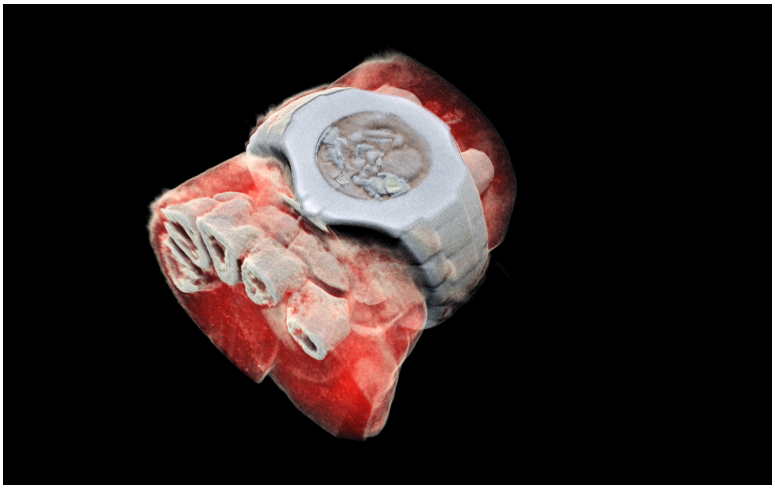

Figure 1.6: A 3D MARS image of a wrist with a watch showing part of the finger bones in white and soft tissue in red. Image retrieved from [MARS, 2018].

1.2 Diagnostic x-ray imaging

X-ray imaging was introduced as the one of the first medical imaging techniques shortly after the discovery of x-rays by W.C. Röntgen in 1895. X-ray imaging has continued to evolve while new imaging modalities, such as magnetic resonance (MR), positron emission tomography (PET) and ultrasound, were established.

Today, the applications of x-ray imaging are numerous. An overview of clinical applications for important diagnostic and interventional x-ray modalities is provided in Spahn [2013].

"Healthcare systems are subject to continuous adaptations, following trends such as the change of demographic structures, the rise of life-style related and chronic diseases, and the need for efficient and outcome-oriented procedures" [Spahn, 2013]. These developments affect the design and performance of current, and future x-ray systems. An example of such a system is computed tomography (CT), which is the focus of this thesis. "Future developments of x-ray detectors will have to support the increasing clinical demands and new applications, assist improved workflows, reflect the increasing awareness of efficiently utilising x-ray dose, and be cost efficient" [Spahn, 2013].

Computed tomography (CT) was introduced in the early 1970's by G. N. Hounsfield, and is an imaging technique based on the reconstruction of the linear x-ray attenuation coefficients. To obtain material information from CT images, energy-integrating detectors were developed. The traditional energy-integrating detectors used in CT systems capture transmitted polychromatic x-rays as a single measurement and each detector pixel integrates all the photon energies into a composite signal. In energy-integrating detectors the contribution of each photon is weighted in proportion to the energy of photon ($\sum n_E E$) and the photon statistics are not known. This x-ray detection mechanism is good for anatomical imaging, but suffers from various imaging artefacts related to the loss of the photons' energy information. The diagnostic x-ray range for most imaging modalities is 20 - 150 keV.

Dual-energy CT was the first attempt towards exploiting spectral signatures of materials such as tissue types and contrast pharmaceuticals to extract energy-specific information. Duel energy CT uses switching of the x-ray source. The attenuation of x-rays by materials are measured at two energy ranges, and using basis decomposition methods [Alvarez and Macovski, 1976; Johnson et al., 2007; Liu et al., 2009] , dual-energy CT data (attenuation information) can be

transformed into material images (density quantification). While the dual-energy approach has been successful in several clinical applications, the number of energy ranges (bins) is limited to two, and comes at a cost of increased radiation dose.

The next major shift in x-ray imaging began with the emergence of spectroscopic photon-counting detectors, such as the Medipix family of detectors [Ballabriga et al., 2016]. The Medipix spectroscopic photon-counting detector is able to resolve photons of different energies and is the detector used for the research in this thesis. Further information on the Medipix spectroscopic photon-counting detector is found in chapter 2.

A photon-processing detector is a spectroscopic detector that has energy-discriminating capabilities. A photon-processing detector measures the energy of each photon ($n_E = \{n_1, ..., n_5\}$) and the photon distribution is governed by Poissionian statistics. Medipix photon-processing detectors allow simultaneous acquisition of two to eight energy bins and each photon's energy is measured.

The energy ranges (bins) are user-defined and, therefore, provides flexibility and customisation for a wide range of medical and industrial applications. In photon-processing detectors, all x-ray energies receive equal weighting which improves soft tissue contrast unlike energy integrating detectors where high energy photons receive more weighting than low energy photons resulting in poor soft tissue contrast [He et al., 2013]. More importantly, pixelated photon-processing detectors are designed to operate at low x-ray flux, and have the potential to reduce radiation dose [Watt et al., 2003].

1.3 MARS spectral imaging

The MARS system is a spectral imaging modality capable of resolving spatial, temporal and spectral data. At the heart of this system is the spectroscopic Medipix (pixelated) photon-processing detector developed by the Medipix collaboration at the European Organisation for Nuclear Research (CERN) in Geneva,

Switzerland. The company, MARS Bioimaging Ltd (MBI), was founded in 2007 to commercialise the MARS technology by productising the scanner and selling it to biomedical users around the world. MBI is the leading manufacturer of small-animal (small-bore) spectral scanners and has recently developed the world's first spectral human imaging modality. This system is known as the MARS body-part, the MARS large-bore scanner, or the MARS human scanner. As well as the health improvement benefits the MARS scanner will confer, the likely economic benefit to New Zealand will be substantial. Figures 1.7 and 1.8 show what the MARS small-bore and large-bore scanners look like, respectively.

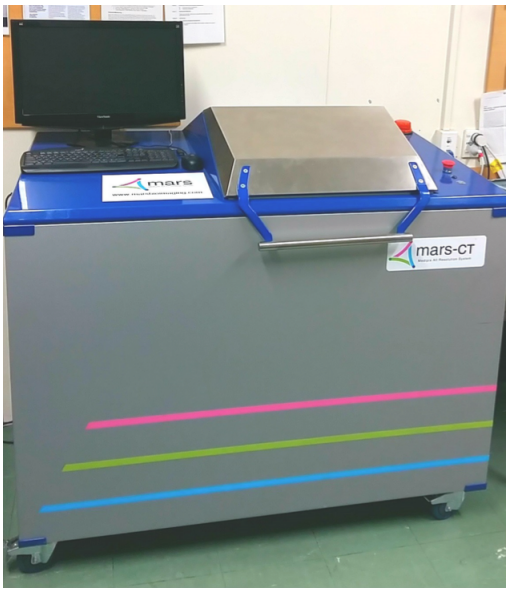

Figure 1.7: Photograph of the MARS small-bore scanner. The MARS gantry (internal part of the scanner) is discussed in more detail below.

Figure 1.8: Photograph of the first human being scanned in MARS-14 in July 2018. MARS-14 is the MARS large-bore (body-part) scanner and has the same software as the MARS small-bore scanners. Image retrieved from MARS [2018].

1.3.1 The MARS gantry

Figure 1.9 shows what the MARS small-bore scanner interior looks like. It is known as the MARS gantry and has the following modules: (1) the Medipix detector with its readout unit, together termed the "MARS camera", (2) a 50 μm x-ray tube (SourceRay Inc, NY), (3) a sample mount, (4) a camera mount that can be moved up or down, and (5) a gantry rotational motor control. An external voltage source is used to supply the bias voltage to the sensor. This voltage varies depending on the sensor material. The module of primary interest in this thesis is (1), the MARS camera.

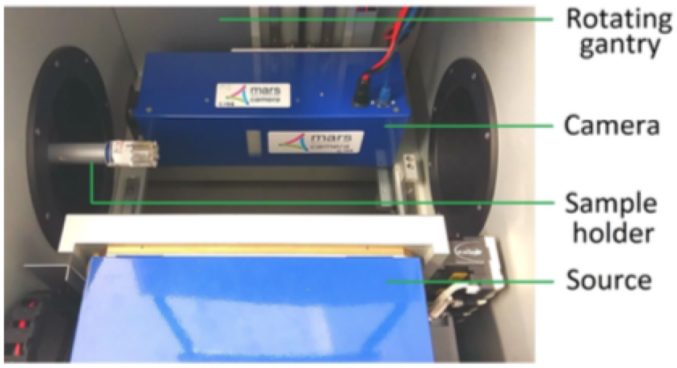

Figure 1.9: A top view of the inside of the MARS gantry inside the small-bore scanner, specifying the MARS camera and the polychromatic x-ray source that rotates around a sample mounted on a sample holder. Image retrieved from Atharifard [2017].

1.3.2 The MARS camera

The MARS camera consists of the Medipix detector chip(s) and its readout board(s). The Medipix detector is what makes MARS data spectral data. The Medipix detector is made up of a semiconducting sensor layer made from materials such as silicon (Si), gallium arsenide (GaAs), cadmium telluride (CdTe) or cadmium zinc telluride (CdZnTe also known as CZT), and an application-specific integrated circuit (ASIC). The sensors are bonded to the ASIC via uniformly spaced bump bonds, as shown in figure 1.10.

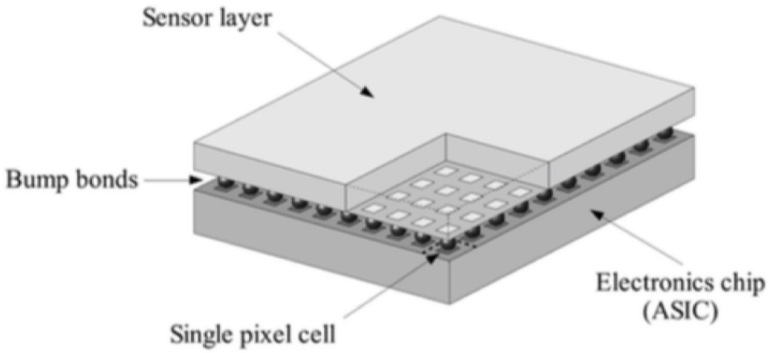

Figure 1.10: A schematic view of a hybrid pixel detector. It consists of a sensor layer and a readout ASIC that are connected via uniformly spaced bump bonds (flip bond technology). Image retrieved from Pfeiffer [2004].

In the latest versions of the MARS small-bore scanners (and the large-bore scanner), multiple detector chips are used to allow an increase in the volume of the object that is being scanned (allow larger objects to be imaged faster). Figure 1.11 shows an example of a MARS 3-chip camera, consisting of three sensor layers, three Medipix ASICs, and solder (bump) bonds between each sensor and ASIC module. The MARS camera is termed a multi-detector-element camera. For the experimental results (chapter 4) presented in this thesis, a 3-chip MARS camera is used. Figure 1.12 shows a MARS 7-chip camera. The MARS 3-chip camera looks very similar but has four less sensors and ASICs. In the remainder of this thesis, when I refer to the term "MARS camera", I refer to a MARS three-chip (three-detector-element) camera, unless otherwise specified.

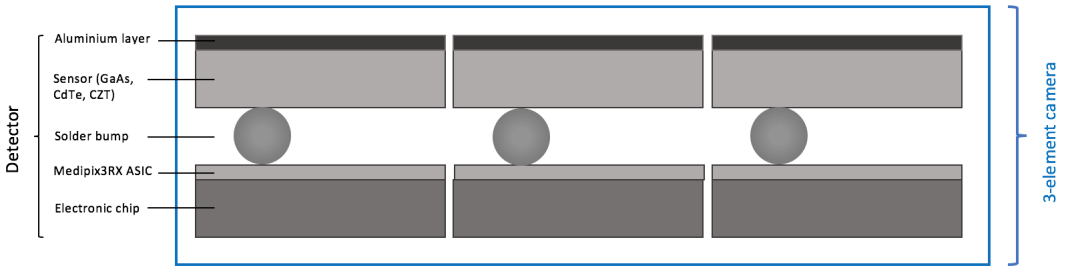

Figure 1.11: Side view of a MARS three-detector-element camera. consisting of three sensor layers bonded to three ASICs.

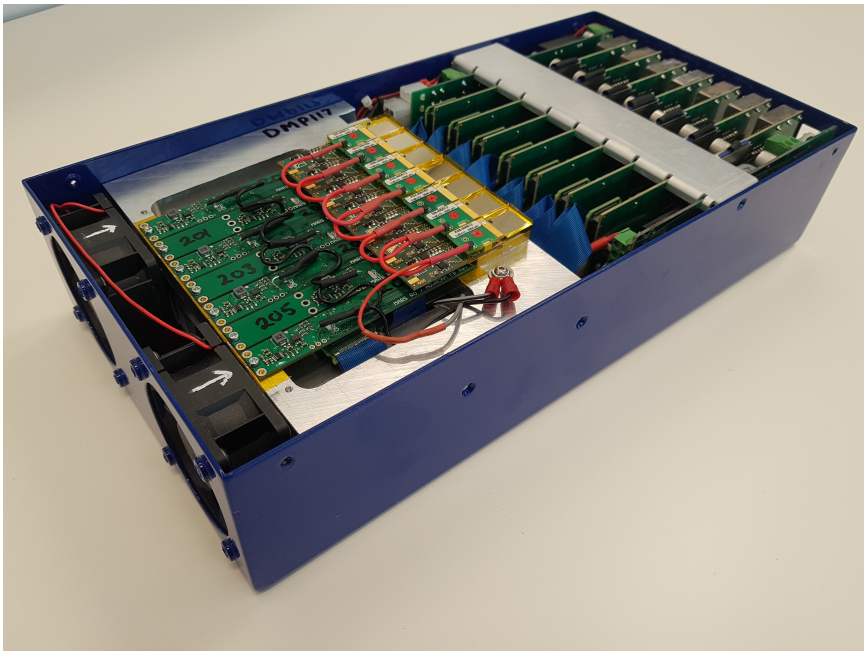

Figure 1.12: This is a picture of the MARS 7-detector-element camera where each element in the camera is Medipix3RX bump bonded to a 2 mm thick CZT sensor.

Different versions of Medipix detectors have been released. The Medipix3RX version is currently used inside MARS scanners. The Medipix3RX has 128×128 pixels, each containing 8 counters (1 arbitration counter, 3 charge summing mode (CSM) counters and 4 single pixel mode (SPM) counters). The Medipix3RX measures 14.1 by 14.1 mm. More detail about the Medipix3RX detector is given in chapter 2. The Medipix4 is set for release in 2020.

1.3.3 The MARS imaging chain

MARS images are obtained using the imaging chain illustrated in figure 1.13. The MARS scanner, with a calibrated detector, acquires projection images (DICOM format) which are transferred to a Picture Archival and Communication System (PACS). A MARS workstation located on-site or off-site can request and acquire specific datasets from the PACS for preprocessing and reconstruction. The reconstructed data is then visualised on the MARS Vision workstation. This entire MARS imaging chain is extremely complex and a large proportion of the MARS team's efforts are put into the development of the imaging chain. Each process contributes to the quality of the final image. The work in this thesis contributes to the improvement of the processes in blue in figure 1.13. The primary goal of this thesis is to characterise the energy response of the Medipix3RX detector to calibrate the MARS scanner. This has direct implications on the reconstruction algorithm. It will speed up reconstruction times, and minimise the amount of user intervention required.

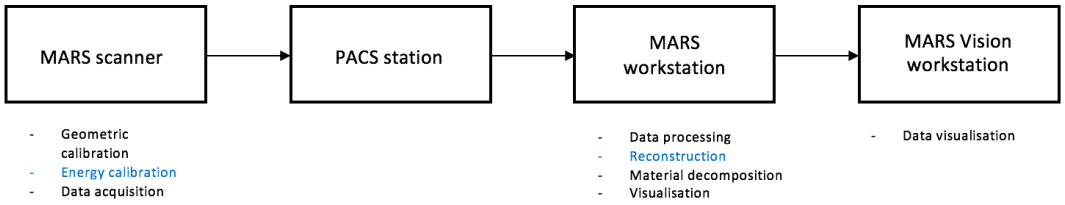

Figure 1.13: This figure shows a schematic representation of the MARS imaging chain. The work relevant to this thesis is shown in blue.

1.4 Thesis outline

The work in this thesis improves the spectral performance of the Medipix3RX detector by characterising its energy response. This makes material analysis with the MARS scanner more accurate, and in turn makes the MARS images more medically useful. This thesis is a continuation of the work started in my MSc [Vanden Broeke, 2015]. The thesis is structured as follows:

- Chapter 1 provides an introduction to the thesis. It demonstrates the capabilities of the MARS small-bore scanner and shows preliminary results of the MARS large-bore scanner. It introduces the MARS project and highlights the significance of my work.
- Chapter 2 provides a scientific background relevant to this thesis. The basic physics behind x-ray fluorescence (XRF) creation is described, and the detection of x-rays with the Medipix is detailed.
- Chapter 3 develops a model that simulates XRF creation and detection in MARS.
- Chapter 4 discusses the optimal MARS setup for creating and detecting XRF (based on the model in chapter 3) and shows experimental results.
- Chapter 5 uses the experimental results in chapter 4 to develop a method to characterise the energy response of the Medipix3RX detector.
- Chapter 6 concludes this thesis and discusses the future directions of this research.

Chapter 2

Background

This chapter provides an introduction to the production of x-rays. The interactions of x-rays with matter, in particular photoelectric absorption with respect to the creation of x-ray fluorescence, is discussed. The principles of x-ray detection with the Medipix3RX are detailed, with particular focus on the energy calibration of the detector. An understanding of the basic physics principles in this chapter are paramount to understanding the ideas that are developed in the following chapters of this thesis.

2.1 Production of x-rays

X-rays are an important tool for imaging the inside of an object. The use of diagnostic radiology has significantly increased over the past two decades [Smith-Bindman et al., 2008]. One of the most commonly used diagnostic imaging modalities in hospitals is known as computed tomography (CT). Rates of imaging with CT are three times as high as they were in 1997 and nearly overtake ultrasound imaging as the most common imaging modality. This trend is likely to continue [Spahn, 2013]. The technology developed in this thesis is a spectral CT scanner which uses the energy information of x-rays to compute the 3-D internal structure of an object from a set of 2-D x-ray images. The production of x-rays is briefly discussed below.

X-rays are generated when high energy electrons interact with matter. In medical imaging, x-rays are nearly always created in an x-ray tube [Johns and Cunningham, 1983]. Inside the x-ray tube, two types of electromagnetic radiation are generated: characteristic radiation and bremsstrahlung (braking) radiation. A typical x-ray spectrum is shown in figure 2.1. In this, we can see several discrete, characteristic, energy peaks superimposed on the continuous bremsstrahlung spectrum. The intensity of the x-ray spectrum is determined by the energy of the electron beam which creates it. The electron energy also determines the shape of the bremsstrahlung spectrum, in particular, the end point of the spectrum.

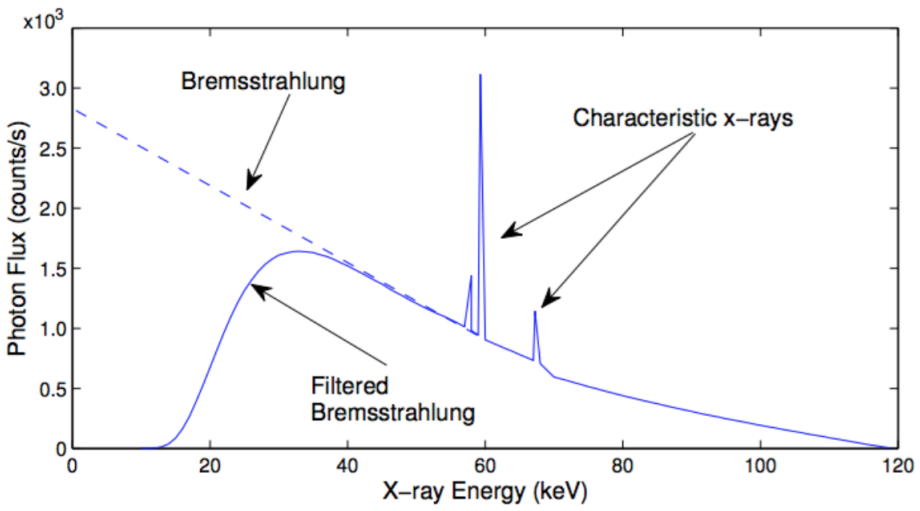

Figure 2.1: Bremsstrahlung radiation shows a continuous polychromatic spectrum with discrete characteristic x-ray peaks. The end point of the spectrum is determined by the energy of the electrons which create it. Image retrieved from Bateman [2015].

2.2 Interaction of x-rays with matter

There are two basic types of energy transfer that occur when x-rays interact with matter: (1) ionisation; and (2) excitation. There are many known processes that can occur when x-rays interact with matter, however, only three of these processes play a role in diagnostic radiology. These processes are: (1) Rayleigh scattering; (2) Compton scattering; and (3) photoelectric absorption. Understanding the

physics principles behind photoelectric absorption is fundamental to the work presented in this thesis. In photoelectric absorption, the emission of characteristic x-rays from a material that has been excited by bombarding with high energy x-rays is also known as x-ray fluorescence (XRF). For the remainder of this thesis, characteristic x-rays are referred to as x-ray fluorescence. A detailed account of x-ray interactions in diagnostic radiology is found in [Attix, 2008].

2.2.1 X-ray fluorescence

An atom is comprised of orbital shells labelled (K, L, M, N, ...) which correspond to the principal quantum numbers 1, 2, 3, ... Each shell of an atom is subdivided into sub-shells which are made up of orbitals (s, p, d and f). Discrete transitions, due to photoelectric absorption, between atomic shells and sub-shells give rise to x-ray fluorescence (XRF). Therefore, XRF is discrete, material specific, and monochromatic. XRF is named according to the orbital in which the photoelectric absorption (electron vacancy) occurred. The energy of the XRF photon is the difference between the electron binding energies of the respective shells. A detailed account of XRF creation is found in Podgorsak et al. [2005]. The energies of various K-shell fluorescence photons for materials relevant to this thesis are shown in table 2.1. In this thesis I only investigate $K_{\alpha 1}$ XRF photons as they have the strongest XRF signal and highest yields [Berger, 2010].

Atomic number	Target material	K_α energy (keV)	K_β energy (keV)
42	molybdenum	17.48	19.61
49	indium	24.21	27.27
60	neodymium	37.36	42.27
66	dysprosium	46.00	52.18
73	tantalum	57.53	65.21
82	lead	74.97	84.92

Table 2.1: Average XRF K_α and K_β energies for various target materials [Berger, 2010].

2.3 X-ray detection

X-rays are quantised (photons) and they possess intrinsic energy that is imparted to the matter it interacts with via atomic ionisation or excitation. In order to detect x-rays you have to transfer energy from the photon to a detector which is able to convert the x-rays into electrical signals. Based on the mechanisms of conversion, the detection systems are classified as direct or indirect systems. Details on each type of detection system is found in Attix [2008]; Johns and Cunningham [1983]; Podgorsak et al. [2005]. In the direct detection systems, the conversion of the radiation to an electrical signal occurs directly in a semiconductor layer. Ballabriga [2009] discusses that the two-step mechanism of the indirect detection systems degrades spatial resolution and efficiency of the detection process, therefore the choice of direct conversion technology is more suitable for spectral imaging.

2.3.1 Hybrid pixel detectors

A common design of the direct detection systems is the hybrid pixel detector which has a sensor layer and a readout chip on different substrates. The two layers are connected using the bump bond technology. Both sensor and the readout electronics are segmented into very small units referred to as detector pixels. Figure 2.2 shows that each pixel of the sensor is connected to its own electronics in the readout application-specific integrated circuit (ASIC). An advantage of the hybrid architecture is that it allows an independent optimisation of the sensor and the electronic circuitry. Furthermore, it provides an application-specific use of sensor materials in combination with the readout ASIC. The Medipix family of the detectors used in the MARS scanner are an example of hybrid pixel detectors.

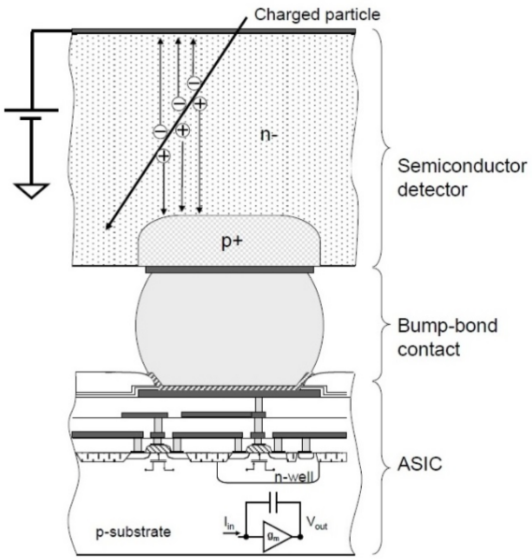

Figure 2.2: The side view of a Medipix pixel with the sensor layer bump bonded to the ASIC. Photons interact with the semiconductor material to produce a signal in the ASIC. An externally applied bias voltage drives the charge carriers, that are created in the sensor layer, toward the ASIC. The exact mechanism of this is discussed in section 2.4.2 below. Image retrieved from Ballabriga [2009].

2.3.2 Photon-processing detectors

Photon-processing x-ray detectors with energy discrimination capabilities are essential in spectral CT. The energy discriminating characteristics of the x-ray photon are exploited by assigning the incident x-ray photon to one of several energy bins (channels) via a pulse height analysis. The number of energy channels per detector pixel in photon-processing detectors varies from 2 to 8, depending on specific detector designs [Taguchi et al., 2011]. The Medipix series of detectors are an example of energy-discriminating photon-processing detectors in a hybrid design. The MARS project is the first human imaging system to use such detectors to create spectral images (with commercial goals). The Medipix detectors are described in the next sections of this chapter.

2.3.3 The Medipix detectors

A brief introduction to the Medipix series of detectors is given in chapter 1. More detail is given in the section below. In the Medipix detector, both the ASIC and CMOS layers are pixellated. The small pixel size gives a high contrast between different materials and a high spatial resolution [Zeller et al., 2009]. The Medipix detector offers substantially more information regarding the object being imaged. Three generations of the Medipix detector chips have been successfully developed. The detector used for the results presented in this thesis is the Medipix3RX energy-discriminating photon-processing detector, which is discussed in detail below.

2.4 Medipix3RX

The Medipix3RX active area is formed by a square matrix of 256×256 pixels. Each pixel measures $55\mu\text{m} \times 55\mu\text{m}$, though this can vary slightly due to charge steering [Ballabriga et al., 2013]. The regular structure in the matrix is implemented as a cluster composed of 2×2 pixels with different circuitry. In the spectroscopic mode of operation only one pixel in the cluster is bump bonded. From here on out the word "pixel" will be used to refer to a cluster of pixels (2×2) and the Medipix3RX is said to have 128×128 pixels of size $110\mu\text{m} \times 110\mu\text{m}$.

2.4.1 Pixel architecture

The pixel architecture of the Medipix3RX is very similar to what I have shown in figure 2.2. Each pixel has an analogue and a digital part [Ballabriga et al., 2013]. Charge is collected on a pixel and integrated by a Charge Sensitive Amplifier (CSA). A digital-to-analogue converter (DAC) determines the global energy threshold in the analogue section of the pixel. The same global energy threshold is set across the entire detector matrix (all pixels).

2.4.2 Energy binning in the Medipix3RX

When photons strike the detector, electron-hole pairs are created in the sensor layer. The electron-holes are separated by an external electric field and drift toward the collection electrodes. The speed of this drift is determined by the bias voltage. An electrical pulse is created whose magnitude is proportional to the photon energy associated with the event [Walsh et al., 2013]. The discriminator (in the analogue section of the pixel) compares the height of the pulse to thresholds selected by the user. The thresholds are set via an energy threshold DAC, and each pixel sees the same threshold. If the pulse height of the charge is higher than the energy threshold DAC, the counter in the digital section of the corresponding pixel is incremented in the image processing part of the MARS imaging chain. At the end of charge collection, the number of the charge carriers above each counter are subtracted from the number of charge carriers in the previous counter. This creates an energy bin which is also called an energy channel.

The counters include four CSM, three SPM and one arbitration counter. The threshold of the arbitration counter is set above the noise floor and below the x-ray spectrum's peak energy. At present the three SPM counters are not used in MARS imaging. So, even though the Medipix3RX is capable of assigning an incoming photon to one of eight energy bins, only five are used. Figures 2.3a and 2.3b demonstrate how the spectrum is divided into five energy bins. Spectral information is acquired from having multiple bins.

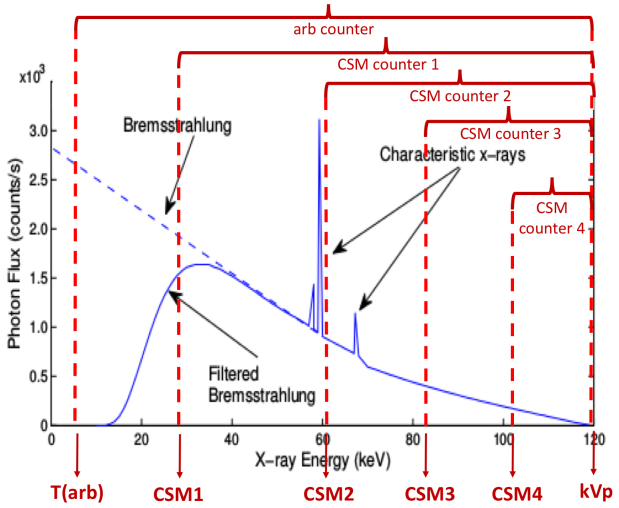

(a) Unsubtracted energy bins.

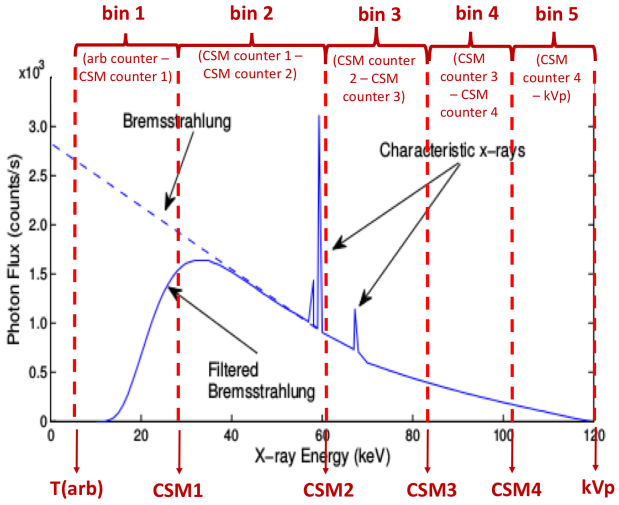

(b) Subtracted energy bins.

Figure 2.3: These figures show the (a) unsubtracted, and (b) subtracted energy bins for the current mode of operation in the Medipix3RX detector. The boundaries of the energy bins are known as the counters. T(arb) is the arbitration counter, CSM1-CSM4 mark the charge summing counters, and the kVp is not a counter but it is a boundary (i.e., there should be no photon counts above the kVp). Subtracted energy bins can be calculated from unsubtracted energy bins by subtracting two of the energy bins. For example, CSM counter 1 minus CSM counter 2 in subfigure (a) will yield energy bin 1 in subfigure (b). This makes the energy channels independent of each other with non-overlapping energy ranges. By subtracting the values in the counters, not doing anything physical to the counters, or subtracting their thresholds, the bin range is determined. If a photon of energy 50 keV was incident on the detector, it would be assigned to bin 2.

2.5 Energy calibration

The accuracy of the material information acquired in MARS spectral scans relies on the accuracy of the counters (boundaries of the energy channels). Small variations in the counter accuracy (by accuracy I mean the difference between what the user sets and what the electronics set) affects the performance of energy-discriminating photon-processing detectors by degrading the energy resolution. An energy calibration helps to prevent this by evaluating a relationship between the energy of an incident photon and the energy bin it is assigned to.

Calibrating the energy response of photon-processing detectors is achieved using various methods. Typically these are based on measurements of monochromatic x-rays which are generated from either metallic foil XRF [Ballabriga et al., 2013, 2011; Ronaldson et al., 2011], synchrotron radiation [Gimenez et al., 2011], or radioactive sources [König, 2011]. However, it is also possible to calibrate using the kVp energy of a polychromatic x-ray spectrum [Panta et al., 2015a]. Each of these four calibration sources present their own limitations and difficulties in calibrating photon-processing detectors in spectral CT setups. Firstly, XRF can be contaminated by polychromatic x-rays from the x-ray source that is used to induce excitation in the foil. Secondly, synchrotrons require a large physical space for their setup and have significant cost. Thirdly, long measurement times are needed for radioactive sources which raises the issues of safety and storage. Lastly, the accuracy of the kVp methods are limited by the voltage ripple of the x-ray tube and the low numbers of photons near the kVp energy [Schlomka et al., 2008]. XRF for energy calibration is discussed in detail in chapter 4.

2.5.1 Accuracy of energy calibration

If the global energy calibration is not accurate, the detected XRF signal will be distorted [Panta et al., 2015a] and the signal will appear to be smaller, and therefore may not be detected. This is demonstrated in figure 2.4 where the blue line represents an accurate global energy calibration where the XRF pulse has a gaussian shape and is detectable. The red line represents a“bad” global energy calibration where the resulting XRF pulse is distorted, has a low intensity, so

is not easily detectable. This demonstrates how the global energy calibration impacts the detected XRF peak.

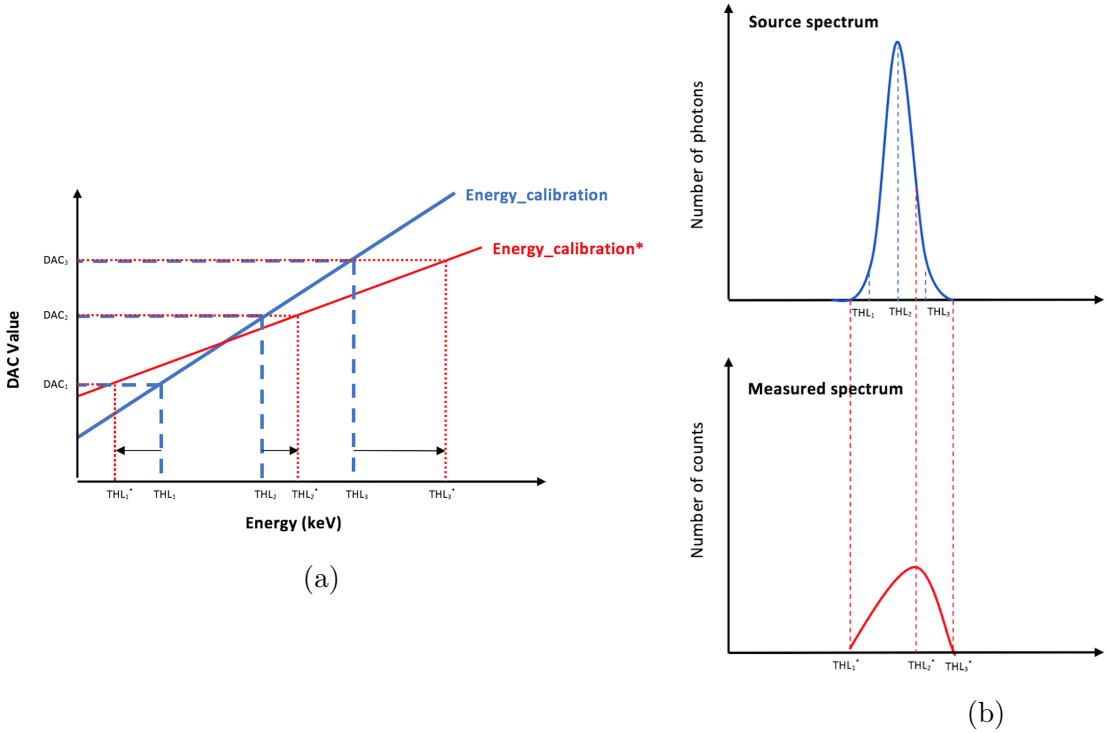

(a)

(b)

Figure 2.4: These figures show the importance of an accurate energy calibration. The blue and red lines in (a) present a small difference in the energy calibration slope and offset. This has a large effect on the strength of the XRF spectrum detected in (b). The XRF peak has shifted to the right and has considerably reduced in size.

2.6 Pulse pileup and charge sharing

Additional factors that limit the energy resolution of the Medipix detectors are pulse pile-up and charge sharing. Pulse pileup combines two consecutive photon events into a single photon event (pulse) because the time interval between the two successive pulses in the detector is so small [Taguchi et al., 2011]. This affects the energy resolution and count rate of the detector [Zeller et al., 2009]. A pulse pile-up correction for MARS has been investigated by Atharifard [2017]. He developed a model to simulate the pileup effect in the Medipix3RX. This model

is yet to be implemented into the MARS imaging chain, however, it will allow a substantial decrease in the scanning time (as higher flux rates are able to be used).

An incident photon creates a three-dimensional charge cloud in the detector which may span across several adjacent pixels. Charge sharing occurs when the pixels have to "share" the collected charge. Charge sharing distorts the energy spectrum of the pixels that are involved in the sharing by appearing as several lower energy photons interacting in the pixels [Koenig et al., 2013]. The Charge Summing Mode (CSM) in Medipix3RX ASIC is an advanced mode of operation that is designed to account for the charge sharing effect in photon-processing detectors [Ballabriga et al., 2013].

2.7 Summary

- A typical x-ray spectrum consists of a continuous (polychromatic) bremsstrahlung spectrum and discrete (monochromatic) characteristic radiation.
- When x-rays interact with matter through the photoelectric effect, x-ray fluorescence (XRF) is produced. XRF is monochromatic characteristic radiation. The naming of the XRF depends on which atomic shell or sub shell the photoelectric interaction took place.
- Photon-processing detectors have a hybrid pixel structure. They are advantageous in multi-energy CT because of their energy discriminating features. These features are based on the pulse height analysis of an incident x-ray where it assigns the x-ray photon to one of several energy channels.
- The Medipix3RX is the current energy-discriminating photon-processing detector used inside the MARS scanners and is able to assign an incoming x-ray photon to one of five energy bins (channels).
- An inaccurate energy calibration degrades the energy resolution of energy-discriminating photon-processing detectors. An energy calibration develops a relationship between the energy of an incident photon and the energy bin it is assigned to.
- Pulse pileup and charge sharing limit the energy resolution of the Medipix3RX detector.

Chapter 3

Modelling oblique x-ray fluorescence in MARS

An accurate selection of energy ranges is highly important in spectral CT to maximise the differential x-ray attenuation between materials. This improves material classification and hence image quality in MARS. In this chapter I develop an analytical model that quantifies x-ray fluorescence (XRF) production and detection in MARS. XRF is used to characterise the energy response of the Medipix3RX detector and improves material discrimination. The model developed in this chapter breaks down aspects of the physical system. Modelling the XRF is a way towards successfully measuring the XRF, without having to do time consuming experiments. The model's output is used to determine the optimal settings for many user-defined scanner parameters. The next chapter of this thesis uses the model's results to experimentally detect XRF in MARS.

This chapter is organised as follows. Section 3.1 gives a brief overview of calibrating the energy response of photon-processing detectors using XRF. Next, a comprehensive description of the development of my XRF model is given in section 3.2, where the physics involved in XRF production is described mathematically in section **??**. Then, the modelled XRF distribution for molybdenum, tantalum and lead foil materials are given in section 3.3, and the optimal detector positions for detecting molybdenum XRF for different collimator positions are

presented in section 3.3.1. In section 3.5 the XRF model is validated by comparing how various parameters behave physically, and in the model. An important finding regarding the source-to-detector distance is given in section 3.5.4. Lastly, section 3.6 discusses the model's significance and limitations.

I was the lead researcher in this study, developing the fluorescence model on Matlab, and interpreting and analysing the results. The model presented in this chapter has resulted in one publication where I am the primary author, and one conference proceeding/poster. I would like to acknowledge Dr Christopher Bateman (previous MBI employee) and Dr Ali Atharifard (MBI employee) for their contribution.

3.1 Introduction

The primary advantage of using photon-processing detectors in spectral CT is their energy discrimination capabilities. The photon-processing detector used in MARS is the Medipix3RX (chapter 2). Currently the Medipix3RX assigns an incoming photon to one of five energy channels, where the software enables each channel to measure a different energy range. Together, the different energy channels differentiate several materials simultaneously. In order to use the Medipix3RX for material identification effectively, the energy response of each channel (in every detector pixel) needs to be calibrated. Energy calibration means evaluating a relationship between the energy of the incident photon and the energy bin it is assigned to. Once the energy calibration is known, it is easy to find the energy of an unknown source (i.e., detect materials within an unknown object). An overview of energy calibration was given in chapter 2. XRF is a common technique to calibrate the energy response of photon-processing detectors

3.2 XRF model development steps

The XRF model developed in this chapter offers a fast and easy way to determine the scanner parameters that produce and detect an optimal XRF signal that can be used for calibrating the energy response of the detector. The XRF model is an analytical model that simulates the XRF from the point it is created in the foil, to the point it is detected by the Medipix3RX detector. The model is used to determine the optimal scanner parameters without having to determine them experimentally. This will save time and deepen our understanding of the fundamental physics happening in XRF creation and detection.

The XRF model output represents the XRF distribution in the detector plane. A simplification of XRF creation and detection in MARS is shown in figure 3.1. This figure represents what happens experimentally, and can be used to follow the steps of the XRF model. In XRF production the source illuminates the foil and creates many independent XRF point sources inside the foil (**B, B', ...**). The amount of XRF that reaches the detector plane, in an area **A**, from every **B** point is determined. The detector plane (DP) consists of an array of **A**'s. Then, the XRF in all the elements **A** are summed. This gives the quantitative XRF distribution in the detector plane. XRF is emitted isotropically, and we expect the XRF distribution to be maximum at the (0,0) point (of the source) and of a normal distribution.

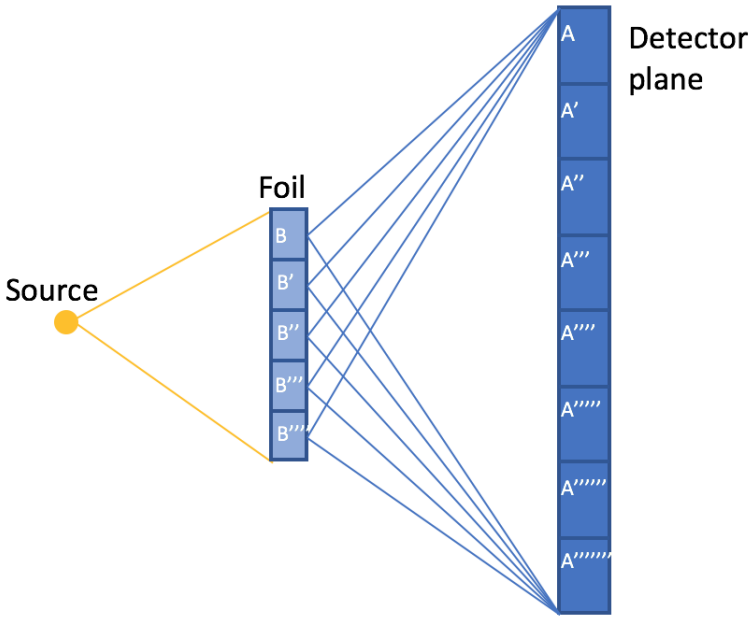

Figure 3.1: A simplification of the fluorescence creation and detection in MARS. The illuminated regions on the foil **B**, **B'**, **B"** **B"'**, and **B""** act as independent fluorescence point sources that reach a point **A**,..., **A"""'** in the detector plane. XRF emission is isotropic but is limited by the size of the detector plane in MARS.

3.2.1 XRF model workflow

Figure 3.2 depicts a detailed workflow of my XRF model. The model can be summarised by three simple steps: (1) the primary beam emission from the source; (2) the XRF creation and emission from the foil; and (3) the XRF detection by the (Medipix3RX) detector. Each step is explained in detail in the sections below.

1. Divide the foil into n layers.
2.Take the first layer (closest to the source).
3. Increment the layer into **B** elements.
4. Take the first horizontal **B** element.
5. Take the first vertical **B** element.
6. Calculate the solid angle to the element.
7. Calculate the XRF created in and escaping the element.
8. Calculate how much of the XRF can travel through the remaining layers.
9. Segment the detector plane into **A** elements.
10. Take the first horizontal DP element.
11. Take the first vertical DP element.
12. Calculate the solid angle to that element.
13. Calculate the XRF contribution in that element.
14. Repeat steps 12-13 for all vertical DP elements.
15. Repeat steps 11-14 for all horizontal DP elements.
16. Repeat steps 6-15 for all vertical B elements.
17. Repeat steps 5-16 for all horizontal B elements.
18. Repeat steps for the remaining foil layers.
19. Sum up the XRF contribution from each layer. The layer is assumed to be of infinitesimal thickness.

Figure 3.2: Detailed workflow of the fluorescence model. Each step is explained in detail below.

Step 1:

Divide the foil into multiple thin layers so that a foil of infinitesimal thickness can be assumed. The thinner the layers, the better the approximation is.

Steps 2-3:

Take the first layer and discretise into individual elements. Each element represents a **B** point. The entire foil is represented as a three-dimensional matrix of **B** points. The collimator settings determine the size (foil height and width) of the layers, while the number of foil layers is user defined. Narrow collimators give a small matrix, whereas wide collimators give a large matrix. When the entire foil is illuminated, each **B** point on the foil can be treated as an independent XRF point source. Figure 3.3 demonstrates what happens in Steps 1-3.

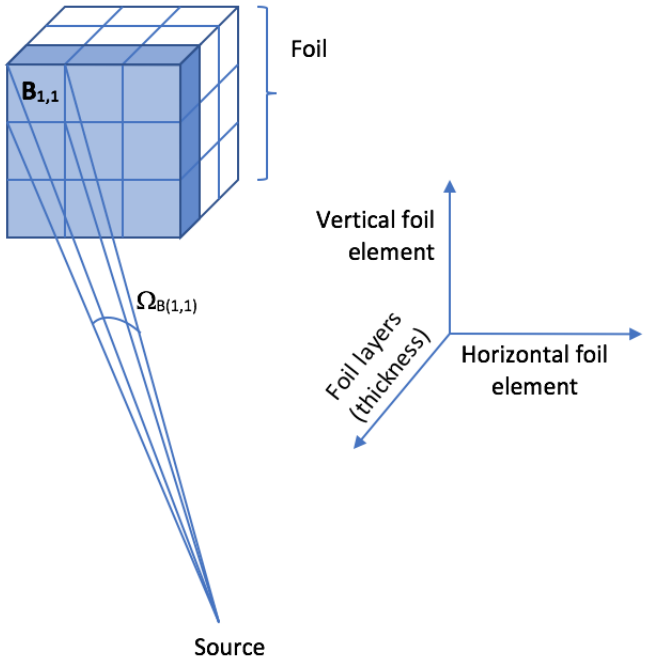

Figure 3.3: This figure represents the source beam incident on a **B** element of the foil. It shows that the foil is divided into multiple (in this case 3) layers.

Steps 4-6:

Take one specific **B** point and calculate the solid angle from the source to the **B** point. This solid angle is Ω_B and is calculated using equation 3.1. More detail about the solid angle calculation is provided in section 3.2.2.

Steps 7-8:

Calculate the amount of XRF created in each element using equation 3.2 which is introduced in section 3.2.3. Then calculate how much of the XRF travels through the remaining layers of the foil.

Step 9:

Discretise the detector plane into a two-dimensional array. Each element represents an area **A** on the detector plane. The user can choose **A** to be the size of a pixel in the Medipix3RX detector.

Steps 10-12:

Take one specific element **A** on the detector plane and calculate the solid angle from the **B** point (foil) to **A**. This solid angle is Ω_A. The solid angle calculation is described in equation 3.1.

Step 13:

X-ray photons are emitted uniformly in all directions by the source, however, only the photons incident on a single **B** point are considered. Calculate the XRF contribution in an area **A** on the detector plane, from a single **B** point, by multiplying equation 3.2 by Ω_B and Ω_A.

Note that prior to interacting with the foil the source x-rays pass through a filtration layer, typically 1.8 mm of inherent Al plus 1 mm of Al filtration. Therefore, the source beam incident on the first layer is given by the filtered MARS source spectrum. The MARS source spectrum model was developed internally by Marzi Anjomrouz and Mohammad Shamshad [Shamshad et al., 2017], and determines I_0 in equation 3.2. The consequent I_0's (for the next layers) are attenuated by the previous layer, and so on. The derivation of equation 3.2 is discussed in more detail below. The role of the filtration and possible improvements to the filter-bar design are discussed later in this chapter.

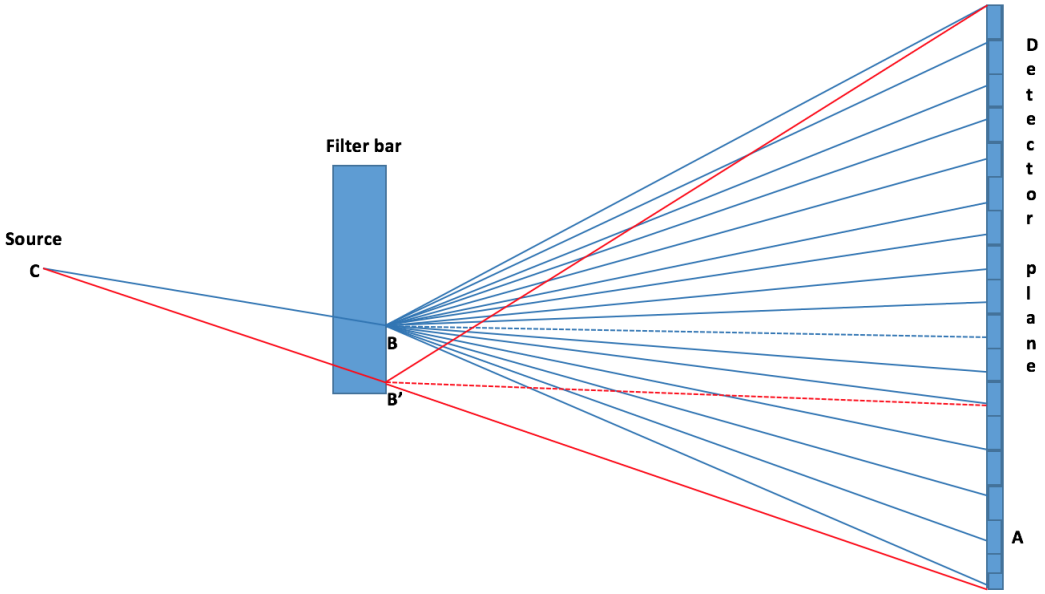

Figure 3.4: Two illuminated regions on the foil **B** and **B'** acting as independent point sources. Each point produces a different XRF flux, and the distances to the same points on the detector plane are different.

Steps 14-15:

Calculate the XRF contribution in the other areas **A** of the detector, from that single **B** point, by multiplying equation 3.2 by the same Ω_B as in Step 7, and Ω_A for another element. This is repeated for all **A** elements on the detector plane.

Step 16-17:

Steps 4-15 are repeated for all the **B** points of the foil.

Steps 18-19:

To determine the total XRF reaching different pixels/ROI's of the detector plane, contributions from all of the **B** point sources must be combined. Therefore, all XRF contributions for each **A** element are summed. This is repeated for every layer of the foil. The result is a XRF distribution, in the detector plane.

In summary, there are three types of attenuation that are taken into account by the model: (1) the attenuation of the incident source spectrum through the

foil elements prior to producing XRF; (2) the attenuation of the XRF photon through the foil element it is created in; and (3) the attenuation of the XRF photon through the remaining foil elements, i.e. a XRF photon created in the first layer will be attenuated much more (by the remaining thickness of the foil) compared to a XRF photon created in the last layer.

3.2.2 Solid angle

Solid angle calculations are essential for the XRF model. Quantifying the solid angle allows the XRF model to "follow" the physics and mathematics of what happens to a source photon from where it is created, to where it causes XRF to be detected. The solid angle is a two-dimensional angle in three-dimensional space that an object subtends at a point. It is a measure of how large the object appears to an observer looking from that point. The development of the XRF model applies two solid angle calculations: (1) from the source to an element on the foil plane, where the element is assumed to be a **B** point source; and (2) from a **B** point to an element **A** on the detector plane.

The first calculation allows me to quantify the fraction of main beam photons that hit a specific foil element, at a specific distance. The second solid angle calculation tells us how many of the XRF photons that are created in the foil, are seen by an element of the detector **A**.

There exists an analytical formula for the exact solid angles of various shapes. Of specific interest to us is that there is an analytical formula for the solid angle of a tetrahedron. The dual tetrahedron method, described in detail in an internal MARS document titled "Solid Angle Calculations", is used in the XRF model calculations. The formula is given by the equation below:

$$tan(\frac{1}{4}\Omega) = \sqrt{tan(\frac{1}{2}s)tan[\frac{1}{2}(s-\theta_{AB})]tan[\frac{1}{2}(s-\theta_{BC})]tan[\frac{1}{2}(s-\theta_{AC})]} \quad (3.1)$$

A spherical triangle, defined by the points A, B, and C, have interior angles of

θ_{AB}, θ_{BC}, and θ_{AC}. $s = \frac{1}{2}(\theta_{AB} + \theta_{BC} + \theta_{AC})$ is the semi-perimeter of a spherical surface.

3.2.3 XRF production

A very important step in the development of my XRF model is XRF production inside the foil. In my MSc thesis I developed a model that optimises the thickness of monoatomic foils to ensure that maximum fluorescence escapes the foil [Vanden Broeke, 2015]. This model was altered slightly to quantify the XRF escaping a foil of a specific thickness. There are several factors to consider when describing the production of XRF from a narrow beam of x-rays passing through a foil. Only the production of K_α fluorescence photons are considered as the production of other XRF photons, such as K_β, are considered negligible [Berger, 2010]. The number of K_α fluorescence photons escaping a foil of thickness L for an arbitrary input x-ray beam is given by:

$$N_{K_\alpha}(L) = \int_K^\infty \omega_{K_\alpha} I_0(E) \frac{\tau_{K_\alpha}(E)}{\mu_{K_\alpha} - \mu(E)} [e^{-\mu(E)L} - e^{-\mu_{K_\alpha} L}] dE \tag{3.2}$$

where K is the K-edge energy of the foil (there is no XRF produced if $E < K$), ω_{K_α} is the fluorescence yield, $I_0(E)$ is the number of x-rays of energy E in the input beam, $\tau_{K_\alpha}(E)$ is the K_α photoelectric absorption contribution to the linear attenuation coefficient, μ_{K_α} is the linear attenuation of the foil at the energy of the K_α photons, and $\mu(E)$ is the linear attenuation of the foil for photons of energy E.

The integration limits are defined for all x-rays in the incident x-ray beam with energies higher than the K-edge energy of the foil material. An approximation made in the derivation of this equation is that the thickness of the foil is infinitesimally small. To use this equation for thick foils, XRF production is calculated for different layers within the foil. It is important to note that the K_α XRF photons produced in the first layer of the foil are attenuated or scattered in the remaining foil layers after they are produced, and similarly for the following layers.

3.3 Results: molybdenum, tantalum and lead foil examples

An example of the predicted number of molybdenum, tantalum and lead XRF photons reaching different positions of the detector plane using my XRF model is given in figures 3.5a, 3.5b and 3.5c, respectively. The input parameters used for these examples were chosen to be similar to those used in the preliminary experimental work (chapter 4): an x-ray tube voltage of 100 kVp, a tube current of 350 μA, an exposure time of 2000 ms, a foil thickness of 130 μm for molybdenum, 110 μm for tantalum and 260 μm for lead, additional 1 mm of Al filtration, and a source-to-detector distance of 118 mm. The foil was divided into 128 point sources. The vertical centre of detector plane was divided into 110 μm^2 tiles to match the detector pixel size for all foils. The collimator positions are marked by the dotted lines in the figures. Inside the collimators is the primary beam.

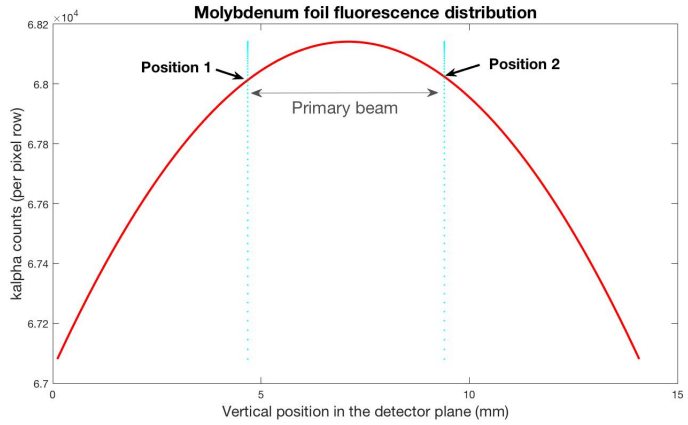

(a)

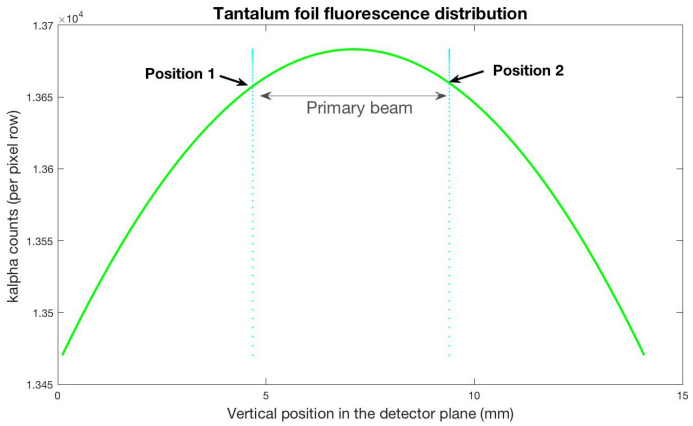

(b)

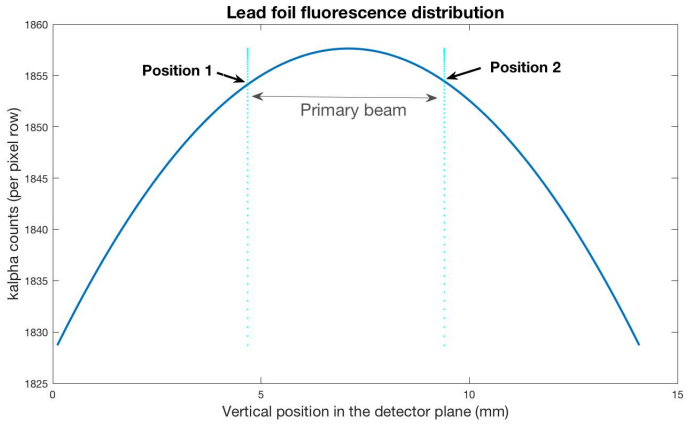

(c)

Figure 3.5: Expected number of (a) molybdenum, (b) tantalum and (c) lead XRF photons across the vertical centre of the detector plane for given model parameters. The dotted lines represent the horizontal (left and right) collimators. In between the collimators the primary beam is not blocked.

3.3.1 Optimal detector position for detecting oblique XRF

The model developed in this thesis is able to provide the optimal camera position, out of the main beam, for detecting XRF. From the XRF distribution plots the two positions that provide maximum fluorescence with minimal primary beam contamination are obtained. These positions are marked as position 1 and position 2 on the plots in figures 3.5a, 3.5b and 3.5c. When the collimators positions are changed (easy to do in my model), the size of the main beam changes, and the optimal detector positions change too. Table 3.1 shows the positions 1 and 2 for a molybdenum foil with changing collimator positions (same exposure parameters as above).

Collimator settings (mm)	Position 1 in DP (mm)	Position 2 in DP (mm)
Top collimator = 1 Bottom collimators = 1 Left collimator = 1 Right collimator = 1	4.7	9.4
Top collimator = 1 Bottom collimators = 2 Left collimator = 1 Right collimator = 2	4.7	11.8
Top collimator = 2 Bottom collimators = 2 Left collimator = 2 Right collimator = 2	2.3	11.8

Table 3.1: This table shows the effect of wide or narrow collimator positions on the optimal position for detecting XRF, outside of the main beam, for a molybdenum foil. Position 1 and 2 are vertical positions in the detector plane.

3.4 Optimal foil thickness

The optimal thickness for a foil is directly related to the foil element that the x-rays are passing through. It can be derived from the Beer-lambert law that, the denser the foil element, the thicker it should be. I investigated the foil thickness that enables maximum fluorescence to escape a foil in Vanden Broeke [2015]. This research developed an equation for the number of K_α photons escaping a foil of thickness L. This equation has been discussed in section 3.2.3 of this thesis.

A plot showing the optimal thickness for molybdenum, indium, and tantalum foils for a polychromatic input spectrum, retrieved from Vanden Broeke [2015], is shown in figure 3.6. The steepness of the peaks gives a measure of how much tolerance there is on the foil's thickness, i.e., if the maximum is a sharp narrow peak then a small change in thickness will cause a large change in fluorescence output, and on the other hand if the peak is broad then a difference in foil thickness may have little effect on the transmitted fluorescence. Table 3.2 shows the optimum foil thickness of several suitable foil materials, including their 90 % tolerance values (Opt90). By suitable I mean not chemically reactive and available in a foil form.

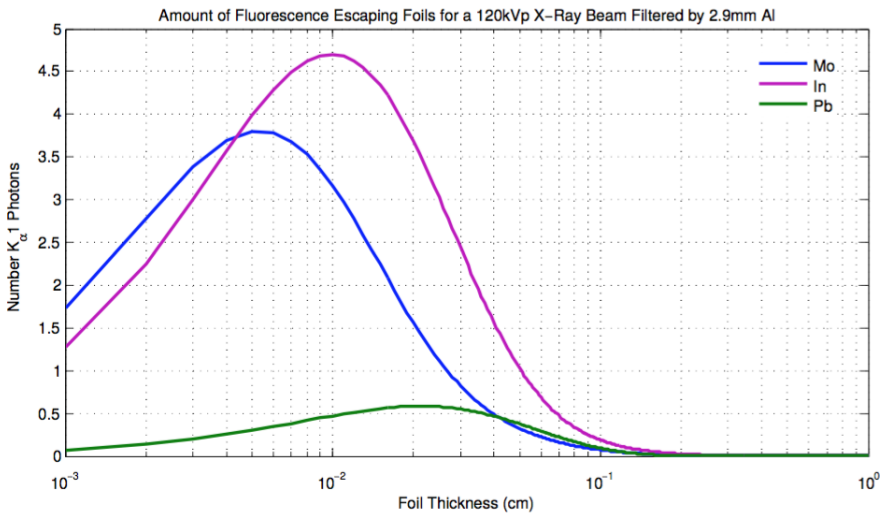

Figure 3.6: Optimum foil thickness for polychromatic input beam. Note that the x-ray spectrum has been normalised. The lead foil has more tolerance than the molybdenum and tantalum foils. Image retrieved from Vanden Broeke [2015].

Element	Optimal thickness (μm)	Opt90 (μm)
iron	44	25 - 78
copper	44	26 - 74
molybdenum	55	32 - 88
zirconium	82	48 - 133
silver	63	37-101
indium	99	58 - 159
tin	104	61 - 168
antimony	119	70 - 191
lutetium	169	102 - 265
tantalum	109	66-170
tungsten	98	59 - 152
platinum	99	60 - 155
gold	113	68 - 176
lead	211	127 - 328

Table 3.2: This table shows the optimal thicknesses for several suitable foils. By suitable I mean not reactive and available as a foil. Opt90 demonstrates the thickness at which the XRF signal is not less than 10 % of the optimal signal when using an optimal thickness.

3.5 XRF model validation

The model developed in this chapter is used to produce the distribution of XRF photons in the detector plane, considering various scanner parameters. This section describes the effect that relevant parameters have on detecting the XRF signal. This validates the model as it offers a comparison between the model's output and the physics of the system.

3.5.1 Exposure settings

In this section I explain the fundamental physics principles behind increasing the tube voltage, tube current and exposure time. The fluorescence model is validated using these principles. It is important to note that for the parameters

listed below, only one parameter was changed at a time. This allows me to investigate how changes to that parameter affect the XRF distribution and XRF intensity.

Tube voltage

The kVp (tube voltage) determines the potential difference between the cathode and the anode of the x-ray tube. The greater the potential difference, the faster the electrons travel from the cathode to the anode. Therefore, a higher kVp results in an increase in; (1) the number of photons generated; (2) their mean energy; and (3) their maximal energy. An increased number of photons generated means an increased number of photons available for XRF creation (equation 3.2). A higher tube voltage also increases the likelihood of XRF production in high-Z materials. The model developed in this chapter ~~validates~~ also demonstrates that a higher tube voltage increases the number of XRF photons in the detector plane, as shown in figure 3.7.

The red colour bars in figure 3.7 represent the changing tube voltage. While the tube voltage is changing from 60 kVp to 120 kVp, the remaining exposure parameters are maximum, i.e., exposure time = 4 sec and tube current is 350 μA.

Exposure time

The exposure time determines the number of photons that are generated. Therefore, changing the time simply controls the quantity of the exposure. An increased exposure time increases the number of photons available to produce XRF. The XRF model validates this in figure 3.7.

The yellow colour bars in figure 3.7 represent the changing exposure time. While the exposure time is changing from 1 sec to 4 sec, the remaining exposure parameters are maximum, i.e., tube voltage = 120 kVp and tube current is 350 μA.

Tube current

Increasing the tube current increases the power applied to the x-ray tube. This heats up the filament inside the x-ray tube and releases more electrons that collide with the target anode to produce more radiation. A linear relationship exists between the tube current and the radiation output. Therefore, increasing the tube current increases the number of photons available to produce XRF (similarly to the exposure time). The XRF model validates this in figure 3.7.

The blue colour bars in figure 3.7 represent the changing tube current. While the tube current is changing from 100 μA to 350 μA, the remaining exposure parameters are maximum, i.e., tube voltage = 120 kVp and exposure time is 4 sec.

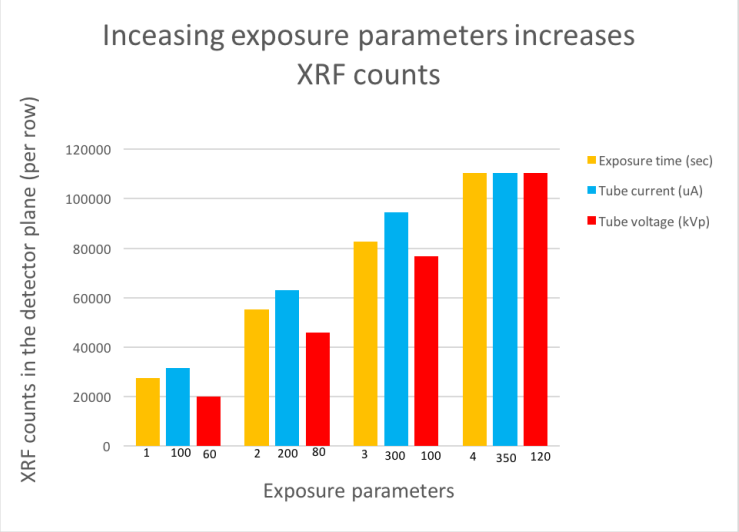

Figure 3.7: This figure demonstrates that increasing the exposure parameters increases the XRF counts (strength of the XRF signal). The increase is also quantified.

3.5.2 Filtration

An x-ray beam consists of a spectrum of x-ray photons of different energies. Inside the MARS scanner there is 1.8 mm of inherent aluminium-equivalent filtration. This filtration removes many of the lower energy photons. The effect of added filtration on the incoming spectrum (obtained from SpekCalc) is shown in 3.8.

Figure 3.9 compares different thicknesses of aluminium and copper filtration. Note that these figures assume that no foil is present.

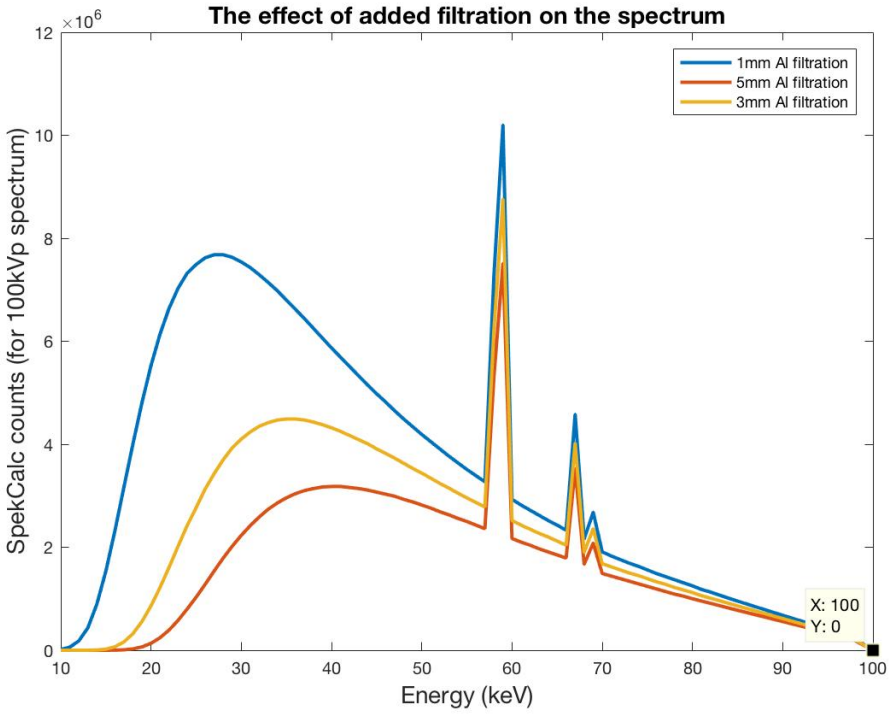

Figure 3.8: This figure shows the effect of added filtration on the x-ray source spectrum. The number of photon counts is reduced with increased aluminium filtration.

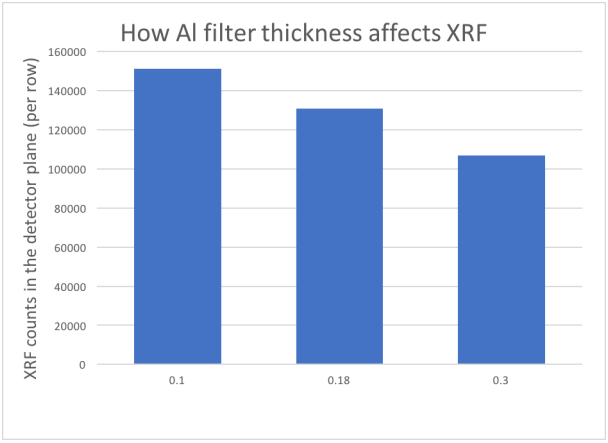

(a)

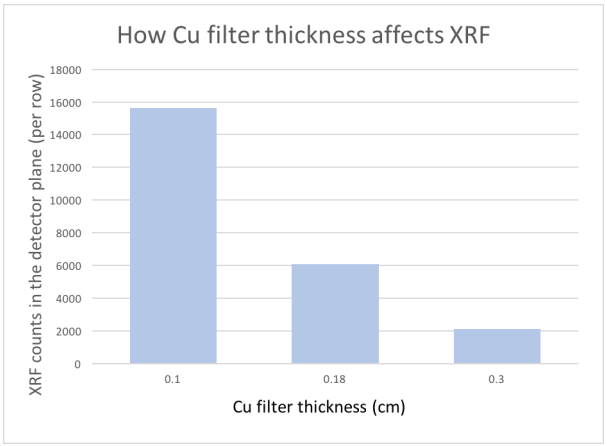

(b)

Figure 3.9: The effect of added filtration on the number of XRF which reach the detector plane. In (a) the total filtration is 1.8 mm of inherent aluminium-like filtration plus extra added aluminium filtration, while in (b) the total filtration is 1.8 mm of inherent aluminium-like filtration plus extra added copper filtration. The effect of the filtration is also quantified.

3.5.3 Collimation

A collimator is a metallic barrier that is used to reduce the size of the x-ray beam. The collimators should be thick enough to block the primary beam from the source. Narrow collimators decrease XRF, while wide collimators increase XRF. However, wide collimators give a larger area of primary beam contamination. The model validates these hypotheses and the effect of the collimators are shown

in more detail earlier in this chapter (section 3.3.1).

3.5.4 Source-to-detector distance

The source-to-detector distance (SDD) is given by the source-to-foil distance (SFD) plus the foil-to-detector distance (FDD), i.e., $SDD = SFD + FDD$. Inside the MARS small bore scanner, the SFD is fixed and the FDD is the only parameter that can be adjusted to change the SDD. A schematic of this is shown in figure 3.10. Decreasing the FDD gives a higher number of fluorescence counts, as expected (because the solid angle from the foil to the detector is increased). Figure 3.11 shows model results for different FDD's for a molybdenum foil with a x-ray tube voltage of $100\,kVp$, a tube current of $350\,\mu$A, an exposure time of $2000\,ms$, and a foil thickness of $130\,\mu$m. The foil was divided into 128 point sources. The vertical centre of detector plane was divided into $110\,\mu m^2$ tiles to match the detector pixel size for all foils.

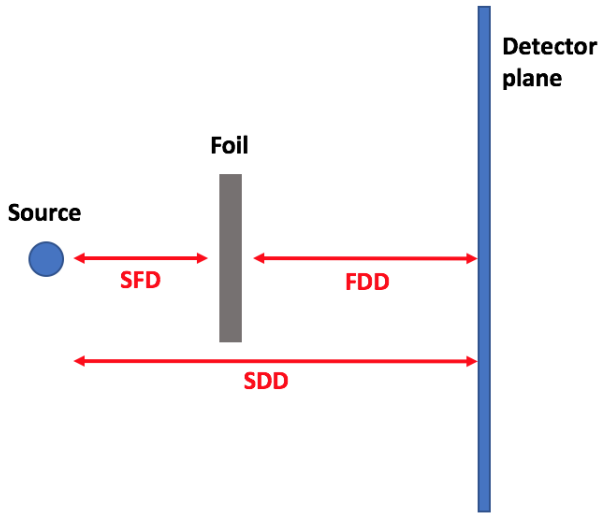

Figure 3.10: This figure shows that the the foil-to-detector distance (FDD) can be manipulated to change the source-to-detector distance (SDD). The source-to-foil distance (SFD) is fixed and is stipulated in the x-ray tube's specifications. Inside the MARS small-bore scanners SFD is said to be 55 mm.

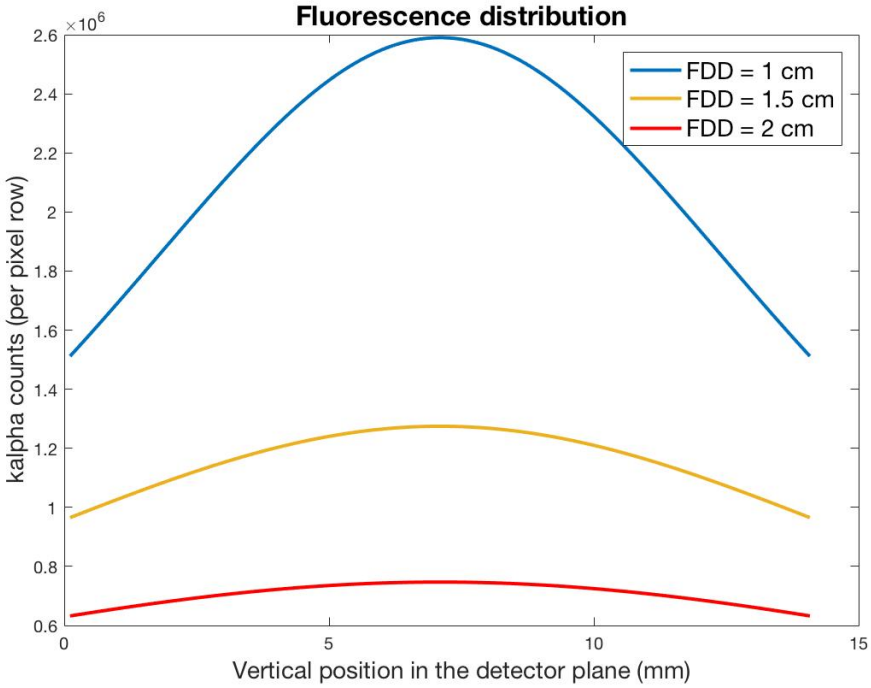

Figure 3.11: Fluorescence distribution for different foil to detector distances (FDD's) for a molybdenum foil with a x-ray tube voltage of 100 kVp, a tube current of 350 μA, an exposure time of 2000 ms, and a foil thickness of 130 μm.

3.6 Discussion

In this chapter an analytical model that quantifies XRF production and detection in MARS was developed. The model breaks down aspects of the physical system and is used to determine the optimal settings for many user-defined scanner parameters. The model accounts for various physical processes including XRF production and solid angle projections. The effect of the scanner parameters on XRF production and detection is visualised through the output of my model.

Each foil material has an optimum thickness that allows maximum XRF to escape the back of the foil to make it to the detector. The optimal thickness (for a polychromatic input beam of 100 kVp) for the molybdenum, tantalum and lead foils are 50 μm, 100 μm and 210 μm, respectively.

The XRF counts in the detector plane increase for each of the exposure parameters (tube voltage, tube current, exposure time). The rate of increase is different for each parameter but the same trend is observed for each, i.e., an increase in exposure parameters increases XRF production. The SDD is given by the SFD plus the FDD. The model has shown that the FDD has the most effect on the strength of the XRF signal. A decrease of 0.5 cm in FDD increases the XRF signal (at the (0,0) position in the detector plane) by approximately 2%. This means that a variation of 2 cm, which could easily happen because of inaccurate specifications, causes nearly a 10% reduction in XRF counts in the detector plane. A summary of the optimal scanner parameters are shown in table 3.3.

Tube voltage	Tube current	Exposure time	FDD
maximum	maximum	maximum	minimum

Table 3.3: Optimal MARS scanner parameters for detecting a maximum XRF signal in the detector plane. In a MARS scanner, these parameters are limited due to software and hardware restrictions, i.e., the maximum tube voltage is 120 kVp, the maximum tube current is 350 μA, the maximum exposure time is 4s, and the minimum FDD is 1.18 mm.

Added filtration decreases the XRF counts in the detector plane. However, low-Z filters (such as aluminium and copper) help reduce primary beam contamination by filtering out low-energy photons. The optimum amount of filtration depends on the foil material that is used. A similar method to finding the optimal foil thickness [Vanden Broeke, 2015] can be used to find an optimal filter thickness. Filter thickness is a parameter that I aim to optimise in the future.

The collimators affect the range of XRF detected by the Medipix3RX detector. Narrow collimator settings reduce the XRF range and the number of XRF photons reaching the detector plane. Therefore, wider collimator settings are optimal.

The model's trends have been validated with the underlying physics. However, the model developed in this chapter makes a few assumptions that could cause

discrepancies between model and experimental outputs. The model does not take into account scatter. Scatter is likely to come from the collimators (lead) and the gantry (lead). In a transmission setup scatter may be significant and narrow collimation should give rise to increased scatter in the field of view Butler et al. [2015]. The modelled XRF distribution only represents the K_α photon contributions, whereas in addition there will also be K_β fluorescence present.

The detection efficiencies of the different sensor materials have not been accounted for in my XRF model. The thickness, atomic number and density of the sensor determine the quantum detection efficiency. This is planned to be incorporated into the model in the future.

With the model I developed, any of the input parameters can be changed and the output XRF distribution can be easily seen. This enables me to determine exactly how each MARS scanner parameter affects the XRF, without having to do time consuming experimental tests. This is very useful for the eventual automation of the energy calibration technique using foils.

The next chapter of this thesis uses the model's results to experimentally detect XRF in MARS. The work presented in this chapter is significant in three ways: (1) it allowed me to understand the physics principles behind every step of XRF creation and detection; (2) it is able to determine optimal scanner and geometric parameters, preventing time consuming experiments; and (3) the model can be used to model extremities without risk of damaging the equipment, in particular the detectors.

The model developed in this chapter is based upon the fundamental principles behind XRF creation and detection. This chapter has presented novel concepts which have been used to develop customised solutions for detecting XRF in the MARS scanner. More detail about experimentally detecting XRF is given in the following chapter (chapter 4). This chapter aligns with the MARS team goal by improving the spectral performance of the MARS scanner.

3.7 Summary

- Calibrating the energy response of the Medipix3RX detector is achieved by detecting monochromatic XRF photons.
- An accurate energy calibration reduces blurring in the energy domain and results in a better image reconstruction and an improved image.
- An analytical model is developed to simulate XRF from the point of creation, to the point of detection (in the DP plane).
- The model is based on fundamental physics principles and accounts for: (1) the primary beam emission from the source; (2) the XRF creation and emission from the foil; and (3) the XRF detection by the Medipix3RX detector.
- The dual tetrahedron method is used to specify solid angle calculations in the model. There are two solid angle contributions. The first solid angle contribution is from the source to the foil, and the second from the foil to the detector.
- XRF production inside the foil is based on a model that I created in my Masters thesis [Vanden Broeke, 2015]. That model optimises the thickness of the foils to ensure that maximum XRF is escaping the foil.
- The XRF distribution plots for the molybdenum, tantalum and lead foils give two positions, out of the main beam, where XRF is maximum. These positions mostly eliminate contamination from the primary x-ray beam.
- The optimal thicknesses for a range of suitable foils are provided. The optimal thickness range where the XRF signal has not been reduced by more than 10% is also given.
- The analytical XRF model is validated by examining how it behaves with a change in experimental parameters.

Chapter 4

Detecting X-ray Fluorescence in MARS

In this chapter I develop a methodology to detect x-ray fluorescence (XRF) in a MARS scanner using an oblique transmission setup. XRF is used to characterise the energy response of a multi-element camera in MARS by providing a per pixel energy calibration. The XRF setup is derived from the model output in chapter 3. Due to the low emission and detection efficiency of the XRF signal in a transmission setup it is challenging to measure a well-defined XRF peak. In the proposed approach, metallic foils are positioned on the front of the extrinsic filtration that is located between the x-ray source and the source collimators. The primary x-ray beam is narrowed with the collimators and oblique XRF reaches the detector plane outside of the primary beam. As a result, there is minimal contamination by the polychromatic x-rays from the primary beam. Characterising the (per-pixel) energy response improves the quality of the 2D spectroscopic data set obtained with the MARS scanners, making the material analysis more accurate, which in turn makes the images more medically useful.

This chapter presents aspects of my work towards developing this methodology. The motivation for this chapter is discussed in section 4.2, while XRF creation in MARS is explained in section 4.3. The significance of a transmission setup is outlined and an oblique transmission setup is the introduced in section 4.3.2. The

significance of various experimental parameters that control XRF in MARS are discussed in section 4.4. Optimal parameters for detecting a well-defined XRF signal are discussed and experimental results for a 3-detector-element camera for molybdenum, tantalum and lead foils are presented in section 4.5. Lastly, section 4.6 shows an analysis of the results and discusses where improvements can be made.

I was the principal investigator for this work but I would like to acknowledge Dr Ali Atharifard (MBI employee) for his contributions. This work resulted in one publication where I am the primary author, another publication with me as primary author under preparation, and two scientific posters. Dr Atharifard also dedicated one of his thesis chapters to this work [Atharifard, 2017].

4.1 Introduction

Each pixel in the Medipix3RX has dedicated front-end electronics, allowing measurements of deposited energy in each pixel element. Analogue front-end electronics in each pixel provide charge amplification and shaping, while a digital front end allows for operation in charge summing mode (CSM), and in single pixel mode (SPM). In the ASIC are 9-bit (0 - 511) energy threshold DACs (front-end). The energy threshold DACs are global DACs which are converted to an energy threshold value by the system's energy calibration. The same threshold DAC, or energy threshold, values are set for all pixels in the matrix. In the analogue section of each pixel the globally energy threshold is set via a Digital-to-Analog Converter (DAC).

The two discriminators of each pixel contain an independent 5-bit (0 - 31) fine adjustment DAC to correct the inter-pixel threshold dispersion. Threshold equalisation aims to minimise the threshold dispersion, however, it can not be eliminated completely due to the limited range and resolution of the fine adjustment DAC [Ballabriga et al., 2013]. Panta et al. [2015a] explains how a threshold equalisation reduces some of the inter-pixel dispersion. The inter-pixel variation of the energy response is a limiting factor in global spectral resolution and the precision of the

energy calibration [Manuilskiy et al., 2004]. Calibrating the energy response of individual pixels is necessary since the residual threshold dispersion can degrade the contrast and spectral resolution [Manuilskiy et al., 2004].

The current energy calibration used inside the MARS scanners is based on the global energy calibration technique developed by Panta et al. [2015b]. This technique is practical, fast, and easy to implement. However, this method is not pixel specific, resulting in different effective threshold DACs for each pixel.

4.2 Per-pixel energy calibration

This section defines the motivation of the chapter and explains why a per-pixel energy calibration is advantageous. Imperfections in the sensor crystal cause a variation in the charge collection efficiency across the detector matrix [Panta et al., 2015a]. Additionally, there are also existing uncertainties in the electronics parameters. Therefore, an analogue pulse in the front-end electronics is processed slightly differently for each of the pixels of the detector matrix. Therefore, when the analogue signal is converted to a digital signal, the pulse height of the incident photon will also be slightly different for each of the pixels in the detector matrix.

Significant spatial and spectral non-uniformity across the detector array is also caused by inter-pixel variations and threshold dispersion [Atharifard et al., 2017]. To explore the full spectroscopic capability of the MARS imaging system, energy calibration and optimisation of the detectors need to be performed at a pixel level. Figure 4.1 demonstrates two pixels responding differently to the same energy threshold. The difference in energy response between the pixels is partly caused by threshold dispersion [Pelgrom et al., 1989].

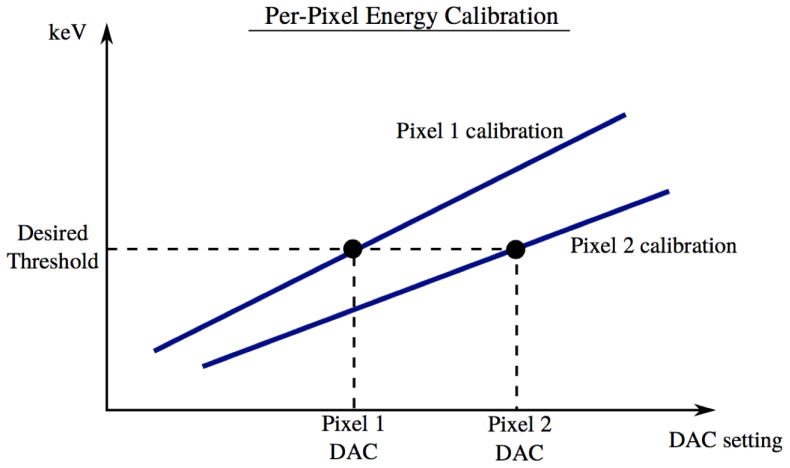

Figure 4.1: Plot showing how the DAC step chosen for each pixel is related to the keV in a per-pixel energy calibration. The global energy calibration procedure does not take into account that every pixel has a different energy response to the globally set threshold DAC. Image retrieved from Vanden Broeke [2015].

The XRF method developed in this chapter is able to perform a per-pixel energy calibration. XRF sources are useful for calibrating energy-resolving photon-processing detectors due to their monochromatic nature. The XRF signal is material specific and used as a physical reference so it is independent of instabilities in the source. The per-pixel XRF technique does not aim to replace the kVp method, but rather it will be used to validate the reliability of the kVp method. The XRF method developed in this chapter is feasible in the current MARS setup. The metallic foils are placed on a movable filter-bar, thus the process can be easily automated.

4.3 XRF creation in MARS

XRF is created in MARS by illuminating metallic foils with the x-ray source. Figure 4.2 demonstrates how a target foil changes the polychromatic source spectrum to a near monochromatic XRF spectrum. Inside the MARS scanner the source and detector are directly in front of each other, with the filter-bar just behind the source. The detector is able to be moved up or down but the source and filter-bar are fixed. A reflection setup is not feasible inside the MARS scanner,

therefore, a transmission setup is used.

The XRF is contaminated by polychromatic x-rays from the x-ray source that are used to induce excitation in the foil (the contamination is not shown in diagram). XRF has a low emission and detection efficiency, therefore it is challenging to measure a well-defined XRF peak and minimising contamination is essential.

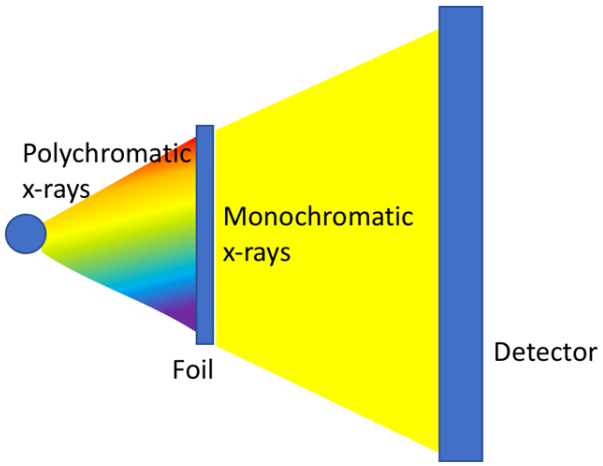

Figure 4.2: This plot demonstrates how a foil creates a nearly monochromatic XRF source from a polychromatic x-ray source beam.

4.3.1 Reflection versus transmission geometry

Common techniques for minimising the polychromatic contamination in XRF setups include having the foil illuminated by an x-ray beam that is not directed towards the detector ("reflection" setup), and/or by placing a lead shield containing a pin hole between the detector and the foil [Bruyndonckx et al., 2011; Butler et al., 2015; Uher et al., 2012]. In the reflection setup the target is placed at an angle to the centre axis and the detector is placed at an angle off the emitter axis.

An example of a reflection setup is shown in figure 4.3a. Measurements from such setups suffer from less Compton scattering contamination than transmission setups. However, this setup is not feasible inside the MARS scanner as the source and detector are fixed linearly (i.e., the source and detector in MARS are fixed

in front of each other). To create XRF in the MARS setup, the target is placed in between the two modules ("transmission" geometry). Butler et al. [2015] compares the two setups and reports that the fluorescence peaks corresponding to the characteristic lines have a lower intensity when the transmission geometry is used. However, Butler et al. [2015] has shown that it is possible to construct transmission type setups which produce strong fluorescence signals despite the increase in scatter. In other transmission setups, such as in [Tran et al., 2004], the Compton scatter contribution is deemed to be negligible.

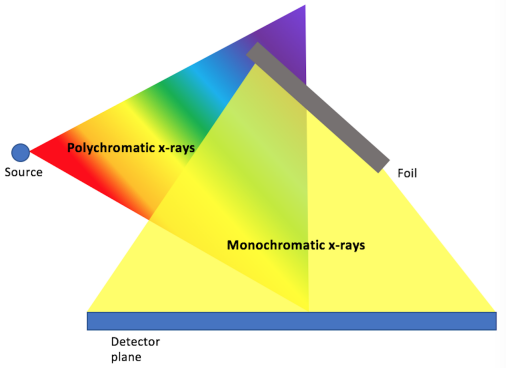

(a)

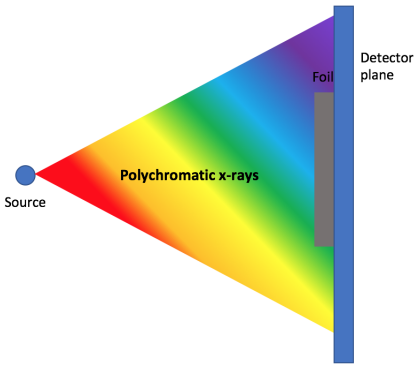

(b)

Figure 4.3: (a) In reflection geometry the detector is placed at an angle to the source. The collimators are used to narrow the main beam and avoid contamination. (b) In Panta's transmission setup a metallic foil is taped to the front of the detector and XRF is measured inside the main beam.

4.3.2 Oblique transmission setup

Panta et al. [2015b] investigated a transmission geometry to detect XRF in the MARS scanner. He measured XRF from different metallic foils that were manually fixed onto the detector. The experimental setup he used is shown in figure 4.3b. Measurements of different metallic foils were made to provide several calibration points. Although this technique managed to measure XRF, it had some drawbacks: (1) the XRF measurements were made in the presence of the primary beam, therefore there was primary beam contamination; (2) the exposure settings were low to avoid saturating the detector, therefore the exposure time was high and measurements took a long time; (3) the technique can not be automated as it involves manual placement of the foils; and (4) currently a per-pixel energy calibration is not available using Panta's method.

The approach proposed in this chapter addresses Panta's limitations by positioning the target on the front of the extrinsic filtration that is located between the x-ray source and the source collimators. When the main x-ray beam is narrowed with the collimators, wide angle (oblique) XRF reaches the detector plane outside of the main beam. This is shown schematically in figure 4.4. As a result, this technique enables the monochromatic XRF beam produced from the metallic foil to be used for the energy calibration of the scanner's detector with minimal contamination by the polychromatic x-rays from the main beam. This technique can be extended to be used for calibrating individual detector pixels. In addition, as the metallic foils can be permanently mounted inside the MARS scanner, it provides a highly automatable method for generating monochromatic photons that can be used for energy calibration. The physics behind XRF production is discussed in detail in chapter 3.

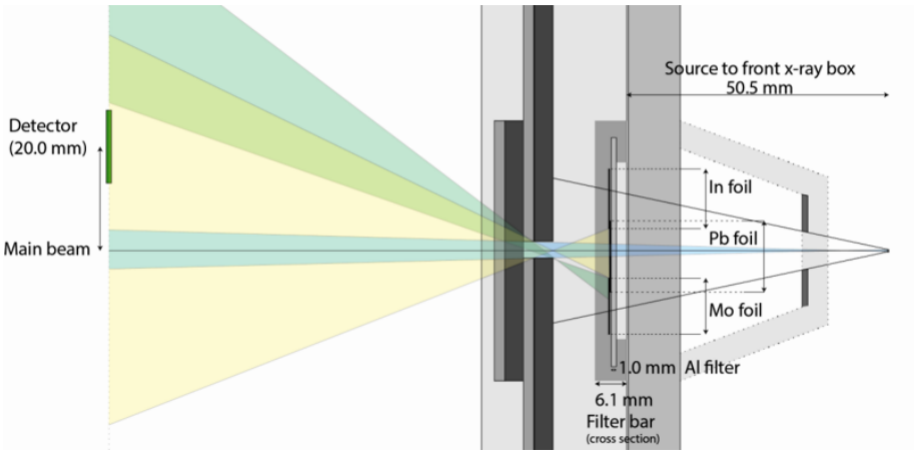

Figure 4.4: Setup for identifying isolated region of lead XRF at the detector plane. The vertical and horizontal collimators are positioned to block fluorescence generated by the other foils attached to the filter-bar. The desired region of isolated lead XRF (yellow) sits between the main x-ray beam and wide angle XRF generated from the other foils (green).

4.4 Factors controlling XRF in MARS

Oblique XRF produced from foils on the filter-bar, in a transmission setup, inside a MARS scanner has been previously investigated by Atharifard et al. [2017]. He demonstrated that a well-defined XRF signal is difficult to detect in the MARS setup. XRF production and detection is controlled by many parameters inside the MARS small bore scanner. In order to detect a well-defined (oblique) XRF signal in a transmission setup, optimisation of the scanner parameters is essential. The XRF model in chapter 3 is used to optimise the scanner parameters. This section is going to discuss some of the experimental parameters and their limitations in current versions of the MARS small bore scanners. Some experimental results are shown to support these claims. The factors presented in this section will be discussed in more detail in the discussion section of this chapter.

4.4.1 Filter-bar design

The MARS small bore scanner has a movable extrinsic filtration module that is located between the x-ray source and source collimators. This module enables different types of source filtration to be selected and used as shown in figure 4.5.

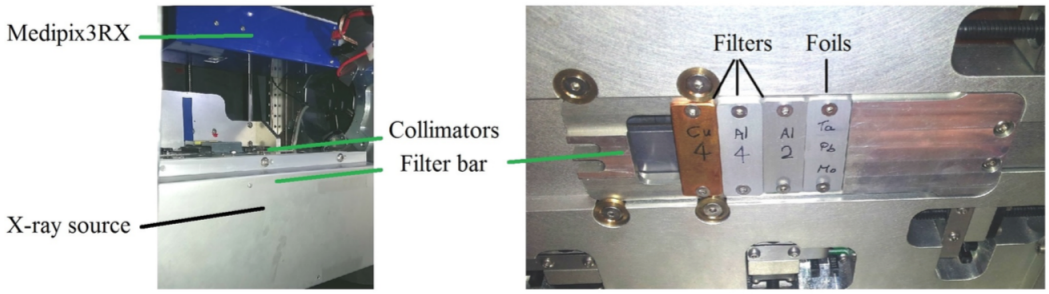

Figure 4.5: Illustration of the transmission setup in the MARS scanner for the XRF measurements. The filter-bar is mounted between the x-ray source tube and the collimators. Control motors are programmed to allow selection of individual foils. Image retrieved from Atharifard [2017].

In the setup presented in this chapter several different metallic foils are placed on the front of the 1 mm aluminium filter-bar in 3×1 and 3×2 arrangements, as shown in figures 4.6 and 4.7, respectively. The foils produce XRF at different energies within the desired imaging range of $10 - 120$ keV, as shown in table 4.1. Foil materials that have been chosen to be positioned on the filter-bar include molybdenum, lead, tantalum, indium, neodymium, and dysprosium. When the foil is illuminated by the x-ray source, each foil will generate XRF, assuming photons of sufficient energy are present in the incident x-ray beam for the given foil (i.e. the K-edge energy). The source collimators are used to isolate the XRF produced by a single foil. The narrowing of the collimators also reduces the size of the main x-ray beam in the detector plane. The MARS camera can then be moved vertically into a position that is both outside of the main beam, and where sufficient XRF is present (optimal DP positions from chapter 3).

Element	Mo	In	Nd	Dy	Ta	Pb
K-edge Energy (keV)	20.0	27.9	43.6	53.8	67.4	88
K_α Energy (keV)	17.5	24.2	37.4	46.0	57.5	75.0
K_β Energy (keV)	19.6	27.3	42.3	52.2	65.2	85.0

Table 4.1: Theoretical K_α and K_β fluorescence and K-edge absorption energies for selected foil materials used in the experimental setup [Bambynek et al., 1972; Hubbell, 2004]. These elements were chosen to provide a spread of XRF energies spanning our desired imaging range. The K-edge energy indicates the minimum incident photon energy required to produce K_α XRF from the given element.

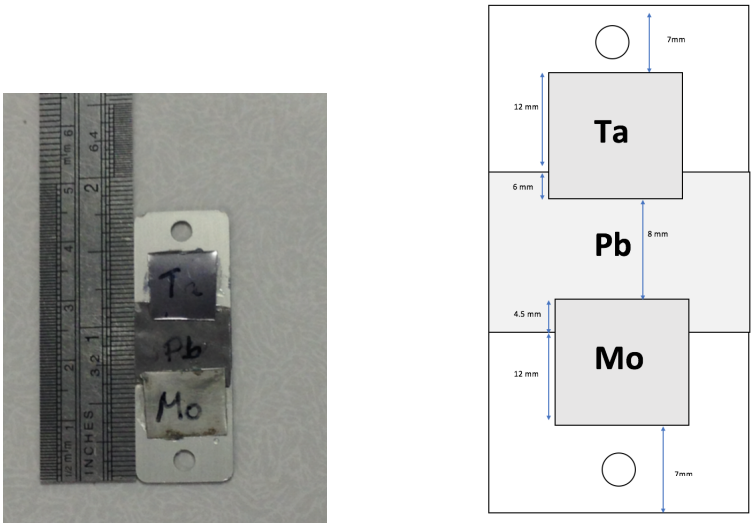

(a) (b)

Figure 4.6: (a) Photo and (b) geometric representation of the 3-foil filter-bar containing molybdenum, lead and tantalum foils.

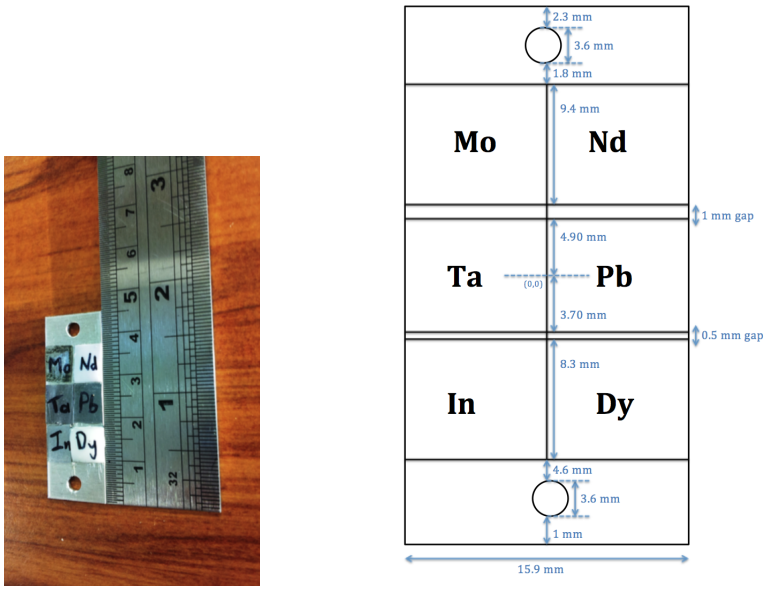

(a) (b)

Figure 4.7: (a) Photo and (b) geometric representation of the 6-foil filter-bar containing molybdenum, neodymium, tantalum, lead, indium and dysprosium foils.

4.4.2 Optimal foil thickness

The foils in the XRF experiments are not of optimal thickness (chapter 3). Table 4.2 compares the optimal and experimental thicknesses of molybdenum, tantalum and lead foils. From figure 3.6, the 90 % tolerance value for the molybdenum, tantalum, and lead foils are also added. More detail on the 90 % tolerance values is found in section 3.4.

Foil	Optimal thickness (μm)	Experimental thickness (μm)	90 % tolerance thickness (μm)
molybdenum	50	130	32 - 88
tantalum	100	110	66 - 170
lead	210	260	127 - 328

Table 4.2: The experimental foil thicknesses are the foil thicknesses used for the results in this chapter. The optimal thicknesses and their 90 % tolerances are obtained from Vanden Broeke [2015].

4.4.3 Collimation

A collimator is a metallic barrier that is used to reduce the size and shape of the x-ray beam. The width of the collimators affects the fluorescence range. In figure 4.8a (thin collimators) the XRF has a larger range on the detector plane than in figure 4.8b (thick collimators). The collimators should be of sufficient thickness to block the main beam, but be thin enough the avoid considerably reducing of the fluorescence range. Currently, the collimator thickness in MARS scanners is 3.6 *mm*. Collimator thickness will be discussed with the MARS scanner design team and a redesign of the scanner collimators may be done.

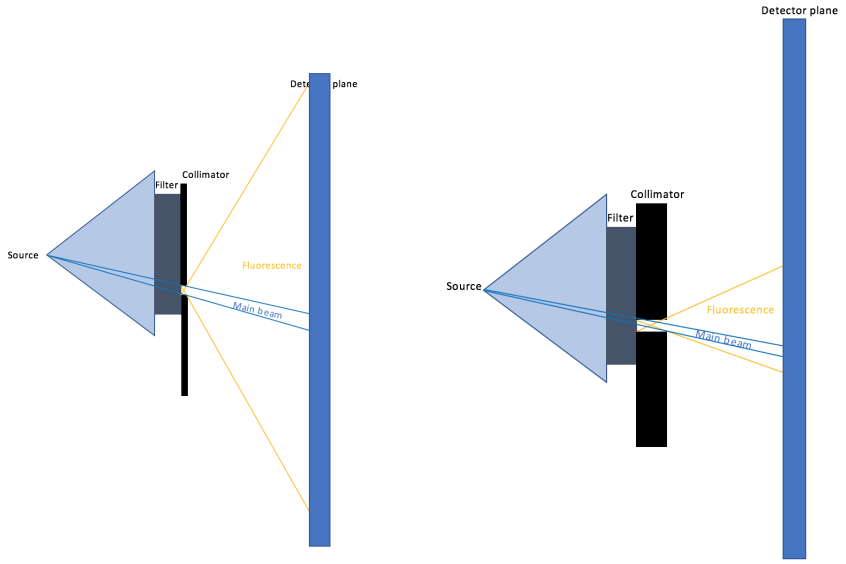

(a) (b)

Figure 4.8: The thin collimators in (a) give a wide XRF range, whereas the thick collimators gives a narrow XRF range. Note that the effect is exaggerated.

4.4.4 Source-to-detector distance

A shorter SDD produces a stronger, more well-defined XRF signal (chapter 3). The most relevant contribution to the SDD is from the FDD (foil-to-detector distance). It is advantageous to have the FDD as small as possible to increase the strength of the XRF signal. The MARS scanner has inherent restrictions to this through an anti-collision software. The anti-collision software prevents the

different modules in the scanner from moving too close to each other and colliding (e.g., the x-rays source and the detector). Figure 4.9 shows experimental results for changing the FDD in a MARS scanner. There is no discernible fluorescence fluorescence signal when the Mo foil is behind the collimator.

Figure 4.9 proves that the shorter the FDD, the stronger and more defined the XRF signal. This plot was obtained using MARS-4 which has a GaAs sensor bump bonded to a Medipix3RX readout. The results are obtained using a molybdenum foil and the XRF data was collected inside the main beam (not oblique). The Mo foil was hammered down to be 50 μm thick, the tube current was 20 μA, tube voltage was 50 kVp and an exposure time of 4 s was used. The x-rays incident on the foil went through 7.25 mm of prior aluminium filtration. The reason for this is to remove low energy photons so that the XRF peak is clearly visible.

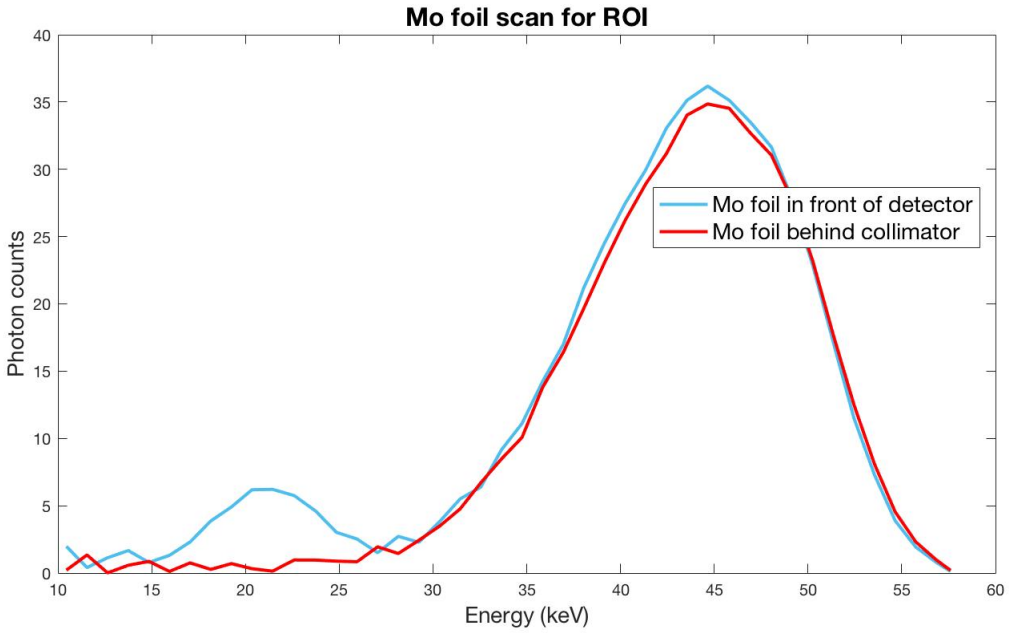

Figure 4.9: Mo foil scan for a region of interest (ROI)- 50 pixels- where the foil is in front of the detector, and where the foil is behind the collimators. This figure demonstrates that a shorter foil-to-detector distance (FDD) produces a more defined XRF signal (blue line). I used 5.45 mm of added Al filtration.

These results do not demonstrate oblique XRF, however, it convincingly demonstrates that a shorter FDD produced a more defined XRF signal. This is the case regardless of whether an oblique setup is used. MARS-4 does not have the same restrictions as the later version of the MARS scanner used for the remaining experiments. However, the results of this study prompted me in selecting the motor testing interface script in MARS debug mode on the MARS graphical user interface (GUI). This script allows me to override the anti-collision software and bring the foil and detector close together to minimise the FDD.

4.4.5 Three-detector-element camera

Multi-detector-element cameras are installed in the MARS small-bore scanners to image larger objects faster. The detector arrangement depends on the DICOM tags given to the data by the MARS software. Private tags that give the x and y positions of each detector element, relative to each other. Figure 4.10 shows the geometry of the 3-detector-element camera in MARS-15. The associated 3-detector-element image is shown in figure 4.11. This figure is for a single exposure and demonstrates the shadows that are present due to the staircase layout of the 3 detector elements. A single detector element is also called a chip. The bottom chip is the chip that is closest to the main beam, the middle chip is the second closest to the main beam, and the top chip is furtherest away from the main beam.

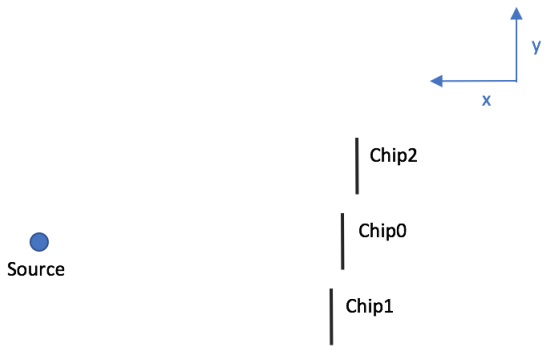

Figure 4.10: The chip geometric positions were obtained from the image DICOM tags and were found to be Chip0(x,y) = 0, 2.505; Chip1(x,y) = 3.5, -11.96; Chip2(x,y) = -3.5, 16.915. The chips have a staircase structure. From now on Chip1 will be referred to as the bottom chip, Chip0 the middle chip, and Chip2 as the top chip.

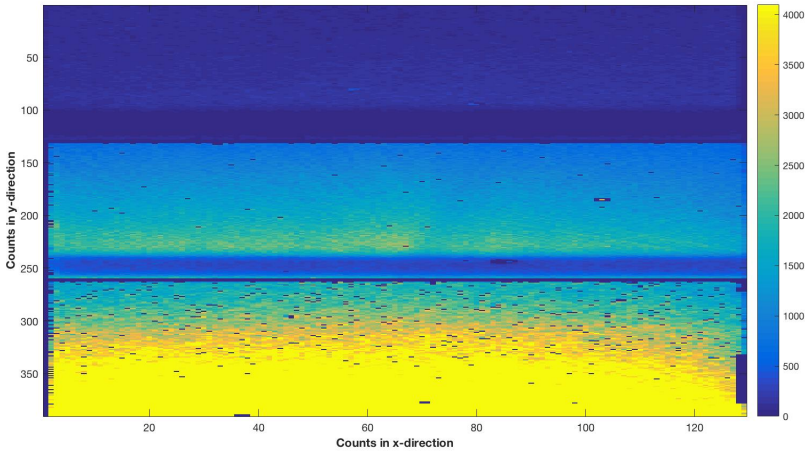

Figure 4.11: There are shadows at the bottom of the middle and the bottom of the top chip. These regions are not included in the ROI's for the XRF plots below. The bottom chip is closest to the main beam and therefore it is at most risk of being saturated, therefore results from this chip should be disregarded.

4.4.6 Filtration

The MARS scanner has 1.8 mm of aluminium equivalent filtration inside the x-ray tube. The foils on the filter-bar have an additional 1 mm of aluminium which is used to hold the foils in place. The foils are positioned in such a way that the source photons pass through the foil to create XRF, and then the XRF has to pass through the 1 mm of aluminium.

Figure 4.12 demonstrates how having the foil taped to the collimator, instead of on the filter-bar, changes the XRF signal for the middle detector chip in MARS-15. The distance from the surface of the filter-bar to the surface of the vertical collimator is 10.9 mm. The distance from the surface of the filter-bar to the surface of the horizontal collimator is 14.2 mm. The FDD is the same when the foil is on the collimator and when it is taped to the collimators.

Similar results are obtained for the top and bottom chips. Note that the exposure parameters are exactly the same for both cases. The only difference is the foil position. Having the foil on the filter-bar versus behind the collimators has a negligible effect on the FDD. The distance between the surface of the filter-bar and the surface of the horizontal collimator is 14.2 mm, and the difference between the surface of the filter-bar and the surface of the vertical collimator is 10.9 mm.

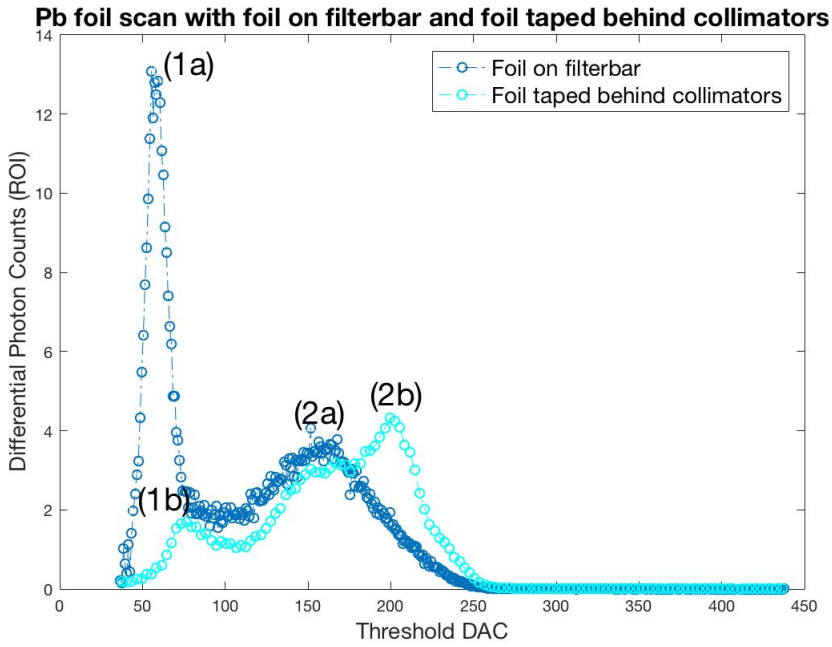

Figure 4.12: These results show the XRF signal for the middle chip of a 3-chip camera when a lead foil is illuminated.. The figure compares the XRF signal when the foil is on the filter-bar and when the foil is taped behind the collimators (FDD is constant). The tube current was 180 μA, the tube voltage was 120 kVp, and the exposure time was 500 ms.

The DAC values of each of the peaks in figure 4.12 are converted to energy values using the global energy calibration. These are listed in table 4.3 below. The nature of these peaks are discussed in the discussion section of this chapter.

Peak	Experimental threshold DAC	Experimental K_α (keV)
(1a)	55.5	17.2
(1b)	76.5	25.1
(2a)	162.5	57.4
(2b)	199.5	71.4

Table 4.3: Experimental peaks are converted from threshold DAC to keV using the global energy calibration.

4.5 Results: oblique XRF detection

MARS-15 is used for the experiments presented in this section. The first CSM counter (CSM1) of a CZT-Medipix3RX (2 mm CZT crystal bump bonded to a Medipix3RX) is used for the measurements. The detector was equalised prior to the experiments using the noise floor measurements, and the average energy response of the detector was approximated by the global energy calibration using the kVp method. The energy calibration of the detector was done again to ensure that any instabilities are accounted for. MARS-15 has a motorised filter-bar that allows an automated selected of extrinsic filters, as shown in figure 4.5. The filter-bar used for the results presented below has a 3×1 geometry (figure 4.6a). The collimators enable selection of different types of filters. The filter-bar that is used for the experiments presented in this chapter has a 3×1 geometry and is shown in figure 4.6a. Table 4.1 shows the XRF and K-edge absorption energies for the selected foil materials.

When the foils on the filter-bar are illuminated by the source x-ray beam that has an energy greater than the K-edge energy of the foil material, XRF is generated. The directions in which the XRF photons travel in are limited by the collimators. A schematic representation of the transmission geometry that was used for the oblique XRF measurements is shown in figure 4.4. The three foil filter-bar is used (figure 4.6a) and the filter-bar is approximately 5.4 cm away from the x-ray tube. The x-ray beam and XRF escaping the foils are collimated with two pairs of horizontal, and two pairs of vertical collimators that can move left, right, up and down by user-defined settings selected on the MARS GUI. The MARS camera is also able to move up or down to be inside or outside of the primary beam.

A threshold scan for the Mo, Ta, and Pb foils is done using the dependent acquire script on the MARS scanner software. I use to script to sweep through the thresholds energies for CSM1 (I define a minimum and a maximum threshold), while the other settings are kept constant. The dependent acquire script is developed internally by MARS team members. The experimental parameters that are used for the dependent acquire scans of the molybdenum, tantalum and lead

foils are shown in table 4.4. The optimal camera position is calculated for these parameters using the model developed in chapter 3. This is checked by locating the collimator shadows in a single exposure. The camera is moved in small steps until the collimator shadows are no longer visible. High exposure parameters and a short FDD are used to maximise the XRF generated in the foils. Since the measurements are made outside of the primary beam, the detector is not exposed to a high flux of x-rays. For each foil, a number of measurements are made (iterations) and then averaged at each threshold value. Numerical derivatives are taken within every three threshold steps to obtain the differential spectra.

Experimental parameters	Mo	Ta	Pb
Foil thickness (μm)	130	110	260
Tube voltage (kVp)	100	100	120
Tube current (μA)	350	350	180
Exposure time (s)	2	2	0.5
FDD (cm)	1.18	1.18	1.18
Collimators (mm)	Left: 5 Right: 5 Top: 4 Bottom: 4	Left: 5 Right: 5 Top: 15 Bottom: -12	Left: 15.81 Right: 11.69 Top: 4 Bottom: 15.35
camera translation (mm)	34	53	50
iterations	50	50	50
Step size (DAC)	1	1	3
Filtration (mm)	1mm Al + inherent	1mm Al + inherent	1mm Al + inherent

Table 4.4: Experimental parameters on MARS-15 for detecting XRF from molybdenum, tantalum, and lead foils. The inherent filtration is 1.8 mm Al equivalent.

4.5.1 Chip comparison for three foils

The XRF signal from each foil, for each detector chip is shown in figures 4.13, 4.14, and 4.15. Figures 4.13, 4.14, and 4.15 represent the bottom, middle and top detector chips, respectively. These plots represent the XRF signal in a region of

interest (ROI) that avoids the chip shadows (figure 4.11). A per-pixel representation of the plots are not shown as the results are too noisy and longer acquisition times are needed to provide enough statistics per pixel. A summary of the peak XRF values are shown in table 4.5. The results are discussed in depth in the discussion section of this chapter.

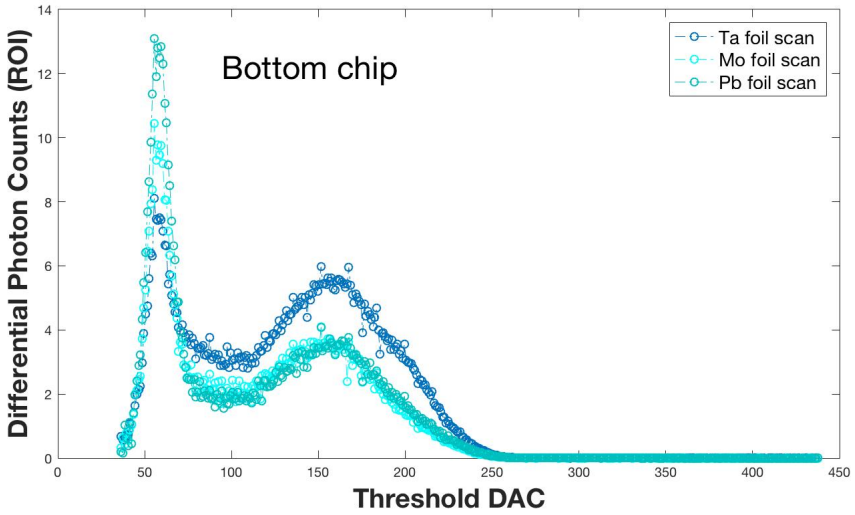

Figure 4.13: The bottom chip is closest to the main beam. This plot shows the XRF signal for Mo, Ta, and Pb foils for the bottom chip in MARS-15. The ROI is defined by px and py, where px marks the x-direction position of the detector chip, and py marks the y-direction position of the detector chip (seen in more detail in figure 4.11). px = [1, 100], and py = [1, 100]. Note that the px axis in figure 4.11 is in the other direction.

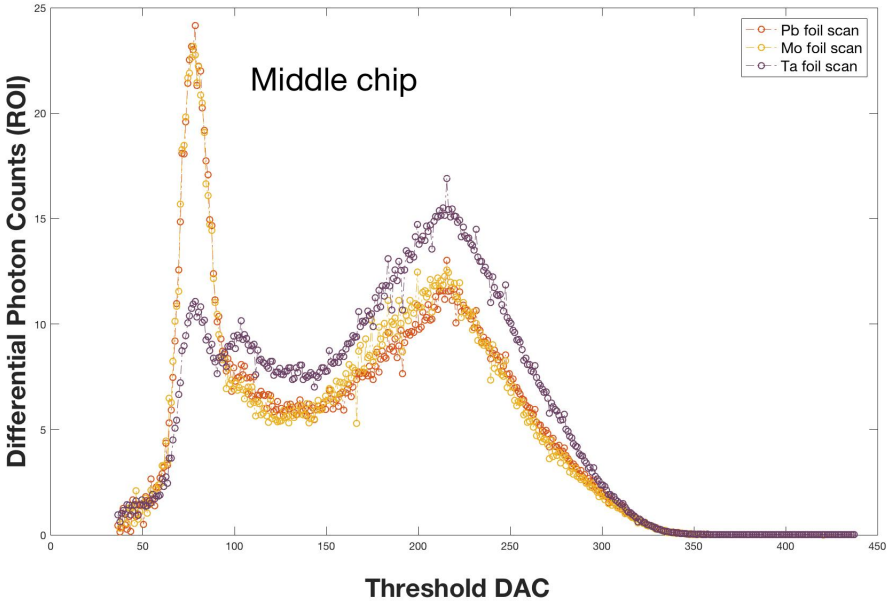

Figure 4.14: This plot shows the XRF signal for Mo, Ta, and Pb foils for the middle chip in MARS-15. The ROI is px = [130, 250], and py = [1, 100]. Note that the px axis in figure 4.11 is in the other direction.

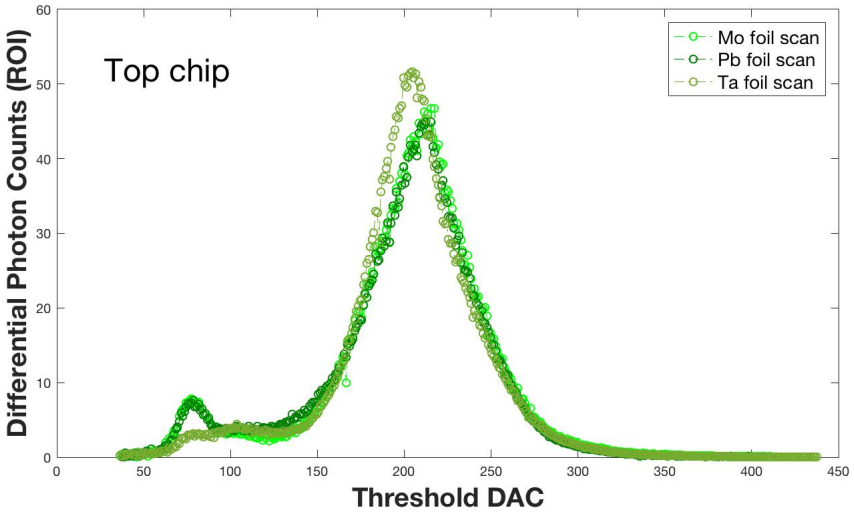

Figure 4.15: The top chip is furtherest away from the main beam. This plot shows the XRF signal for Mo, Ta, and Pb foils for the top chip in MARS-15. The ROI is px = [200, 380], and py = [1, 100]. Note that the px axis in figure 4.11 is in the other direction.

The global energy calibration is used to convert threshold DAC values to energy values. This enables the energy thresholds values, based on the DAC values, of each experimental peak to be determined. Each chip has a different energy calibration. The energy calibration for each detector chip is shown below.

Bottom chip:

$$ThresholdDAC = (2.66 \times Energy) + 9.7 \tag{4.1}$$

Middle chip:

$$ThresholdDAC = (3.51 \times Energy) + 16.8 \tag{4.2}$$

Top chip:

$$ThresholdDAC = (2.97 \times Energy) + 10.4 \tag{4.3}$$

Foil	(keV)	Bottom chip	Middle chip	Top chip
molybdenum	Peak 1	17	18	23
	Peak 2	57	56	68
tantalum	Peak 1	17	18	32
	Peak 2	57	56	65
lead	Peak 1	17	18	23
	Peak 2	57	56	68

Table 4.5: This table gives a summary of the XRF results for each chip, for each foil. Only the two major peaks are taken into account and are converted to an energy value using the global energy calibration. Theoretically molybdenum K_α occurs at 17 keV, tantalum K_α occurs at 58 keV, and lead K_α occurs at 75 keV.

4.5.2 Middle chip results for three foils

Results for the middle chip, for the same 3 foils and exposure parameters, are presented in figures 4.16, 4.17, and 4.18 below. Table 4.6 compares the theoretical K_α DAC values with the experimental K_α DAC values. Note that the theoretical

values are converted from energy (keV) to DAC using the global energy calibration.

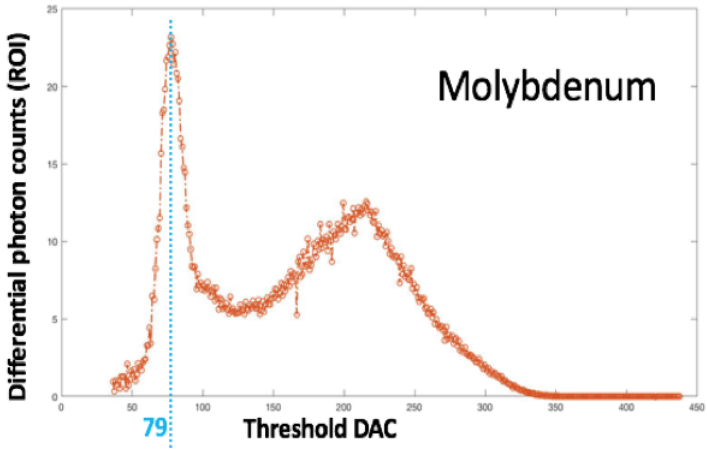

Figure 4.16: This plot shows the molybdenum XRF peak for the middle chip at a threshold DAC of 79. The ROI is px = [130, 250], and py = [1, 100].

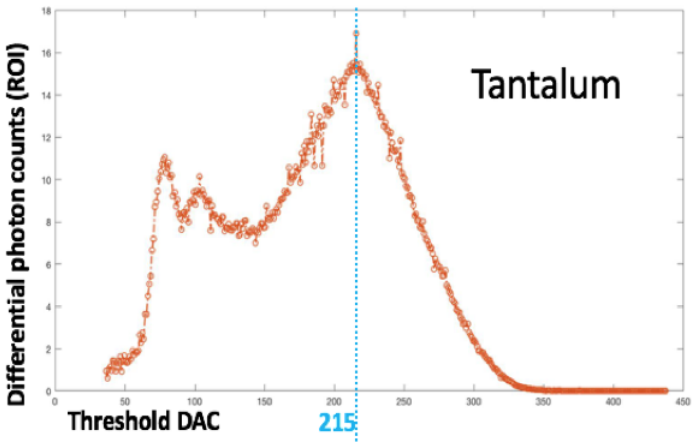

Figure 4.17: This plot shows the tantalum XRF peak for the middle chip at a threshold DAC of 215. The ROI is px = [130, 250], and py = [1, 100].

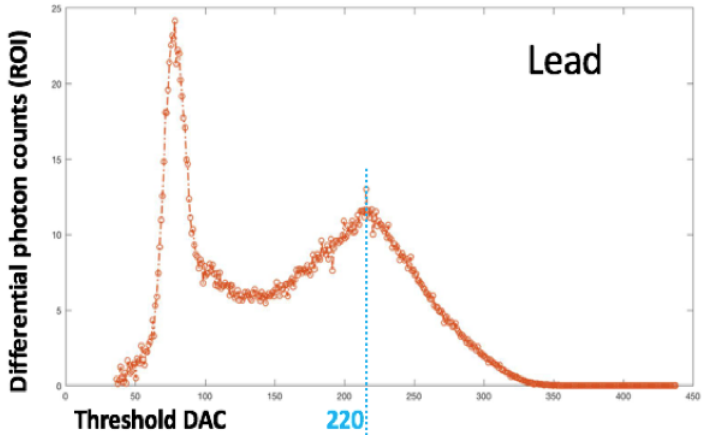

Figure 4.18: This plot shows the lead XRF peak for the middle chip at a threshold DAC of 220. The ROI is px = [130, 250], and py = [1, 100].

Foil material	Peak 1 (keV)	Peak 2 (keV)	Theoretical K_α (keV)
molybdenum	18	56	17
tantalum	18	56	58
lead	18	59	75

Table 4.6: Theoretical versus experimental K_α XRF peaks for molybdenum, tantalum, and lead foils (for the middle chip). Threshold DAC has been converted to energy using the global energy calibration.

4.6 Discussion

In this chapter I developed a method to detect XRF in a MARS scanner using an oblique transmission setup. The XRF setup and various scanner parameters were derived from the model created in the previous chapter. XRF was created by illuminating foils that are positioned on the front of the extrinsic filtration that is located between the x-ray source and the source collimators. When the primary x-ray beam is narrowed with the collimators, oblique XRF reaches the detector plane outside of the primary beam.

When the Mo foil is in front of the detector the XRF peak is well-defined and clearly visible compared to when the foil is positioned behind the collimators (Figure 4.9). This agrees with the model's findings of having the FDD as small as possible to increase the strength of the XRF signal. The results of this study prompted me to use the motor testing interface on the MARS GUI to override the anti-collision software and bring the foil and detector as close together as possible (minimise the FDD) for the rest of the experiments.

Figure 4.12 shows a comparison between the XRF signal when a Pb foil is taped behind the collimators versus when the foil is on the filter-bar (for the same FDD). Table 4.3 demonstrates at what energy values each of the observed peaks convert to with the global energy calibration. The theoretical lead K_α XRF peak occurs at 75.0 keV, while the K_β occurs at 84.9 keV. I suspect that peak (1b) is due to the cadmium or tellurium fluorescence (cadmium $K_\alpha = 23.2$ keV and $K_\beta = 26.1$ keV, tellurium $K_\alpha = 27.5$ keV and $K_\beta = 31.0$ keV). Peak (2b) could be lead fluorescence at 75.0 keV with a left shoulder (peak 2a) of partial charge summing, and a separate Cd or Te fluorescence signal down near 23/27 keV. Such a thought suggests that three pixels are counting in a line together. The x-ray tube has a tungsten anode. Tungsten K_α occurs at 59.3 keV and this could be another reason for peak (2a).

A reason for the difference in height and position of peak (1a) versus (1b), and peak (2a) versus (2b) in figure 4.12 may be due to the distance between the filter-bar and the collimators (section 4.4.6). When the foil is glued to the 1 mm Al filter-bar there is a significant distance between the foil and the collimators. The filter-bar is also placed in front of the x-ray source so the other foil elements on the filter-bar (tantalum and molybdenum) get illuminated, which may contaminate the lead XRF signal. However, when the foil is taped behind the collimators, there is no distance between the foil and the collimators. With this setup only the lead foil is illuminated and there is no contamination from other foils. In summary, these results demonstrate that having the foil on the filter-bar is not advantageous.

When the molybdenum, tantalum and lead foils are illuminated by the source (in seperate scans) the three chips of the Medipix3RX (bottom, middle and top) in MARS-15 respond similarly to each foil (figures 4.13, 4.14, and 4.15). Table 4.5 gives a summary of the peak energy values. However, if I only look at the foil spectra for the middle chip (figures 4.16, 4.17, and 4.18 for the molybdenum, tantalum and lead foils, respectively) the peak is approximately in the correct position when comparing the experimental and theoretical K_α values (table 4.6). The predominant peak for molybdenum and tantalum are approximately in the correct place. For lead, the predominant peak is at 18 keV and the secondary peak is at 59 keV. The theoretical K_α peak for lead is at 75 keV. The secondary peak may be lead fluorescence, the discrepancy between the experimental and theoretical value is given in the paragraph above.

The experimental results shown in this chapter allowed me to see limitations in the experimental design. The scanner parameters have been optimised using my XRF model (chapter 3), however, the experimental setup should be improved. It is not advantageous to have the foils glued to a 1 mm Al filter-bar that is placed in front of the scanner collimators. The filter-bar is also designed such that contamination from adjacent foils may be present due to overlap (figure 4.6a), though this was minimised by using narrow collimator settings. These are improvements that must be made for future foil scans in MARS.

Other sources of discrepancy may be: (1) the collimator positions that are set in the MARS GUI do not always match the physical position of the collimators, so part of the XRF beam could be blocked, resulting in a reduced XRF signal; (2) the kVp is set high enough to be able to produce lead XRF from the collimators which could contaminate the molybdenum and tantalum foil scans; (3) the filter-bar material and thickness (currently 1 mm Al) needs to be optimised such that maximum XRF escapes the foil. The Al should also be placed so that it attenuates the main beam and not the XRF produced from the foils (i.e., the source photons should pass through the aluminium of the filter-bar before creating XRF); (4) the Compton scatter contribution, even though it is deemed to be negligible [Tran et al., 2004], needs to be considered; and (5) cadmium and tel-

lurium contamination from the sensor crystal. The above processes may generate additional features and distort the XRF signal.

The foils on the filter-bar need to be of optimal thickness (chapter 3) and a larger foil area should be used such that more XRF reaches the detector. I assume that the centre point of the source aligns with the centre point of the foils on the filter-bar. This depends on accuracy of whoever put the filter-bar into the scanners.

There is a discrepancy between the optimal collimator positions predicted by the model in chapter 3 and the collimator shadow check done for the measurements in this chapter. The reason for this could be because the collimators are thicker or thinner than what is given in the specifications, or the collimator edges are not sharp and cause a penumbra effect.

The MARS GUI needs to allow for more precise movement of the collimators and SDD without having to go into the user-testing interface in the debug mode of operation. There are also mechanical limits on the collimator positions which do not allow the collimators to open up enough to select the entire surface of the top and bottom foils of the filter-bar.

In future foil scans a per-pixel analysis of the XRF signal will be done and used for a per-pixel energy calibration.

Multiple detector chips are used in MARS scanners to move towards human imaging and to be able to image larger objects, faster. The number of detector elements in MARS body-part scanners will depend on the size of the imaged object. Regardless of the number of detector-elements, the scanners will still be calibrated using the XRF method developed in this chapter. For a large object, the camera will have to be moved up or down significantly in order to be outside of the main beam. This is not feasible using the oblique transmission setup described in figure 4.4. An alternative setup uses the horizontal collimators to determine the position of the main beam. This approach does not require the detector to be

translated vertically. This is advantageous as MARS employs multi-chip cameras (i.e., 10, 12,..., 50 Medipix3RX detectors), therefore, not translating the detectors vertically enables equal XRF to reach each of the detectors. Figure 4.19 shows this approach schematically in a side view. This setup will be used in future XRF experiments.

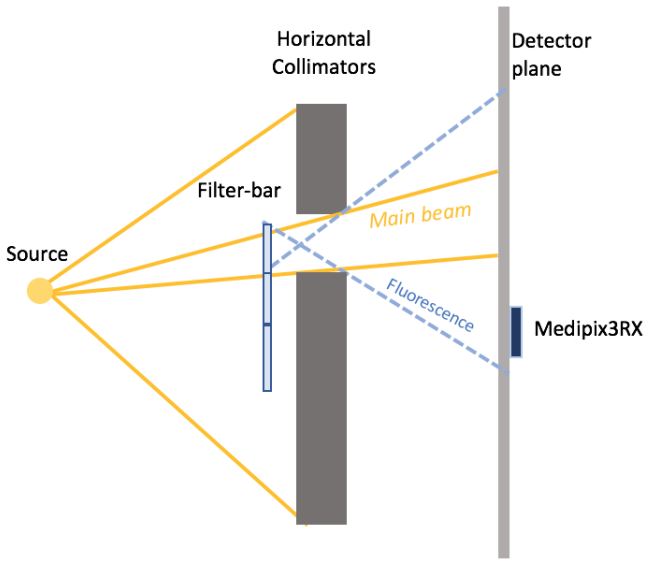

Figure 4.19: Top view where the horizontal collimators are used to select a molybdenum foil on a 3-foil filter-bar. The detector is not required to move up or down.

In summary, the method to detect XRF in a MARS scanner using an oblique transmission setup developed in this chapter offers results that can be used to characterise the energy response of the Medipix3RX multi-element camera. Transmission setups are typically not used to detect XRF as it is very difficult to get a strong enough signal. The setup presented in this chapter is novel as it increases the strength of the XRF signal in a transmission setup by measuring it off-axis. This is something is not commonly done in spectral imaging systems. The metallic foils are permanently mounted on the filter-bar (in addition to a range of filters) inside the MARS scanner, thereby providing an automatable method for generating the XRF photons.

Although the results presented in this chapter are for a ROI, it is very easy to obtain the data for the XRF spectra on a per-pixel basis (the spectra are just more noisy). The following chapter (chapter 5) uses synthetic data to characterise the energy response of the Medipix3RX as the XRF setup in this chapter requires further optimisation. The results in this chapter align with the MARS team goal of improving the spectral performance of the MARS scanner by offering a new method to characterise the Medipix3RX multi-element camera. This method developed in this chapter is translatable to the MARS large-bore scanner.

4.7 Summary

- A per-pixel energy calibration is advantageous as not every pixel in the detector matrix responds the same to a photon of the same energy. The cause of the inter-pixel variation could be due to imperfections in the sensor crystal, threshold dispersion, the ASIC electronics.
- XRF is created in MARS by illuminating metallic foils with the x-ray source in a transmission setup.
- The detector (camera) is moved out of the main beam (oblique) to avoid contamination from the polychromatic x-rays from the x-ray source that are used to induce excitation in the foil.
- XRF is monochromatic and detected using a multi-element MARS detector (camera).
- A well defined XRF signal in an oblique transmission setup is difficult to detect. The strength of the XRF signal is controlled by the filter-bar design, collimation, source-to-detector distance, the multi-element camera arrangement, and the filtration.
- The 3-chip camera has a staircase arrangement that causes shadows on the chips. These areas are avoided for the results.
- The bottom detector chip is closest to the main beam, followed by the middle chip and then lastly the top detector chip.
- The middle detector chip shows reasonable agreement between the theoretical and experimental K_α values for the molybdenum and tantalum foils. the

lead foil shows some discrepancy that could be due to the presence of scatter, cadmium or tellurium contamination from the sensor crystal, tungsten contamination from the source tube anode, partial charge sharing.

- Although the results are shown for a ROI, the per-pixel results are also available but are more noisy (no averaging).
- A similar setup can be used for the MARS large bore (human) scanner.

Chapter 5

Medipix3RX energy response

The purpose of this chapter is to develop a method to determine the energy response of a Medipix3RX detector using x-ray fluorescence (XRF) measurements emitted from metallic foils inside a MARS spectral imaging system. The main motivation behind this research came from an unpublished internal document titled "Using Beer's law in MARS scanners" which challenged the current image reconstruction. The energy response of the detector is an input to the new image reconstruction algorithm, which sets out to improve the quality of the images obtained with the MARS system.

An overview of image reconstruction in CT is given in section 5.2 and common reconstruction artefacts are outlined in section 5.2.1. The MARS forward problem is introduced in section 5.3 and the detector component of the forward problem is detailed in section 5.4. The detector component of the forward model is also called the detector function. Section 5.5 reports on using XRF to determine the detector energy response function. Synthetic XRF data is produced in section 5.6.1. The detector response, thus parameterised, is used to predict how different pixels and different counters of the Medipix3RX detector react to an incoming photon pulse of known energy in section 5.7.1. Finally, section 5.8 analyses the method and results of this chapter.

I would like to acknowledge Dr Ali Atharifard (MBI employee), Dr Niels de Ruiter (MBI employee) and Sikiru Adebileje (PhD student) as co-investigators for this

work. The work presented in this chapter is highly confidential. The intended audience for this chapter are current (and future) members of the MARS team. The chapter contains ideas that seem to be novel in regard to applications to CT reconstruction.

5.1 Introduction

A principal goal of the MARS project is to calculate the material composition of an unknown object contained in a known volume. An object's material composition is defined by a mathematical process known as image reconstruction. Image reconstruction in CT is a numeric process that generates images from x-ray projection data acquired at many angles around an object. Conventional CT reconstruction involves calculating the object's linear attenuation coefficient distribution $\mu(x, y)$ from a set of radiographic projections $p(r, \theta)$. In clinical CT the reconstruction techniques used are commonly based on filtered back projections and on the monochromatic Beer-Lambert law:

$$p(r, \theta) = -ln(I/I_0) = \int_{T(s)} \mu(x, y) ds \tag{5.1}$$

where I is the beam intensity, I_0 is the initial intensity of the beam, $T(s)$ is some ray path at a distance r and rotation angle θ. However, since CT scanners use polychromatic x-ray sources, this approximation results in energy dependent image distortions known as beam hardening artefacts.

5.2 Image reconstruction

Two major categories of CT reconstruction methods exist, analytical reconstruction and iterative reconstruction. A type of analytical reconstruction employs the filtered back projection (FBP) method. This involves inverting the monochromatic Beer-Lambert law, equation 5.1, (also known as Beer's law) using Fourier transforms and back-projecting the image along the lines they were taken from. The algebraic reconstruction technique (ART) employs solving linear equations. The original ART algorithm was an iterative technique developed by Kaczmarz

in 1936 [Kaczmarz, 1937]. An advantage of iterative algorithms is that they often tend to a smoother result close to the exact solution, and they don't need as much data [Tang et al., 2012].

When ART is used for CT image reconstruction it is solving a system of linear equations $Ax = b$ constructed from the discrete version of the monochromatic Beer-Lambert law.

$$p(r, \theta) \approx \sum_{v} \mu_v l_v \tag{5.2}$$

where v is the voxel index and l_v is the path length of the projection passing through voxel v.

To reconstruct with reduced artefacts each x-ray needs to be modelled by the polychromatic Beer-Lambert law. The forward problem is our attempt in moving from a monochromatic material reconstruction to a polychromatic reconstruction model.

5.2.1 Reconstruction artefacts

Reconstruction artefacts are commonly encountered in clinical CT and may give errors and distortions in the imaged object, resulting in false interpretations. Commonly encountered artefacts in CT include ring, cupping, and streak artefacts [Barrett and Keat, 2004]. Ring artefacts are caused by a mis-calibrated detector which results in rings centred on the centre of rotation. Beam hardening effects are visible in the form of cupping, and streak artefacts. Beam hardening occurs because the average energy of a transmitted spectrum increases while passing through an object [Rajendran et al., 2014]. Beam hardening in CT is common when using reconstruction techniques based on the monochromatic Beer-Lambert law. It has been shown that reconstruction techniques based on polychromatic models can eliminate beam hardening artefacts almost entirely [Jang et al., 2013; Maaß et al., 2011].

5.3 The forward problem

The MARS forward problem is MARS's attempt to move from a monochromatic image reconstruction to a polychromatic reconstruction. This new reconstruction algorithm divides the reconstruction problem into simple multiplying factors.

A MARS scan is carried out by using a source S of x-ray photons in the energy range of 20 to 120 keV where the photons travel in a beam B towards an object and some pass through the object in volume V and these photons are detected with detector D. All photons that reach the detector have a chance of getting detected. Some photons might be absorbed by the object before it can reach the detector. The critical components are the source S and the detector D. Algorithms then determine which materials m are within each voxel v of a region of space, which could be chosen to contain the object.

The geometric properties of the rays of the beam B that leave the source S and are incident on the pixels p in the detector, has been examined by other members of the team [Anjomrouz et al., 2018; Shamshad et al., 2017]. The filter F, the collimators C, and the geometry G are currently being investigated. The product of these factors gives J_E, the probable number of photons, at energy E, that are counted in each pixel when the volume V contains only air. This entire concept is the MARS equation and has been termed "the forward problem". It is important to note, however, that the MARS equation can be inverted and does not necessarily have to follow the feedback loop in the forward direction (even though it is termed the *forward* problem). The forward problem (or MARS equation) is given by:

$$Q_{cr} = \int_{E_{THL}}^{E_{KVP}} F_{er} C_{er} D_{ecr} S_{er} e^{\int_{d_{source}}^{d_{detector}} - \sum_m \mu_{em} X_{vm}^{dd}} .de \tag{5.3}$$

where Q are measurements, F describes the filter, C describes the collimators, D is the detector function, S is the source model, e is energy, c is the counter and and r is the ray (note that the ray can be split into alpha = gantry angle, and p = pixel). The exponential term is in the form of the Beer-Lambert law. When

integrating a line from the source to the detector linear attenuation values are accumulated to get the transmission. The linear attenuation has been converted to mass attenuation for each material m. The limits of the integral E_{KVP} and E_{THL} represent the tube voltage and the threshold energy, respectively.

Developing the detector function is the primary concern of this chapter. I call parameterising the detector's energy response "the detector function". The aim of this approach is to set up the required information so that the Beer-Lambert law can be used without the usual monochromatic approximations and accurate values of J_E can be obtained for the new reconstruction algorithm.

The goal of treating each of the components separately is also to answer questions about the properties and best operating conditions of the components of the system, especially (1) the geometric properties of the scanner, (2) the stability and accuracy of the source, (3) the many parameters of the Medipix3RX ASIC and (4) the various sensor crystals. A better reconstruction algorithm will calibrate the MARS system better.

5.4 Detector response function

It is extremely challenging to perform an analytical prediction of the detector response function due to the complex nature of the various physical processes involved. The detector response function at a given energy is defined as the detector's response to a monochromatic input spectrum. In this thesis the monochromatic source is created by passing a polychromatic x-ray beam through metallic foils in the MARS setup. A precise measurement of the response function, over a wide range of energies, can be performed by selecting multiple foils and moving the detector out of the main beam. This process is described in detail in chapter 4.

In the ideal pixel, D_E is a step function, 0 below $E_{\text{threshold}}$, and 1 above. For the MARS cameras the effective area of each pixel is $A_p = 110\ \mu m^2$. When we determine the response of each pixel, we will use this information to adjust the "perceived" area of the pixel. This will be recorded in the B function. The

B function contains information about the properties of the source beam. These properties include shapes of the measured beam profiles, the angular offsets, intra-scan variation, and the integrated counts at the beam centre [Anjomrouz, 2017]. Some pixels will appear to have a larger area than their default 110 μm^2. Others will have a smaller than expected area. At this stage, unresponsive pixels can be eliminated from the list of pixels in B. The effective pixel area of the MARS camera has been studied by other MARS team members [Anjomrouz, 2017; Shamshad et al., 2017].

5.5 XRF for determining the detector energy response function

The detector response function at a given energy is defined as the detector response to a monochromatic input spectrum. In this thesis the monochromatic input spectrum is created by passing a polychromatic x-ray beam through metallic foils to create distinct K_α lines. The position of the K_α lines for a series of foils is known (theoretically) and can be used to determine the response to a photon of energy E, for all counters in a pixel in charge summing mode (CSM), for various values of the energy thresholds of the counters.

For the detector function, D, we want to know what proportion of photons is likely to be detected at every energy within an energy bin. For example, if 1000 photons come in at 20 keV, how many of them will be counted if the counter is set to 15 keV? If 100 photons come in at 90 keV, how many of them will be counted if the counter threshold is set to 50 keV? etc.

An ideal detector, in response to a monochromatic incoming pulse, is a step function that steps up at the THL (K_α) value. This is shown in figures 5.1. However, the real curve has an s-like curve at the THL (K_α) and tapers off at the end as the photons get powerful enough to burst through the sensor without getting detected. This is shown in figure 5.2.

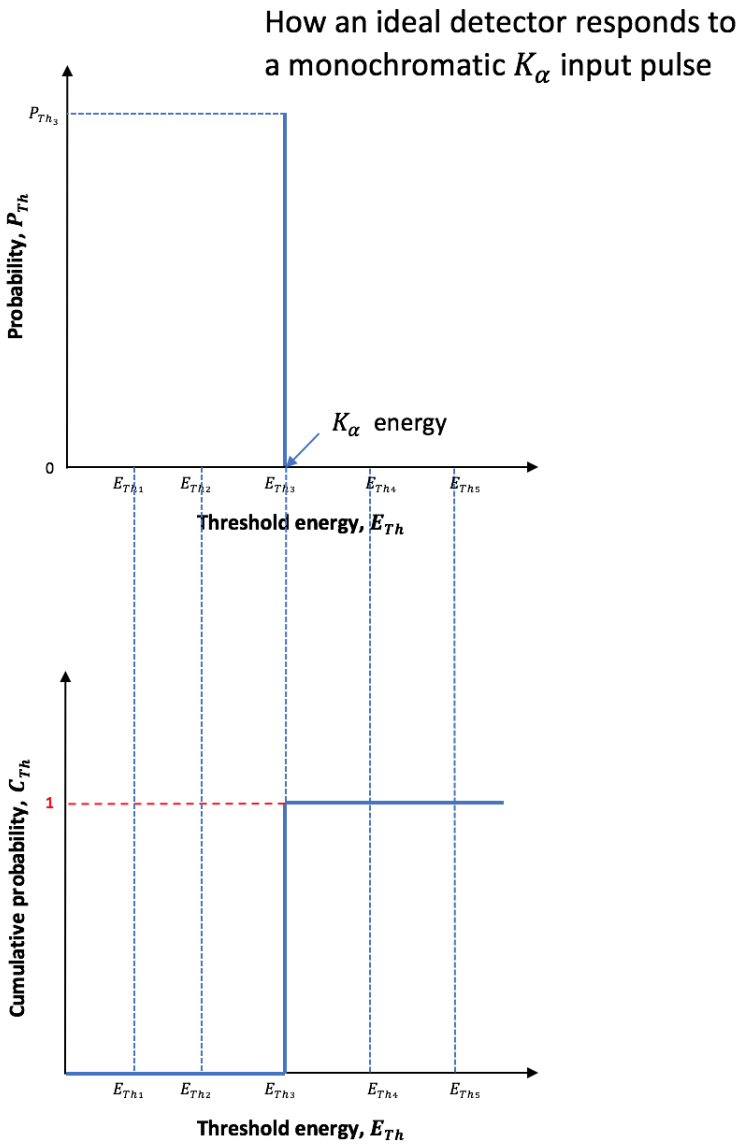

Figure 5.1: The top figure represents an ideal (monochromatic) K_α input pulse. The XRF occurs exactly at the theoretical K_α value with a probability of detection P_{K_α}. In the bottom figure, at threshold energy E_{Th1} the probability of the detector detecting this photon is 0, at E_{Th2} the probability of detection is 0, at threshold energy E_{Th3} the probability of detection is 1, at threshold energy E_{Th4} the probability of detection is 0. Therefore, the response function for the ideal detector is a step function.

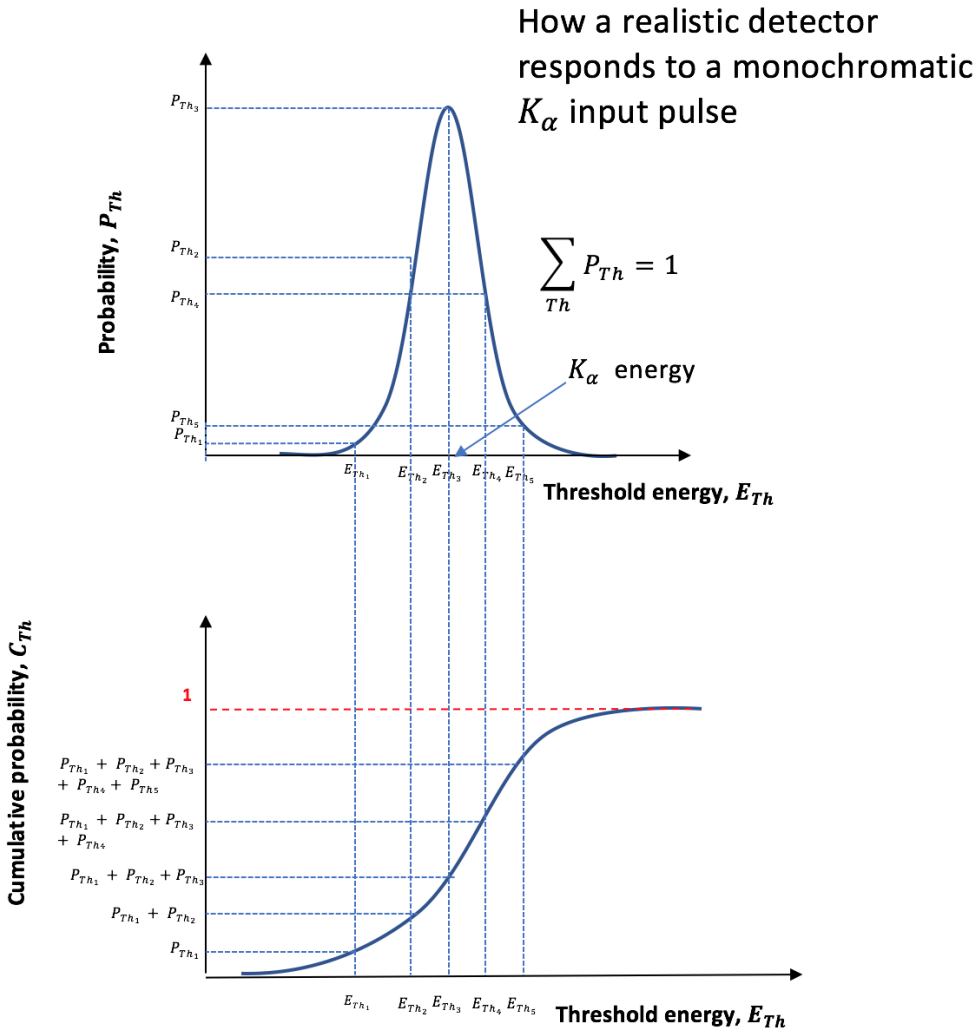

Figure 5.2: The top figure represents a realistic K_α input pulse. The K_α pulse is not truly monochromatic and it has a probability of being detected above and below the K_α value. In the bottom figure, at threshold energy E_{Th1} the probability of the detector detecting this photon is P_{Th1}, at E_{Th2} the probability of detection is $P_{Th1}+P_{Th2}$, at E_{Th3} the probability of detection is $P_{Th1}+P_{Th2}+P_{Th3}$, and so on. The cumulative probability of detecting the photon is 1. The realistic detector response function to a fluorescence photon has an s-like curve at the E_{Th}.

A function that models the x-ray source (S in equation 5.3) allows us to use XRF signals to estimate how many photons are emitted towards each counter of the detector and then we can directly measure how many photons get detected

by that counter. We don't have control over which energies we get to measure (a number of foils are used to provide a range of data points), but with enough foils we are able to get a reasonable approximation and use interpolation to fill the blanks.

Figure 5.3 shows the integral K_α counts for every counter threshold, when a beam of XRF photons are emitted from a metallic foil. The counter increases its counts for all photons above a set threshold. This is an integral count as it is equivalent to integrating over the spectrum. If we subtract the result between threshold values, we get a new measure for differential counts. Until the counter energy threshold is above the K_α energy value of the foil, the integral counts remain mostly constant. The three different lines are for three different foils with different K_α energy values.

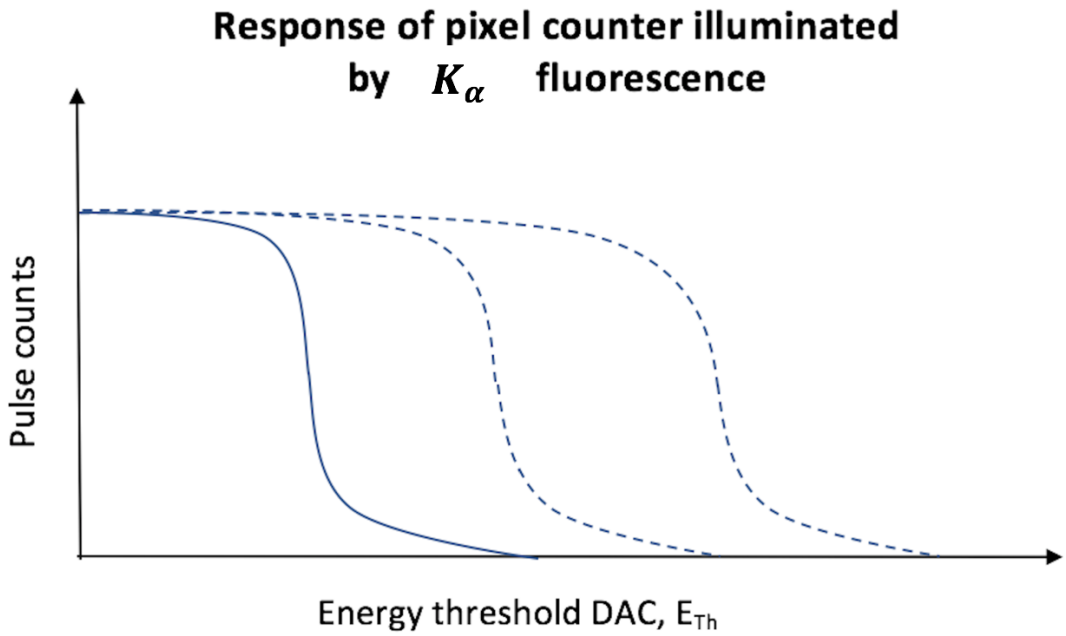

Figure 5.3: Plot showing the number of XRF counts if the source is K_α versus the counter energy threshold DAC. The dotted blue lines represent the K_α counts for two different foils.

5.6 Determining the detector energy response function

This section entails a set of instructions on how to go from the experimental XRF measurements, to the detector function (in a form that is desired by the image recovery team). XRF is created as in chapter 4. The resulting DICOM files are read by a Matlab function that I produced, and a plot of the integral photon counts against the threshold energy/DAC is created. The probability of fluorescence counts is obtained by normalising the y-axis (integral photon counts). An example of the raw integral data is shown in figure 5.3. It is expected that the maximum probability that a pixel counts an incoming photon pulse is greater than 1 (charge summing etc). Therefore, we can't normalise using the counts vector that we obtained experimentally. A possible solution is to use the XRF model developed in chapter 3) to normalise the experimental counts by using the maximum number of modelled counts. This is something that will be done in the future.

How can we take the probability of fluorescence counts and relate them to what the image recovery team wants for the detector function in the image reconstruction algorithm? It is actually quite simple, as figure 5.4 demonstrates in a 3D plot.

3D plot (figure 5.4) explained: The blue curves show what we can measure experimentally using foil fluorescence. Each blue curve represents a different foil, which has a different and specific K_α energy. The blue curves are created in two dimensions and represent photon probability (all we have to do is normalise the counts in figure 5.3 to get from counts to probability) versus counter energy threshold (DAC). The green dotted curve finds the probability of counting an incoming photon of energy E_γ, by a counter on the detector, if the counter energy threshold E_{Th} is set to a specific value.

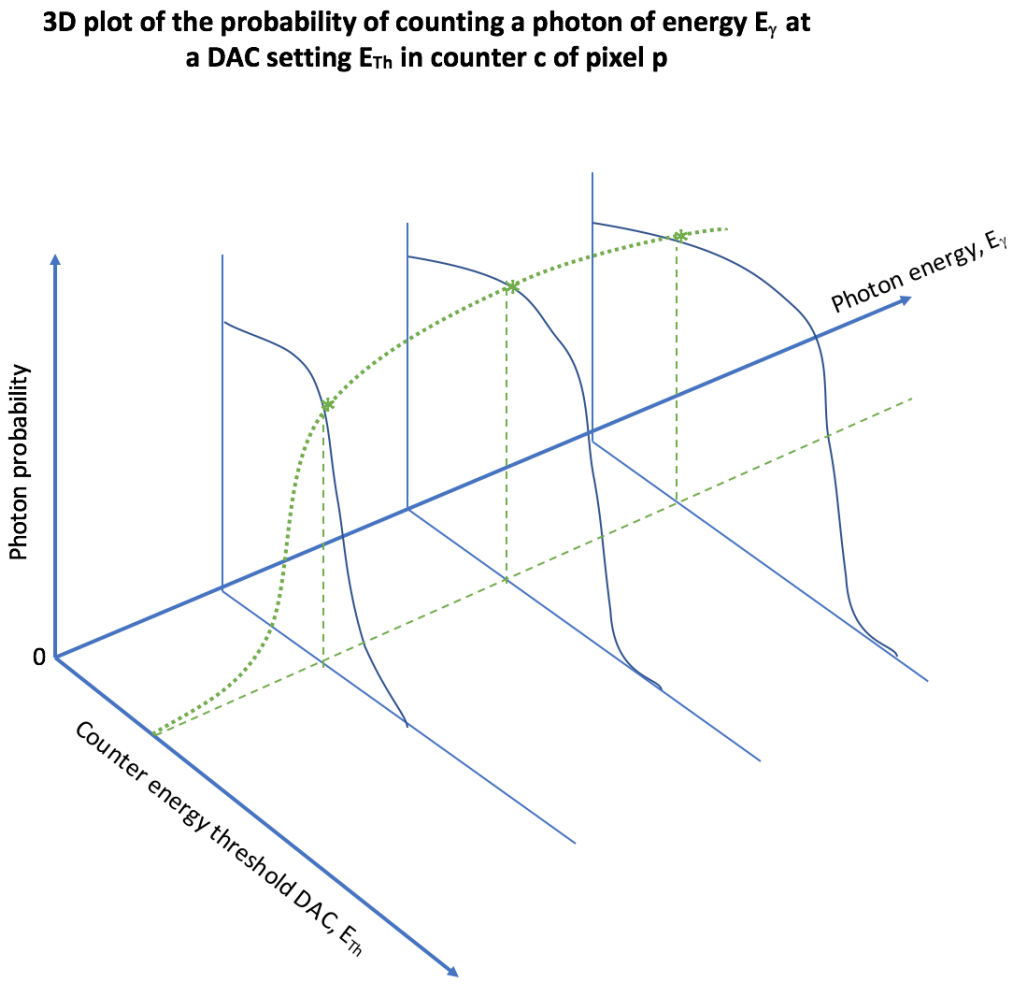

Figure 5.4: Three-dimensional plot showing how the probability of counting a photon of energy E_γ at a DAC setting E_{Th} in counter c of pixel p. The green line shows the curve that is of interest to the image recovery group and the blue curves show what we can measure from the foils.

5.6.1 Preliminary synthetic data

The detector energy response function is a theoretical function based on experimental XRF results. However, a well-defined fluorescence peak is difficult to detect experimentally, as has been shown in chapter 4. To get an idea of how the detector response function can be modelled using foil fluorescence, synthetic

data is used. This section discusses the steps involved in modelling the detector function from some preliminary synthetic data which imitates the experimental XRF data.

The synthetic data was produced based on years of experimental knowledge by Dr Ali Atharifard. Therefore, it is neither theoretical nor experimental, but a mix of the two. Some assumptions he made are:

1. Fluorescence broadens at higher energies due to the pre-amplifier gain.
2. The fluorescence peak has a symmetric Gaussian distribution where the peak occurs at a probability of 0.5.
3. The width of the differential fluorescence peak (slope of the integral curve) was decided based on XRF measurements previously made by Dr Raj Panta [Panta et al., 2015a].
4. The maximum counting probability is 1, and the minimum counting probability is 0.
5. The effect of pulse pileup is zero as the experimental data is collected outside of the main beam.

XRF data from Panta et al. [2015a], in addition to using the assumptions listed above, are used to create the synthetic data. Three different (integral) spectra are approximated, at $E_\gamma = 10$ keV, 65 keV, and 120 keV in figure 5.5, respectively. Each curve of figure 5.5 shows the preliminary synthetic data created from points at every 0.1 steps of probability of photon counting. Note that probability of photon counting is obtained from normalising the expected measurements made by the detector at each selected E_γ. The curves in figure 5.5 are equivalent to the blue curves in figure 5.4.

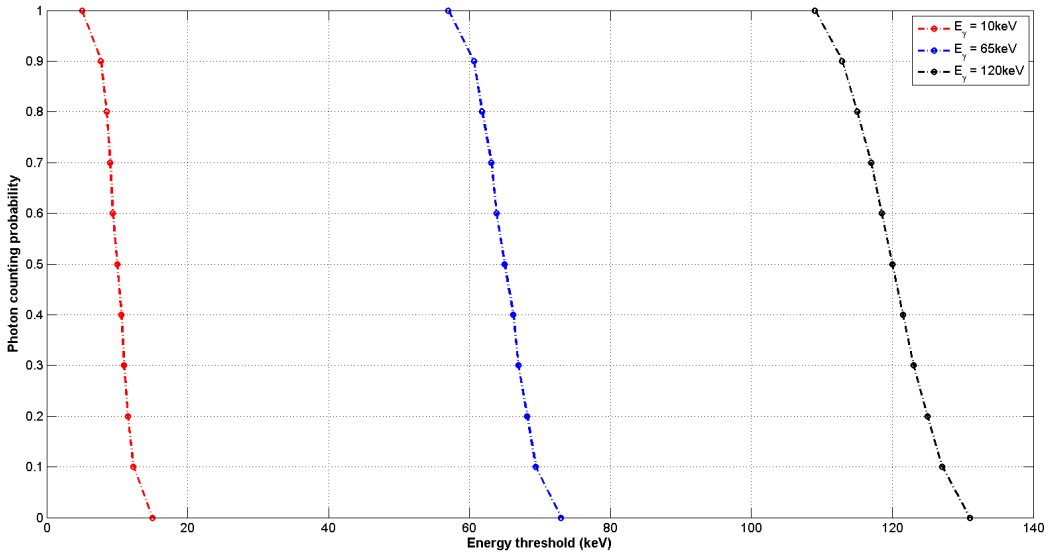

Figure 5.5: Preliminary synthetic data points representing the expected normalised measurements made of monochromatic photons of $E_\gamma = 10\,\text{keV}$, $65\,\text{keV}$, and $120\,\text{keV}$. These figures show the integral spectra.

5.7 Data processing

The green curve in figure 5.4 should be presented in a form that is useful to the image recovery team. A look up table is a suitable form, and is achieved by producing a mesh plot of the curves in figure 5.5. This is produced by two interpolations in three different steps:

- **Step 1:** The curves in figure 5.5 are interpolated along the x-direction (energy threshold) to obtain intermediate curves, with the same probability steps. For example, we interpolate the 3 existing curves to find an intermediate curve that has $E_\gamma = 30$ keV, in probability steps of 0.1. A shape-preserving piecewise cubic Hermite interpolating polynomial is used for this interpolation. This creates 111 vectors of length 11.
- **Step 2:** The 111 vectors (curves) are now interpolated in the y-direction (photon counting probability).

- **Step 3:** A similar interpolation method is used to find the photon counting probabilities at 1 keV spaced energy thresholds for different E_γ values. For example, take the 65 keV curve and use it to find the photon counting probabilities that correspond to energy threshold steps of 1 keV in the range 10-120 keV.

These interpolations create a matrix of size (111, 111) which includes a probability value for every 1 keV step of energy threshold and photon energy within the range [10, 120] keV. At this stage the probability of counting a photon of energy E_γ at energy threshold of E_{Th} will be known.

5.7.1 Data visualisation

The matrix of size (111,111) is visualised in a wireframe mesh plot, as shown in figure 5.6. A 3D surface is created using a linear interpolation applied to the synthetic data points. The colour bar shows the probability level at different E_γ and E_{Th}.

(a) Front view

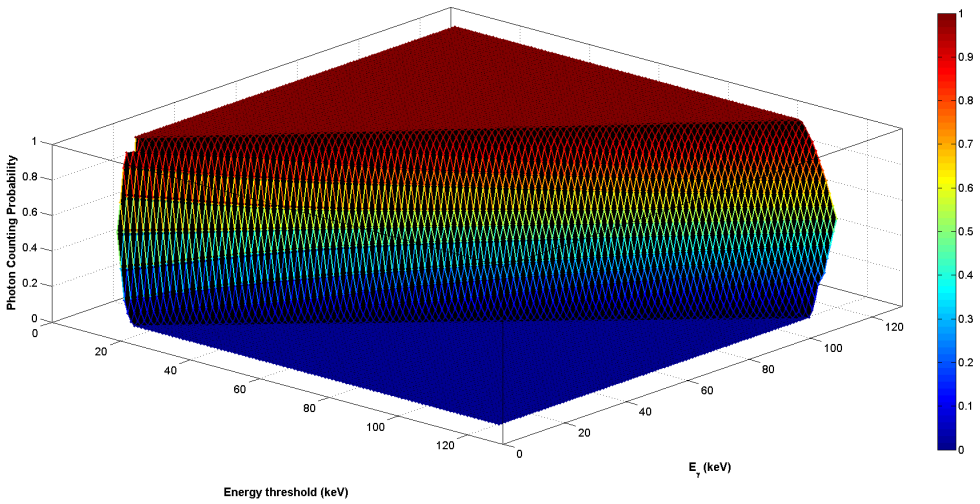

(b) Sideview

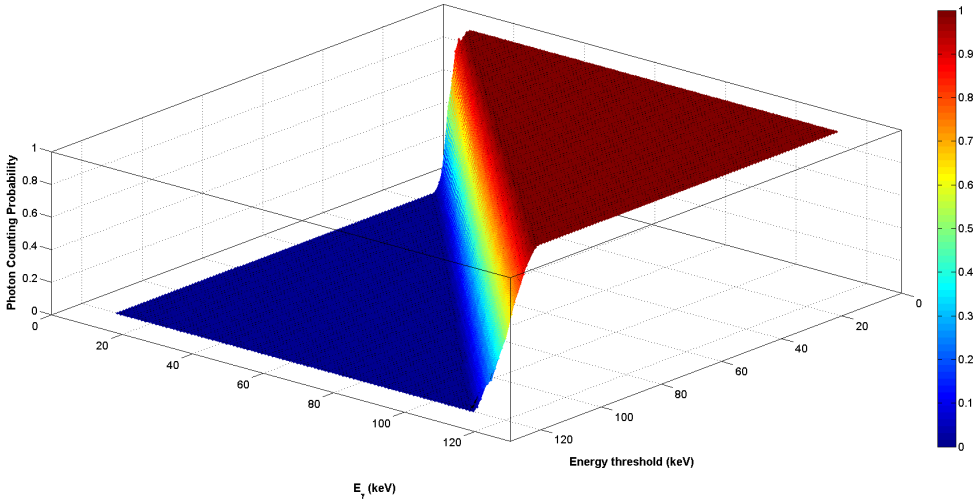

Figure 5.6: (a) front view, and (b) side view of the mesh plot created from interpolated synthetic data points. The colour bar shows the probability of counting photons at 1 keV energy thresholds when measuring photons of energy E_γ.

Viewing the 3D plot in 2D gives the plot in figure 5.7. When looking at the 2D plot with colour bar for every horizontal line from left to right, one is able to follow a S-shape function in which the probability changes from 0 (dark blue) to 1 (dark red). This is exactly what the image recovery team is looking for.

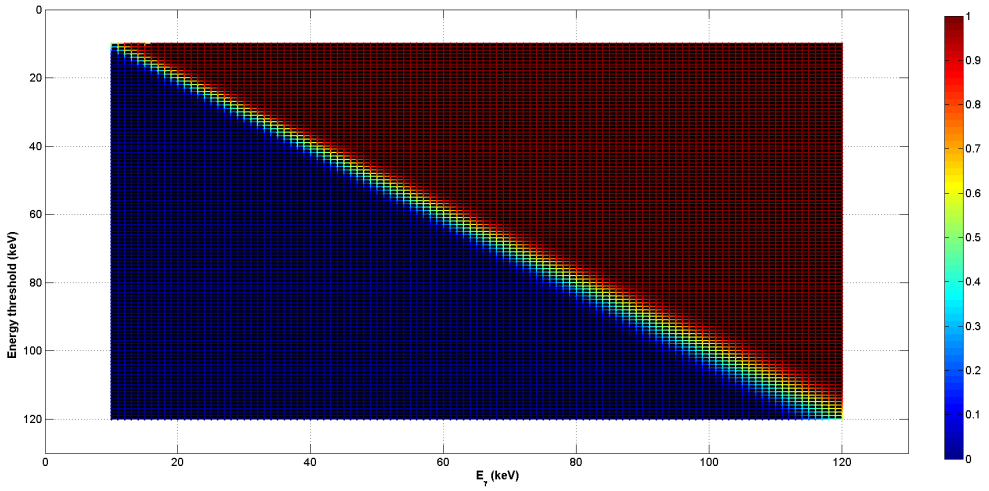

Figure 5.7: A 2D plot of energy thresholds against photon energy. Considering the colour-coded probability, following every horizontal line from left to right (a given energy threshold), a S-shape function. The probability changes from 0 (dark blue) to 1 (dark red).

5.7.2 Probability of counting a photon

The detector function D is now able to tell us the proportion of photons likely to be detected at every energy within an energy bin. A summary of the results are shown in table 5.1. It answers the question of "what is the probability of a photon of a certain energy coming in and being detected by the detector if the energy threshold of a counter is set to some energy?".

Photon energy (keV) (keV)	20	20	60	60	100	100
Counter threshold energy (keV)	15	25	55	65	95	105
Counting probability (4 s.f.)	0.9957	0.004288	0.9361	0.06394	0.8419	0.1581

Table 5.1: This table shows the probability of a photon of certain energy being counted if the counter threshold is set at a specific energy. For example, I can now answer the question "if 1000 photons come in at 20 keV, how many of them will be counted by a counter on the detector if the counter is set to 15 keV?". In this case the answer is $0.9957 \times 1000 = 995$ photons.

5.8 Discussion

This chapter has detailed the development of a method that uses XRF to characterise the energy response function of the Medipix3RX detectors used inside the MARS scanners. Synthetic XRF data is used to describe the probability of counting a photon of energy E_γ at a DAC setting E_{Th} in counter c of pixel p. This allows the image reconstruction team to reconstruct MARS images without the usual approximations and improves the quality of the images obtained with the MARS system.

The detector response function at a given energy is defined as the detector response to a monochromatic input spectrum. The monochromatic input spectrum is represented by synthetic XRF data. The probability of counting a photon of energy E_γ at energy threshold E_{Th} is known. For example, if photons come in at 20 keV, the probability of them being counted by a counter on the detector if the counter is set to 15 keV is 0.9957. Similarly, if photons come in at 60 keV, the probability of them being counted by a counter on the detector if the counter is set to 65 keV is 0.06394. Table 5.1 will be extended to a complete look up table in the energy range 20 - 120 keV. This enables the probabilities to be implemented in the MARS forward model, enabling the new reconstruction algorithm to be used in the MARS imaging chain.

The interpolations presented in this chapter are not tested using real data. The synthetic data makes the following assumptions. It assumes that: (1) fluorescence broadens at higher energies due to the pre-amplifier gain; (2) the XRF peak has a Gaussian distribution, and occurs at a probability of 0.5; (3) charge sharing is negligible; (4) fluorescence does not escape to neighbouring pixels; and (5) the effect of pulse pileup is zero as the data is collected outside of the main beam.

These assumptions are justified but will be removed when real data is used. A pulse pileup model developed by Atharifard [2017] is going to be incorporated into the forward model in the near future. A shape-preserving piecewise cubic Hermite interpolating polynomial (pchip) is used to interpolate along the energy threshold and photon counting probability axes. In this case, the pchip function is preferred over the cubic spline interpolation (spline) function as the integral curves that are being interpolated do not oscillate freely between the data points, so the movement between the points does not need to be captured.

The experimental XRF measurements from chapter 4 need to be optimised further so that the method to characterise the energy response of the Medipix3RX can be applied to real data. It is expected that real data collection will be performed in late 2019. It is anticipated that it will be easy to integrate real data XRF measurements to describe the detector part of "forward model" using the method developed in this chapter.

The method to characterise the Medipix3RX presented in this chapter is independent of the sensor crystal. However, the detection efficiency needs to be accounted for. Detection efficiencies for common semiconductor materials (such as GaAs, CdTe, CdZnTe) as a function of photon energy are given in [Panta et al., 2015a]. Quantum detection efficiency decreases exponentially with photon energy. Similarly, the quantum efficiency is higher for higher atomic number materials. Future implementations of this method should account for the detector efficiency.

A benefit of the method presented in this chapter is that it is not limited to use in the Medipix3RX. The method presented in this chapter can be used for most energy-discriminating photon-processing detectors. this is advantageous as the Medipix4 is due to be released in 2020.

A principal goal of the MARS project is to calculate the material composition of an unknown object contained in a known volume. An object's material composition is defined by the image reconstruction. Conventional image reconstruction assumes a monochromatic input beam, which causes distortions in the imaged object. Reconstruction techniques based on a polychromatic input beam can significantly reduce image distortions. Accounting for a polychromatic input spectrum requires an analytical prediction of the detector response function. This is extremely challenging due to the complex nature of the various physical processes involved. The method to characterise the energy response of the Medipix3RX developed in this chapter (detector response function) is an important part of the MARS forward model that will allow the MARS reconstruction chain to model a polychromatic spectrum.

5.9 Summary

- A principal goal of the MARS project is to calculate the material composition of an unknown object contained in a known volume. An object's material composition is defined by a mathematical process known as image reconstruction. In conventional CT the reconstruction techniques used are commonly based on filtered back projections and on the monochromatic Beer-Lambert law.
- Image reconstruction has a fundamental impact on image quality. A monochromatic input beam results in image distortions and may result in false interpretations of the images.
- The MARS forward problem is MARS's attempt to move from a monochromatic image reconstruction to a polychromatic reconstruction. The new reconstruction algorithm divides the reconstruction problem into simple multiplying factors. The characterisation of the detector's energy response

is one of these factors. It is called the detector response function.

- The detector response function at a given energy is defined as the detector response to a monochromatic input spectrum. It is extremely challenging to perform an analytical prediction of the detector response function due to the complex nature of the various physical processes involved.
- The position of the K_α lines for a series of foils is known (theoretically) and can be used to determine the response to a photon of energy E, for all 8 counters in a pixel in charge summing mode (CSM), for various values of the energy thresholds of the counters. The creation of XRF is discussed in detail in chapter 4.
- Synthetic XRF data is interpolated in two directions using a shape-preserving piecewise cubic Hermite interpolating polynomial function that gives the probability of counting a photon of energy E_γ at energy threshold E_{Th}.
- The data is visualised in a wireframe mesh plot and viewing the plot in two dimensions gives the probability of counting a photon of energy E_γ at energy threshold E_{Th}.

Chapter 6

Conclusion

This chapter summarises the results of this thesis with respect to the research aims and objectives. The primary goal of this thesis was to characterise the energy response of the Medipix3RX detector in a MARS spectral scanner using x-ray fluorescence (XRF). Characterising the energy response improves the quality of MARS images by improving the 2D spectroscopic data. The MARS large-bore scanner uses multiple detector elements, therefore characterising its energy response is critical. The work in this thesis is translatable to the MARS large-bore technology and the concluding section of this chapter provides an outlook and future direction of how the research in this thesis will be extended. The work presented in this thesis provides economic and health benefits to New Zealand through improving the spectral performance of the MARS spectral imaging system.

6.1 Summary

The research in this thesis demonstrates the progression of the thesis goal (detector characterisation) through various stages. Each chapter represents a different stage, which follows on from the previous stage. The research in this thesis represent a cohesive collection of ideas.

In chapter 3 an analytical model that quantifies XRF production and detec-

tion in MARS was presented. The model is able to identify where in the detector plane XRF is maximum. Additionally, the model optimises parameters for XRF detection in MARS, without the need for time-consuming experiments.

XRF is detected in the MARS small-bore scanner by placing a metallic foil in front of the x-ray source and off-axis XRF is measured. The model breaks down aspects of the physical system and models individual scanner and geometric parameters. Some of these include foil thickness, tube voltage, tube current, exposure time, filtration, collimation, and the source-to-detector distance. The effect of each of these parameters is summarised in chapter 4. The source-to-detector distance (SDD) is a parameter that has a large effect on the strength of the XRF signal. The SDD is given by the source-to-foil distance (SFD) plus the foil-to-detector distance (FDD). The model has shown that a decrease of 0.5 cm in FDD increases the XRF signal (at the (0,0) position in the detector plane) by approximately 2%. A summary of the optimal scanner parameters are shown in table 3.3.

Chapter 4 developed a method to detect XRF in a MARS scanner using an oblique transmission setup. The detector consists of a Medipix3RX bump bonded to a CdZnTe sensor material. XRF was created by illuminating foils that are positioned on the front of the extrinsic filtration that is located between the x-ray source and the source collimators. When the primary x-ray beam is narrowed with the collimators, wide angle (oblique) XRF reaches the detector plane outside of the primary beam.

As a result of the model developed in chapter 3, anti-collision software on the MARS scanner was overridden to minimise the FDD. A comparison between having the foil on the filter-bar versus having the foil taped to the collimators (for the same FDD) showed that having the foil on the filter-bar is not advantageous. In another XRF scan it was shown that the XRF signal for all three foils (molybdenum, tantalum and lead) are contaminated by cadmium and/or tellurium fluorescence, XRF from the tungsten anode, scatter from the lead collimators, XRF from the lead collimators, and partial charge summing.

Multiple detector chips are used in MARS scanners to move towards human imaging and to be able to image larger objects, faster. The XRF scans in chapter 4 were obtained with a three-chip-camera in MARS-15 which show that in an oblique transmission setup, the bottom chip (closest to the primary beam) is largely saturated, the top chip (furtherest away from the primary beam) does not have a significant XRF signal, and the middle chip has the most defined and useable XRF signal. The position of the XRF peaks for the molybdenum, tantalum and lead foils for the middle chip are in agreement with the theoretical values. An alternative setup for multiple detector chips that controls the size and position of the main beam by moving the horizontal collimators, and not the camera, was suggested.

The results from the experimental scans suggests that, in order to get a more defined and accurate (closer to the theoretical value) XRF signal, the experimental setup and parameters require further optimisation. It is also not advantageous to have the foils glued to a 1 mm Al filter-bar that is placed in front of the scanner collimators. The foils on the filter-bar need to be of optimal thickness (chapter 3) and a larger foil area should be used such that more XRF reaches the detector.

The method to detect XRF in a MARS scanner using an oblique transmission setup developed in this chapter offer results that are able to characterise the energy response of the Medipix3RX multi-detector-element camera. Chapter 5 details the development of a method that uses XRF to characterise the energy response of the Medipix3RX detectors used inside the MARS scanners. Synthetic XRF data is used to describe the probability of counting a photon of energy E_γ at a DAC setting E_{Th} in counter c of pixel p. This allows the image reconstruction team to reconstruct MARS images without the usual approximations and improves the quality of the images obtained with the MARS system.

This method gives the probability of counting a photon of energy E_γ at energy threshold E_{Th}. A major advantage of the model and methods presented in this thesis is that they are not limited to use in the Medipix3RX and can be applied to most energy-discriminating photon-processing detectors. Several

MARS researchers are currently working on acquiring the required information (well-defined XRF signal) to complete the detector response component of the MARS forward model. It is expected that real data tests will be performed early 2019.

6.2 Outlook

The chapters of this thesis enable further improvements to the MARS imaging chain by improving the spectral performance of the Medipix3RX detectors. The methods developed in this thesis are translatable to the MARS large-bore (human) scanner. The XRF model developed in this thesis is not limited to use inside MARS and could be used to model transmission XRF in other x-ray imaging systems. The oblique, transmission XRF setup and method developed in this thesis are relevant to numerous x-ray imaging systems that aim to detect XRF using a transmission setup. The method to characterise the Medipix3RX detector presented in chapter 5 is applicable to the Medipix series of energy-discriminating photon-processing detectors. The next generation of Medipix detectors, the Medipix4, is due for release in 2020 and all of the work presented in this thesis will be relevant to the new detector, and any new sensor materials that will be used in MARS scanners in the future.

In conclusion, the work in this thesis has provided a cohesive understanding of how XRF can be used to improve the spectral performance of MARS imaging systems. This contributes to the MARS team motivation of providing economic and health benefits to New Zealand.

References

Aamir, R., Chernoglazov, A., Bateman, C., Butler, A., Butler, P., Anderson, N., Bell, S., Panta, R., Healy, J., Mohr, J., et al. (2014). Mars spectral molecular imaging of lamb tissue: data collection and image analysis. *Journal of Instrumentation*, 9(02):P02005. 4, 5

Alvarez, R. E. and Macovski, A. (1976). Energy-selective reconstructions in x-ray computerised tomography. *Physics in Medicine and Biology*, 21(5):733–744. 8

Anderson, N., Butler, A., Scott, N., Cook, N., Butzer, J., Schleich, N., Firsching, M., Grasset, R., De Ruiter, N., Campbell, M., et al. (2010). Spectroscopic (multi-energy) ct distinguishes iodine and barium contrast material in mice. *European radiology*, 20(9):2126–2134. 2

Anderson, N. G. and Butler, A. P. (2014). Clinical applications of spectral molecular imaging: potential and challenges. *Contrast media & molecular imaging*, 9(1):3–12. 2

Anjomrouz, M. (2017). *Investigation of MARS Spectral CT: X-ray Source and Detector Characterization*. PhD thesis, University of Otago. 88

Anjomrouz, M., Shamshad, M., Panta, R. K., Broeke, L. V., Schleich, N., Atharifard, A., Aamir, R., Bheesette, S., Walsh, M. F., Goulter, B. P., et al. (2018). Beam profile assessment in spectral ct scanners. *Journal of applied clinical medical physics*, 19(2):287–297. 86

Atharifard, A. (2017). *Characterization of X-ray Detectors for MARS Spectral CT Technology*. PhD thesis, University of Otago. 12, 26, 54, 61, 100

Atharifard, A., Healy, J., Goulter, B., Ramyar, M., Broeke, L. V., Walsh, M., Onyema, C., Panta, R., Aamir, R., Smithies, D., et al. (2017). Per-pixel energy calibration of photon counting detectors. *Journal of Instrumentation*,

12(03):C03085. 55, 60

Attix, F. H. (2008). *Introduction to radiological physics and radiation dosimetry*. John Wiley & Sons. 19, 20

Ballabriga, R. (2009). *The Design and Implementation in 0.13µm CMOS of an Algorithm Permitting Spectroscopic Imaging with High Spatial Resolution for Hybrid Pixel Detectors*. PhD thesis, CERN. 20, 21

Ballabriga, R., Alozy, J., Blaj, G., Campbell, M., Fiederle, M., Frojdh, E., Heijne, E., Llopart, X., Pichotka, M., Procz, S., et al. (2013). The medipix3rx: a high resolution, zero dead-time pixel detector readout chip allowing spectroscopic imaging. *Journal of Instrumentation*, 8(02):C02016. 22, 25, 27, 54

Ballabriga, R., Alozy, J., Campbell, M., Frojdh, E., Heijne, E., Koenig, T., Llopart, X., Marchal, J., Pennicard, D., Poikela, T., et al. (2016). Review of hybrid pixel detector readout asics for spectroscopic x-ray imaging. *Journal of Instrumentation*, 11(01):P01007. 9

Ballabriga, R., Campbell, M., Heijne, E., Llopart, X., Tlustos, L., and Wong, W. (2011). Medipix3: A 64k pixel detector readout chip working in single photon counting mode with improved spectrometric performance. *Nuclear Instruments and Methods in Physics Research Section A: Accelerators, Spectrometers, Detectors and Associated Equipment*, 633:S15–S18. 25

Bambynek, W., Crasemann, B., Fink, R., Freund, H.-U., Mark, H., Swift, C., Price, R., and Rao, P. V. (1972). X-ray fluorescence yields, auger, and coster-kronig transition probabilities. *Reviews of modern physics*, 44(4):716. 62

Barrett, J. F. and Keat, N. (2004). Artifacts in ct: recognition and avoidance. *Radiographics*, 24(6):1679–1691. 85

Bateman, C. J. (2015). *Methods for material discrimination in MARS multi-energy CT*. PhD thesis, University of Otago. 18

Berger, M. (2010). Xcom: photon cross sections database. *http://www. nist. gov/pml/data/xcom/index. cfm*. 19, 37

Bruyndonckx, P., Sasov, A., and Liu, X. (2011). Laboratory 3d micro-xrf/micro-ct imaging system. In *AIP Conference Proceedings*, volume 1365, pages 61–64. AIP. 57

Butler, A., Butler, P., Bell, S., Chelkov, G., Dedovich, D., Demichev, M., Elkin,

V., Gostkin, M., Kotov, S., Kozhevnikov, D., et al. (2015). Measurement of the energy resolution and calibration of hybrid pixel detectors with gaas: Cr sensor and timepix readout chip. *Physics of Particles and Nuclei Letters*, 12(1):59–73. 51, 57, 58

Gimenez, E., Ballabriga, R., Campbell, M., Horswell, I., Llopart, X., Marchal, J., Sawhney, K., Tartoni, N., and Turecek, D. (2011). Study of charge-sharing in medipix3 using a micro-focused synchrotron beam. *Journal of Instrumentation*, 6(01):C01031. 25

He, P., Yu, H., Bennett, J., Ronaldson, P., Zainon, R., Butler, A., Butler, P., Wei, B., and Wang, G. (2013). Energy-discriminative performance of a spectral micro-ct system. *Journal of X-ray Science and Technology*, 21(3):335–345. 9

Hubbell, J. (2004). Tables of x-ray mass attenuation coefficients and mass energy-absorption coefficients (version 1.4). *http://physics. nist. gov/xaamdi*. 62

Jang, K. E., Lee, J., Sung, Y., and Lee, S. (2013). Information-theoretic discrepancy based iterative reconstructions (idir) for polychromatic x-ray tomography. *Medical physics*, 40(9). 85

Johns, H. and Cunningham, J. (1983). The physics of radiology (springfield, il: Charles c thomas). 18, 20

Johnson, T. R., Krauss, B., Sedlmair, M., Grasruck, M., Bruder, H., Morhard, D., Fink, C., Weckbach, S., Lenhard, M., Schmidt, B., et al. (2007). Material differentiation by dual energy ct: initial experience. *European radiology*, 17(6):1510–1517. 8

Kaczmarz, S. (1937). Agent dherte auflosung von systemen linearer gleichungen. *Bulletin international de l'Acadmie polonaise des sciences et des lettres.*, 35:355–357. 85

Koenig, T., Hamann, E., Procz, S., Ballabriga, R., Cecilia, A., Zuber, M., Llopart, X., Campbell, M., Fauler, A., Baumbach, T., et al. (2013). Charge summing in spectroscopic x-ray detectors with high-z sensors. *IEEE Transactions on Nuclear Science*, 60(6):4713–4718. 27

König, T. (2011). Exploring coherent phenomena and energy discrimination in x-ray imaging. 25

Liu, X., Yu, L., Primak, A. N., and McCollough, C. H. (2009). Quantitative imaging of element composition and mass fraction using dual-energy ct: Three-

material decomposition. *Medical physics*, 36(5):1602–1609. 8

Maaß, C., Meyer, E., and Kachelrieß, M. (2011). Exact dual energy material decomposition from inconsistent rays (mdir). *Medical physics*, 38(2):691–700. 85

Manuilskiy, A., Norlin, B., Nilsson, H.-E., and Fröjdh, C. (2004). Spectroscopy applications for the medipix photon counting x-ray system. *Nuclear Instruments and Methods in Physics Research Section A: Accelerators, Spectrometers, Detectors and Associated Equipment*, 531(1-2):251–257. 55

MARS, B. (2018). First living human images from a mars photon-counting 8-energy ct, booktitle=IEEE Conference Proceedings, 7, 11

Moghiseh, M., Aamir, R., Panta, R. K., de Ruiter, N., Chernoglazov, A., Healy, J., Butler, A., and Anderson, N. (2016). Discrimination of multiple high-z materials by multi-energy spectral ct–a phantom study. *JSM Biomed Imaging Data Pap*, 61:1007. 3

Panta, R. K., Walsh, M. F., Bell, S. T., Anderson, N. G., Butler, A. P., and Butler, P. H. (2015a). Energy calibration of the pixels of spectral x-ray detectors. *IEEE transactions on medical imaging*, 34(3):697–706. 25, 54, 55, 94, 100

Panta, R. K., Walsh, M. F., Bell, S. T., Anderson, N. G., Butler, A. P., and Butler, P. H. (2015b). Energy calibration of the pixels of spectral x-ray detectors. *IEEE transactions on medical imaging*, 34(3):697–706. 55, 59

Pelgrom, M. J., Duinmaijer, A. C., and Welbers, A. P. (1989). Matching properties of mos transistors. *IEEE Journal of solid-state circuits*, 24(5):1433–1439. 55

Pfeiffer, K.-F. G. (2004). *Evaluation of the Medipix detectors for medical X-ray imaging, with special consideration of mammography*. PhD thesis, Citeseer. 13

Podgorsak, E. B. et al. (2005). Radiation oncology physics. *Vienna: International Atomic Energy Agency*, pages 123–271. 19, 20

Prebble, H. (2018). *Unpublished PhD thesis*. PhD thesis, University of Canterbury. 4

Rajendran, K., Löbker, C., Schon, B. S., Bateman, C. J., Younis, R. A., de Ruiter, N. J., Chernoglazov, A. I., Ramyar, M., Hooper, G. J., Butler, A. P., et al.

(2017). Quantitative imaging of excised osteoarthritic cartilage using spectral ct. *European radiology*, 27(1):384–392. 6

Rajendran, K., Walsh, M., De Ruiter, N., Chernoglazov, A., Panta, R., Butler, A., Butler, P., Bell, S., Anderson, N., Woodfield, T., et al. (2014). Reducing beam hardening effects and metal artefacts in spectral ct using medipix3rx. *Journal of Instrumentation*, 9(03):P03015. 85

Ronaldson, J., Walsh, M., Nik, S., Donaldson, J., Doesburg, R., van Leeuwen, D., Ballabriga, R., Clyne, M., Butler, A., and Butler, P. (2011). Characterization of medipix3 with the mars readout and software. *Journal of Instrumentation*, 6(01):C01056. 25

Schlomka, J., Roessl, E., Dorscheid, R., Dill, S., Martens, G., Istel, T., Bäumer, C., Herrmann, C., Steadman, R., Zeitler, G., et al. (2008). Experimental feasibility of multi-energy photon-counting k-edge imaging in pre-clinical computed tomography. *Physics in Medicine & Biology*, 53(15):4031. 25

Shamshad, M., Anjomrouz, M., Smithies, D., Largeau, A., Lu, G., Atharifard, A., Broeke, L. V., Aamir, R., Panta, R., Walsh, M., et al. (2017). Semi-analytic off-axis x-ray source model. *Journal of Instrumentation*, 12(10):P10013. 34, 86, 88

Smith-Bindman, R., Miglioretti, D. L., and Larson, E. B. (2008). Rising use of diagnostic medical imaging in a large integrated health system. *Health affairs*, 27(6):1491–1502. 17

Spahn, M. (2013). X-ray detectors in medical imaging. *Nuclear Instruments and Methods in Physics Research Section A: Accelerators, Spectrometers, Detectors and Associated Equipment*, 731:57–63. 8, 17

Taguchi, K., Zhang, M., Frey, E. C., Wang, X., Iwanczyk, J. S., Nygard, E., Hartsough, N. E., Tsui, B. M., and Barber, W. C. (2011). Modeling the performance of a photon counting x-ray detector for ct: Energy response and pulse pileup effects. *Medical physics*, 38(2):1089–1102. 21, 26

Tang, N. D., De Ruiter, N., Mohr, J., Butler, A. P., Butler, P. H., and Aamir, R. (2012). Using algebraic reconstruction in computed tomography. In *Proceedings of the 27th Conference on Image and Vision Computing New Zealand*, pages 216–221. ACM. 85

Tran, C., De Jonge, M., Barnea, Z., and Chantler, C. (2004). Absolute determi-

nation of the effect of scattering and fluorescence on x-ray attenuation measurements. *Journal of Physics B: Atomic, Molecular and Optical Physics*, 37(15):3163. 58, 78

Uher, J., Harvey, G., and Jakubek, J. (2012). X-ray fluorescence imaging with the medipix2 single-photon counting detector. *IEEE Transactions on Nuclear Science*, 59(1):54–61. 57

Vanden Broeke, L. (2015). Foil fluorescence in mars spectral imaging. Master's thesis, University of Canterbury. 15, 37, 41, 42, 50, 52, 56, 63

Walsh, M., Nik, S., Procz, S., Pichotka, M., Bell, S., Bateman, C. J., Doesburg, R., De Ruiter, N., Chernoglazov, A., Panta, R., et al. (2013). Spectral ct data acquisition with medipix3. 1. *Journal of Instrumentation*, 8(10):P10012. 23

Watt, J., Davidson, D., Johnston, C., Smith, C., Tlustos, L., Mikulec, B., Smith, K., and Rahman, M. (2003). Dose reductions in dental x-ray imaging using medipix. *Nuclear Instruments and Methods in Physics Research Section A: Accelerators, Spectrometers, Detectors and Associated Equipment*, 513(1-2):65–69. 9

Zeller, H., Dufreneix, S., Clark, M., Butler, P., Butler, A., Cook, N., and Tlustos, L. (2009). Charge sharing between pixels in the spectral medipix2 x-ray detector. In *Image and Vision Computing New Zealand, 2009. IVCNZ'09. 24th International Conference*, pages 363–366. IEEE. 22, 26